UNIVERSIDAD CARLOS III DE MADRID

DEPARTAMENTO DE CIENCIA E INGENIERÍA DE MATERIALES E INGENIERÍA QUÍMICA

Tesis doctoral

Microwave medical imaging using level set techniques

Autor: Natalia Irishina

Directores: Oliver Dorn y Miguel Moscoso

Programa de doctorado en Ingeniería Matemática

Enero de 2009

MICROWAVE MEDICAL IMAGING USING LEVEL SET TECHNIQUES

Memoria que se presenta para optar al título de
Doctor por la Universidad Carlos III de Madrid
por el programa en Ingeniería Matemática

Autor: Natalia Irishina
Director: Oliver Dorn y Miguel Ángel Moscoso Castro

Programa de doctorado en Ingeniería Matemática
Departamento de Ciencia e Ingeniería de los Materiales e Ingeniería Química
Escuela Politecnica Superior
Universidad Carlos III de Madrid
Enero de 2009

Tesis doctoral

Microwave medical imaging using level set techniques

Autor: Natalia Irishina

Directores: Oliver Dorn
Miguel Ángel Moscoso Castro

Firma del Tribunal Clasificador:

Firma

Presidente		
Vocal:		
Vocal:		
Vocal:		
Secretario:		

Calificación:

Leganés, Enero de 2009

A mi familia

Agradecimientos

El primer y el más profundo agradecimiento es para mis directores de tesis Oliver Dorn y Miguel Ángel Moscoso Castro, por su confianza al incluir a mí en su proyecto de investigación, su dedicación y sus sugerencias durante la realización de esta tesis. Tengo que agradecer también al Grupo de Modelación y Simulación Numérica y Departamento de Ciencia y Ingeniería de los Materiales e Ingeniería Química por los medios materiales y humanos de los que he disfrutado durante el tiempo de elaboración de la tesis.

Resumen

El cancer de mama es una de las enfermedades que causan una mayor mortalidad entre las mujeres. Se estima que, slo en Europa, una mujer es diagnosticada de esta enfermedad cada 2 minutos y medio, y que una muere cada 7 minutos y medio. Para su cura es fundamental la deteccin temprana de los pequeños tumores. Si éstos son detectados a tiempo, los tratamientos que existen hoy en da son mucho más efectivos. En consecuencia, es de fundamental disponer de tecnologías especializadas que puedan llevar a cabo esta tarea con seguridad y, al ser posible, a un costo bajo.

La técnica de referencia hoy en día sigue siendo la mamografa, una imagen de rayos X de la mama comprimida. Sin embargo, éstas siguen teniendo inconvenientes bien conocidos: no detectan un 15 % de los tumores malignos, al mismo tiempo que el resultado de los falsos positivos es muy elevado (sòlo un 13 % de las manchas encontradas resultan finalmente ser un tumor maligno). Adems, exponen a las pacientes a radiación potencialmente peligrosa y el procedimiento es, a veces, poco confortable. Otras técnicas, como la resonancia magnética, dan buenos resultados pero son muy caros y no pueden utilizarse como medio de prevención a una escala general. Por ello, otras técnicas alternativas se están estudiando en la actualidad para el diagnóstico no invasivo de esta enfermedad. Entre ellas, destacan la tomografía de óptica difusa, la tomografía de impedancia eléctrica y las imágenes de microondas.

En esta tesis se propone un algoritmo numérico especialmente diseñado para la detección y caracterización de pequeos tumores usando microondas. La idea consiste en iluminar la mama con radiación de frecuencias del orden de unos pocos GHz, y reconstruir las imágenes del interior a partir de las señales que se recogen en la superficie de la mama. La reconstrucción de estas imagenes supone la resolución de un problema inverso en donde se minimiza la diferencia de las señales medidas y las simuladas con el modelo de mama propuesto (que incluye el posible tumor). Para ello aplicamos técnicas novedosas de conjunto de nivel que permiten la representación implícita de las estructuras del interior de la mama, y suponen además una regularización implicita que estabiliza la resolución del problema inverso.

Los resultados de nuestros experimentos numéricos demuestran que el algoritmo es capaz de localizar los tumores y reconstruir las distrubuciones de

los parámetros dieléctricos dentro del mama de una manera eficiente. El algoritmo no sólo detecta el posible tumor y aproxima correctamente su tamao, sino que además es capáz de caracterizar el tejido sano por su contenido en fibra y grasa y aproximar las propiedades dieléctricas del tumor, que pueden ser reflejo de su grado de malignidad.

Contents

Chapter 1

Introduction

1.1 Motivation

Breast cancer is one of the most dangerous diseases in the modern world with a high mortality [32]. It is estimated that within the European Union, every 2.5 minutes a woman is diagnosed with breast cancer. Every 7.5 minutes a woman dies from the disease [64]. The early detection of small breast tumors is absolutely necessary for preventing the metastasis of the cancer and for obtaining good prognosis of cancer treatment. Therefore it is of highest importance to have technologies and algorithms available which are able to image tumorous structures of few milliliters in the breast non-invasively and with relatively low cost.

The gold standard technique for early tumor detection is still the x-ray image of the compressed breast, the *mammography*, which remains the primary screening method for detecting non-palpable early-stage breast cancer tumors. The mammogram essentially is a map of breast density (see Fig.1.1). The resolution of the obtained image is high, however, the contrast is low. It is difficult, even impossible in many cases, to localize a tumorous structure of few milliliters or to distinguish between the different types of benign and malignant tumors. Overall, mammography misses up to 15% of the cancerous tumors [37]. At the same time, the false positive results of the mammography technique, which amounts to an estimated 13% of all suspicious findings, lead to the need for additional mammographies and biopsy tests [37]. An additional drawback of X-ray breast screening is the potential danger of the X-ray itself, which is an ionizing radiation. Furthermore, the mammography procedure is uncomfortable and even painful for many patients. All these drawbacks and inconveniences produce anxiety in many patients, accumu-

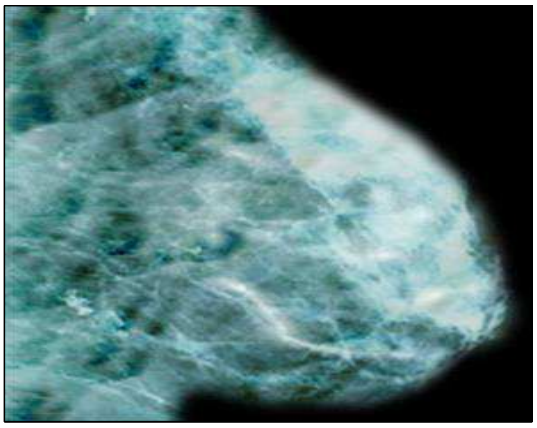

Figure 1.1: A typical X-ray mammography image which a trained physician can use for detecting suspicious spots for possible hidden tumors.

late the radiation exposure of healthy tissue and increase the overall costs of tumor detection [32].

The natural question arises if any alternative radiation technique, less dangerous and possibly even more effective than mammography, can be developed and used clinically to enhance the diagnosis. Over the last decade, the use of microwaves for breast screening has developed into such a new and very promising diagnostic option [37].

But what are the advantages of microwaves for breast screening? The dielectric properties of different biological tissues, including normal and tumorous breast tissue, have been investigated scientifically during the past four decades [18, 23, 40, 41]. The obtained data indicate that there exists a significant contrast between the dielectric properties of tumorous and normal breast tissue [75]. This characteristic difference in the dielectric parameters (permittivity and conductivity) appears, among other reasons, due to increased water content, protein hydration and vascularization of the tumorous tissue.

Microwaves are called here the electromagnetic waves with frequencies ranging from 300 MHz up to 30 GHz. The breast can easily be radiated from outside and is translucent to microwaves in this regime, up to a certain degree. Microwave radiation, as used in the screening process, contains insufficient energy to directly change biological tissue by ionization or similar effects, and

consequently, is a very harmless radiation. Most of the studies conclude that it is perfectly safe for the human health [36, 37]. On the other hand, since microwaves potentially give rise to a certain amount of heating of organic tissues, many investigators point out its potential, when applied with much higher power than in the screening process, to be used in tumor treatment for destroying cancerous tissue by locally overheating suspicious marks [51].

In response to the increasing interest in microwaves for breast cancer detection, new studies have been prepared and published recently containing and analyzing the breast data of a large group of patients [71, 72, 73]. The result of this work is that the contrast between the healthy and tumorous tissue is lower than it was reported in earlier studies. In particular, the contrast in dielectric properties is less significant for breasts with higher content of dense fibroglandular tissue. Nevertheless, a majority of breasts can be classified as mostly 'fatty' (fatty tissue is from 3 up to 10 times less dense than fibroglandular tissue), with approximately 70% of fatty and 30% of fibroglandular tissue [86]. This important circumstance supports the hope that, in a majority of the cases, the possibility of the successful detection of very small tumors via microwave imaging exists. Furthermore, for the case of very dense breasts and consequently lower contrast, new imaging strategies and new numerical algorithms need to be developed which exploit in an optimal way the sensitivity of microwaves to the existence of such a small dielectric contrast. In this thesis, we present a new numerical algorithm which efficiently detects, locates and characterizes small breast tumors in different types of breasts. In particular, we will see that for the cases in which the breast is very dense and/or the tumor is small and it is located deep in the breast, it is necessary to reconstruct, in addition to the tumor, the internal breast structure.

Lately, significant improvements of the existing microwave imaging techniques have been obtained due to the progress in the underlying numerical methods and engineering devices. Many research groups are investigating the application of microwaves for breast cancer diagnosis, among them prestigious research groups at the University of Wisconsin, at Dartmouth College, at the Northeastern University of Boston, and others.

Finalizing this introduction, we want to resume the expected advantages of microwaves for the early breast cancer detection:

- Microwaves are absorbed and reflected differently by tumorous and healthy tissues.

- They detect breast cancer at a curable stage.

- They have low health risk.
- They penetrate easily through tissue because the biological tissue is translucent to microwaves.
- They involve minimal discomfort and the examination is easy to perform.
- The cost of microwave screening is predicted to be very low.

In this thesis we investigate the potentials, advantages and disadvantages of microwave imaging for the early detection of breast cancer from a more mathematical and computational viewpoint as opposed to the experimental studies which already exist in the literature. We present a new numerical algorithm for the detection of small breast tumors via microwave imaging, and demonstrate its robustness and advantages when used for early breast cancer detection. We show that the new algorithm can be successfully applied not only for tumor detection, but also for the characterization of the internal breast structure and the dielectric characterization of tumorous inclusions. From the mathematical viewpoint, we propose a novel scheme of using two or more different level set functions simultaneously for achieving structural inversions from few data. In particular, we not only reconstruct various different interfaces in the breast tissue, but also interior profiles characterizing fatty and fibroglandular tissue textures from the same data set. This is a very novel development in the framework of level set inversion schemes.

The following sections of this chapter 1 are organized as follows. In section 1.2 we describe the anatomical structure of the human breast from the perspective of microwave imaging applications. The next section 1.3 reviews the currently existing imaging techniques for breast screening and the main research directions in the microwave medical imaging literature. In section 1.4 we define the underlying inverse problem and general concepts of ill-posedness. Finally, the last section 1.5 is devoted to the introduction into the level set technique as used in this thesis.

1.2 Breast anatomy

Human breast consists mainly of glandular, fatty and fibrous tissue located on the pectoral muscles of the chest wall and attached to the skin by fibrous strands called Cooper's ligaments, as it is visualized in the left image of Fig. 1.2.

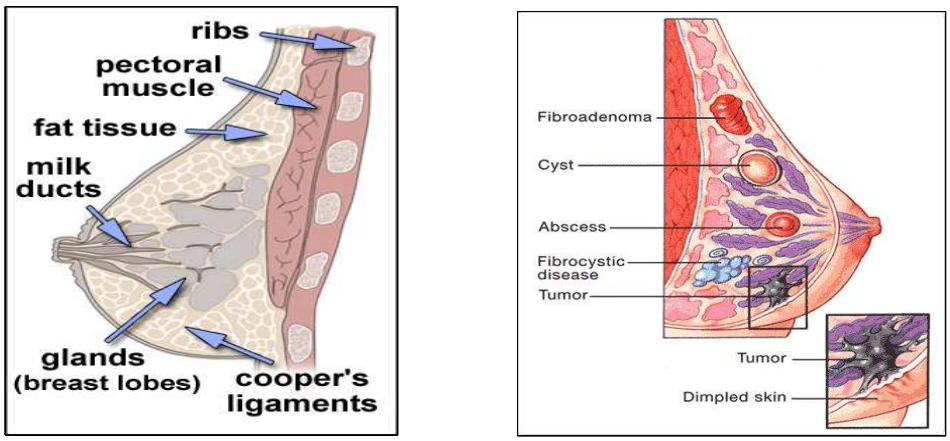

Figure 1.2: Breast internal structure (left image) and the anomalies of healthy tissue (right).

The density of the breast depends on its relative content of fibroglandular and fatty tissue and vary from patient to patient. It is difficult to predict the physiological structure of patient's breast, because there are many factors which can influence it. At the same time, this knowledge sometimes determines the success of the diagnoses, because in particular for the denser breasts of high content of fibroglandular tissue the techniques used for the reconstruction need to be more refined, as it is necessary to reconstruct the denser parts of the breast together with the correct tumor characteristics.

A tumor, which can be precancerous (benign) or cancerous (malignant), may apparently have no symptoms and is difficult to detect at the early stage by traditional methods (X-ray mammography), especially if it is situated deeply inside the breast. However, the success of the treatment depends heavily on the size of the detected tumor, i.e. on the current stage of the disease.

The recently published studies [71, 72, 73] have demonstrated that the contrast between the dielectric properties of healthy and tumorous tissues, as well as the dielectric contrast between the benign and malignant tumors, are not so large as expected. Malignous anomalies have a high content of water, as they are typically crossed by more blood vessels than benign anomalies. Therefore, we can in general assume a higher grade of malignancy for lesions with higher dielectric parameters.

The difficulty of early cancer diagnosis is that inside the breast tissue there

exist a large variety of possible physiological anomalies. They are related to age, hormonal treatments, lactate periods or lesions. In the right image of Fig. 1.2 we can see benign lesions, as for example a cyst, a fibroadenoma or an abscess, as well as a malignant lesion, which is a tumor. All these lesions give rise to local changes in the dielectric properties of the healthy tissue. In the X-ray image all these abnormalities result in a very similar response, namely spots of higher density. This similarity is the main reason for the large number of false positives in cancer detection.

Our algorithm aims at early cancer detection in cases of breasts of different densities. It can be applied also to the reconstruction of the structure of healthy breast tissue and the detection of any benign lesion, if necessary.

1.3 Imaging techniques for breast screening

Methods of noninvasive breast imaging can be divided into two groups: the classical techniques and those which have been developed more recently.

Among the classical techniques for breast imaging we mention the mammography, magnetic resonance imaging, positron emission tomography and ultrasound imaging.

Mammography is the process of using low-dose X-rays to examine the human breast for the early detection of breast cancer. This is typically done by detection of characteristic spots of dense tissue, which need to be distinguished from microcalcifications. As it was mentioned before, X-ray mammography is still the main tool in the breast cancer screening, but suffers from certain drawbacks and is not very effective in many cases (see the subsection 1.1).

Magnetic resonance imaging (MRI) is a medical imaging technique which provides much greater contrast between the different soft tissue types of the body than other methods. It uses a strong magnetic field to align the nuclear magnetization of hydrogen atoms in water molecules of the body. Radiofrequency fields are used to alter the alignment of this magnetization, which produces a rotating magnetic field of hydrogen nuclei which can be detected by a scanner. The MRI method can create images of high resolution, is very precise in its diagnosis, but unfortunately it is very expensive to use as a broad-scale preventive screening tool.

Positron emission tomography (PET) is a nuclear medicine imaging technique which produces a three-dimensional image or map of different parts of the body. A positron-emitting radionuclide is introduced into the body, and the system detects pairs of gamma rays emitted by this tracer. The computer

analysis reconstructs the images of tracer concentration in the 3-dimensional space. In general, the quality of the image delivered by this reconstruction technique is not as good as the one of MRI reconstructions.

Diagnostic ultrasonography is an ultrasound-based diagnostic imaging technique used to create images of the internal body organs, their sizes, structures and possible pathologies or lesions. In physics, ultrasound refers to acoustic waves of frequencies above the limit which the human ear can hear (higher than 20 kHz). The scanner usually operates in the frequency range between 2 and 18 MHz. The resolution of the image depends on the chosen frequency: lower frequencies produce images of less resolution than higher frequencies do. The acoustic wave propagating through the tissue is reflected when it hits an interface of regions with different densities, and the reflected wave can be measured by a transducer. The depth of the tissue interface is calculated from the travel time of the reflected sound wave. The attenuation of the sound wave is increased at higher frequencies. Therefore, in order to have better penetration of deeper tissues, a lower frequency (3-5 MHz) is often used despite of the lower resolution which can be achieved with lower frequencies.

The limitations of X-ray mammography, which is the gold standard in early detection of breast cancer, provide a clear motivation for the development of new complementary breast imaging strategies to assist in the detection and diagnosis of small tumors. Among the newer imaging techniques under investigation for breast screening we want to mention in particular *diffuse optical tomography* (DOT), *electrical impedance tomography* (EIT) and *microwave imaging* (MI).

Diffuse optical tomography is a particular case of computed tomography where the photons of the near-infrared regime show significant scattering during their way through the body. Near-infrared light penetrates within the tissue several centimeters but suffers from a large amount of scattering which blurs the images of the optical inhomogeneities of the tissue. Consequently, new tomographic algorithms have been devised to overcome this problem and improve the resolution of these images [28, 2, 63, 61]. Diffuse optical tomographic technologies use either continuous-time, or time-harmonic, or time-pulsed excitation. The time-pulsed excitation is realized by means of the exposure of the tissue to short laser pulses of the order of nanoseconds, or even shorter. The data gathered at the detectors are superpositions of large numbers of photons with different path histories inside the tissue but the same travel time and/or receiver location when measured. They are sensitive, for example, to the local oxygenation status of the blood, which can be used for tumor detection or for detecting a hematoma. In the time-harmonic

mode, the tissue is illuminated with modulated light in the frequency range 0.1-10 GHz (this is the so called frequency-domain or phase method). Then, the degree of modulation of the scattered light and the corresponding phase shift at modulation frequencies is recorded as data.

Electrical impedance tomography is a medical imaging modality in which an image of the conductivity or permittivity of a part of the body is constructed from surface electrical measurements. The electrodes are attached to the surface of the body transmitting small alternating currents. The resulting electrical potentials are measured, and the process is repeated for numerous different configurations of applied currents [54, 9, 62].

Microwave imaging, on the other hand, can be divided further into two groups: the radar techniques (among them confocal microwave imaging and space-time beamforming) and tomographic imaging techniques. Both of these groups are under intensive development. Confocal imaging and space-time beamforming are non-iterative techniques which display the received backscattered signal energy as a function of location to define the regions of the breast of increased scattering power [46, 47, 35, 75, **?**, 8, 74]. Beamforming methods are developed to overcome the difficulties associated with the high heterogeneity of the breast tissue. Their spatial resolution is proportional to the bandwidth of the applied signal.

Other broadband array imaging techniques that provide an image of the backscattered signal in clutter are currently under investigation [10]–[14]. Borcea *et al.* [13] have proposed a new method, called *coherent interferometry*, for imaging in randomly inhomogeneous media. The authors introduce an imaging functional that does not depend on the detailed properties of the random media, and apply the optimal smoothing of the image to stabilize it. To compensate for the delay spread of the signal due to multipathing in these media, they cross-correlate the traces over appropriate space-time windows. In addition, optimal illumination and waveform design for array imaging can be used to enhance the resolution of small scatterers [14].

All these methods, as well as the tomographic techniques, are based on the supposed high contrast between the dielectric properties (permittivity and conductivity) of the tumors, benign or malignant cysts, and the healthy breast tissues, namely the fibrous, glandular, adipose and skin tissue [23, 40, 37]. We point out that, so far, these methods are not able to reconstruct the shape of the scattering region. They can only identify it.

To differentiate a malignant tumor from benign tumor, El-Shenawee and Miller have proposed a *shape-based method* aims at accurately estimating certain shapes and their locations of anomalous regions [34]. Malignant tumors tend to have irregular shapes due to the invasive nature of malignant

cells and their random growth [1]. Benign tumors, however, tend to have smoother more ellipsoidal or spherical shapes. Typically, the quality of a shape reconstruction algorithm also depends on the accuracy with which the electromagnetic properties (permittivity and conductivity) of the tumors are known or, if they are unknown a-priori, can be estimated simultaneously with the shapes. There are several differences between the work of [34] and the shape-based work presented here, which will be pointed out further below in this thesis.

Finally, *microwave tomographic imaging* (which most closely characterizes the technique used in this thesis) is showing a significant promise as a new technique for the early detection of breast cancer. It includes the measurements of the scattered microwave signals through the contrast media and simulate these signals numerically using a breast model. The corresponding inverse problem consists in minimizing the mismatch between the signal of the scattered waves and the one simulated with the numerical model, undertaking at the same time the corresponding corrections of the initial model [79, 17].

One-step inversion methods, like the *Born and Rytov approximations*, are applied in practice as well, but they are only able to give an indication about the location of an inhomogeneity in the tissue [52, 15]. The classical pixel-based iterative algorithms, which go beyond the Born and Rytov approximations, successively improve the initial guess. This is done by comparing the predicted data corresponding to the latest estimate of the tumor characteristics with the measured data, and minimizing the resulting least-squares data misfit. In order to stabilize the inversion process, the least-squares data misfit is typically augmented by some additional regularization terms. Unfortunately, the standard Tikhonov-Philips regularization term, usually employed in these strategies, has the effect of 'over-smoothing' the reconstructed images. As a consequence, it is difficult or impossible to accurately estimate key characteristics of the breast internal structure and the tumor, like their shapes and internal dielectric properties.

Obtaining these characteristics, on the other hand, could lead to potentially important strategies for breast cancer diagnosis and the definition of the interior density of breast tissues. In part of the clinical situations studied recently, the fibroglandular tissue has high density and assumes dielectric properties which become closer to those typically assumed for tumors. This means that, in contrary to previous believe, the contrast between tumor and healthy tissue is not necessarily always very high, even though it still seems to be significant [81, 71, 72, 73]. *This lower contrast increases even further the need for very efficient and robust mathematical reconstruction techniques*

for extracting reliable estimates of tumor characteristics from the microwave data. This thesis aims at going one significant step forward in this direction by providing a new reconstruction algorithm which makes optimal use of the microwave data and of some of the available prior information about typical human breast tissue.

1.4 Some general concepts

In his original paper [58], J. B. Keller calls two problems 'inverse to each other' if the formulation of one involves the formulation of the other. For example, the problem which predicts the future behavior of a physical system from knowledge of its current state would traditionally be called the direct problem, whereas the problem of determining the present state from future observations (for example, certain observations of the system's evolution) would be called the inverse problem. The inverse problem is usually *ill-posed*. The definition of ill-posedness of a problem will be introduced in the subsection 1.4.1. In order to solve ill-posed problems in a stable and reliable way, typically *regularization* methods are needed. Some typical regularization techniques are outlined in subsection 1.4.2.

1.4.1 Ill-posedness of the inverse problems

In this section we will give a brief outline of important concepts of ill-posedness using, as example, a linear operator equation $Am = b$ with a bounded linear operator $A : H \to K$ which maps from a Hilbert space H to a Hilbert space K. We can define the corresponding direct problem as finding b assuming m is known, whereas the corresponding inverse problem is to find m from the knowledge of b, which satisfies $Am = b$ in some meaningful sense [84]. The problem of calculating m is directly related with the properties of the operators A and, if it exists, of A^{-1}.

We say that the inverse problem is well-posed or properly posed if the three following conditions are satisfied:

- The exact solution exists.
- There is no more than one solution.
- The solution depends continuously on the data.

These three conditions mean that b is in the range of A, that A is injective and A^{-1} exists and is continuous in the given spaces. Usually, the typical

inverse problems encountered in medical imaging do not satisfy the above three requirements (often none of them at all), which means that they are ill-posed. Moreover, when one discretizes the ill-posed inverse problem to solve it numerically, the discretized problem is typically represented by an ill-conditioned matrix. For this discretized problem, the condition number [1] becomes bigger the finer one chooses to discretize.

1.4.2 Regularization

From the above discussion it follows that for solving an ill-posed inverse problem, we need to regularize it. Regularization means to replace the ill-posed inverse problem by a family of nearby well-posed problems, which often is characterized by one or more regularization parameters. In the end, one member of this family of approximated well-posed problems is chosen to represent the solution of our ill-posed inverse problem. This replacement of the (often non-existing) solution of the ill-posed problem is often called a 'quasi solution'.

The least squares method is often used to regularize an inverse problem. The goal is to find an estimate m^+ such that it minimizes the least-squares data misfit functional

$$\mathcal{J} = \|Am - b\|^2 . \tag{1.1}$$

If there is more than one minimizer, we choose the one with minimal norm and call it m^+. It can be shown that m^+ is the unique solution of the corresponding normal equations $A^*Am = A^*b$, where A^* is the formal adjoint operator to A [33]. By this choice of m^+ we define an operator A^+, such that: $A^+b = m^+$. If we know the singular value decomposition of operator A, the generalized solution m^+ of the inverse problem is determined by the Moore-Penrose generalized inverse A^+ as follows [33]:

$$m^+ = A^+b = \sum_{i=1}^{r} \lambda_i^{-1} < b, w_i > v_i \tag{1.2}$$

where $\{\lambda_i, v_i, w_i\}$ are the singular values and vectors of A, respectively. r is the number of singular values λ_i distinct from zero.

The singular values of an ill-posed inverse problems are often characterized by a rapid decay, which has the effect that noise in the data introduces an instability to the generalized solution due to small singular values. Most

[1] The condition number $c_a = \|A\|\|A^{-1}\|$ is a useful measure of the stability, which characterizes the dependence of the error in the predicted solution from the error in data.

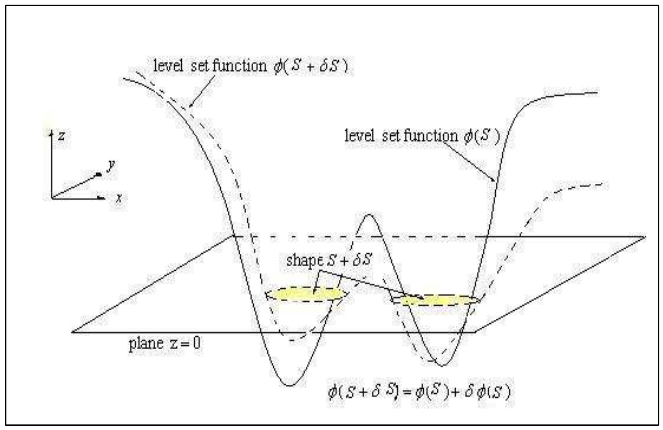

Figure 1.3: The level set function ϕ implicitly defines the shape S. A small perturbation $\delta\phi$ changes the shape S to the new shape $S + \delta S$ in an implicit way.

regularization methods aim at damping or eliminating those parts of the solution which correspond to very small singular values. If an iterative algorithm is used for solving an ill-posed inverse problem, then the early stopping of the iterative method can be interpreted as a form of regularization. This is so, since often the earlier iterations concentrate more on the parts of the solution which correspond to larger singular values, whereas the later iterations tend to fit the parts corresponding to smaller singular values.

Another popular regularization method is the so called Tikhonov method [101]. The goal is to find the m_α which minimizes the modified cost functional

$$\mathcal{J}_\alpha = \|Am_\alpha - b\|^2 + \alpha\|m\|^2 \ , \tag{1.3}$$

with the regularization parameter $\alpha > 0$, which controls the weight of the penalty term $\|m\|^2$ (and some appropriate norms $\|\ |, ||$ chosen). The modified normal equations in the least squares sense are

$$(A^*A + \alpha I)m_\alpha = A^*b \ , \tag{1.4}$$

which solution formally is $m_\alpha = (A^*A + \alpha I)^{-1}A^*b$.

If we know the singular value decomposition of A, this solution can be formally written as a 'filtered' version of the generalized inverse, in the following sense

$$m_\alpha^+ = A_\alpha^+ b = \sum_{i=1}^{r} \frac{\lambda_i^2}{\lambda_i^2 + \alpha} \lambda_i^{-1} < b, w_i > v_i. \tag{1.5}$$

Therefore, the Tikhonov regularization method can be interpreted as a 'filtering' method. It filters out those components of the singular value decomposition with $\lambda_i^2 \ll \alpha$.

The above mentioned regularization schemes are aiming mainly at suppressing the impact of data noise on the reconstruction. In general, a difficulty of ill-posed problems is the often high dimension of the solution space and the small number of data which are available to determine a valid solution. One way of regularization is, therefore, the incorporation of a priori information into the solution scheme. This potentially reduces the number of possible solutions and helps focusing in the reconstruction on those features which in fact can be recovered in a stable and reliable way.

Our approach in this thesis follows this general idea of regularization. In our application, we can include this prior information by assuming some knowledge regarding the type of tissues which the breast is composed of. This means that the dielectric properties of the breast tissue are not arbitrary but follow certain rules or constraints which are in agreement with this prior knowledge. In particular, we will make use of the assumption of well defined interfaces between the different tissue types.

Once we have chosen this 'shape-based' approach for the different components of breast tissue, it still remains to reconstruct the shapes from the the boundary data. One possibility is to parameterize the unknown shapes, for example, using harmonic functions, and to cast the problem as an optimization problem by solving for the unknown coefficients of the parametrization as in [34]. However, this approach is limited to shapes which can be represented by the a priori assumed parametrization. Besides, they do not perform well under topological changes of the unknown shapes when these occur during the iterative reconstruction process. In this thesis, we will follow a completely different approach to reconstruct the unknown shapes. They will be implicitly represented by higher dimensional level set functions as will be explained in the next section.

Notice that in the tumor detection task, the problem to be solved is not so much the determination of a detailed and complete map of electromagnetic parameters inside the breast, which would in fact be impossible from the given few noisy data. Instead, the physician which interprets the results

would be satisfied if just a few questions could be answered reliably from the data, namely regarding the existence, size, contrast and possibly shape of one or more hidden tumors. Certainly, this information cannot be recovered reliably without specifying from the same data set at least some overall features of the remaining structure of the breast tissue. Not all of these remaining features might have the same impact on answering the important questions stated above. Also, certain characteristics of the breast are in fact known (say, for example, the existence of interfaces between glandular and fatty tissue, and a range of possible values for these two tissue types), such that this prior knowledge might help in focusing on the main goal of the interpretation of the data.

The novel level set technique proposed in this thesis is following this path of focusing on the reliable answering of the above mentioned important questions of the existence and main characteristics of hidden breast tumors. It aims at providing an optimal way of using all available information at hand in the inversion of microwave data of the breast.

1.5 Level sets

The level set method was originally developed by Osher and Sethian for describing the motion of curves and surfaces [88, 89]. Since then, this method has been widely applied in different areas of research. Examples are the application to image enhancement, modelling physical interface problems, crystal growth, and others [93]. In 1996, Santosa proposed to use the level set technique for solving inverse problems with interfaces [92]. In this seminal paper he presented as examples the solution of linear inverse problems using the level set technique for shape representation. Later, the level set method was used by Litman *et al* for a nonlinear inverse scattering problem [76]. In that work, a shape evolution is defined by calculating the derivative of the cost functional with respect to the hidden shape, the boundary of the shape moving in a descent direction of the corresponding cost functional. The calculation of the interface velocity, i.e. the updates for the level set function in each step, requires the solution of one forward and one adjoint Helmholtz problem. In that work, the evolution of the level set function is controlled by a Hamilton-Jacobi-type equation describing shape evolution. In this thesis, we will follow a slightly different approach in which the level set function is updated by means of an evolution law directly formulated for the level set function. Next we explain the main ideas of the representation of shapes by level sets and introduce the evolution law as our main tool for

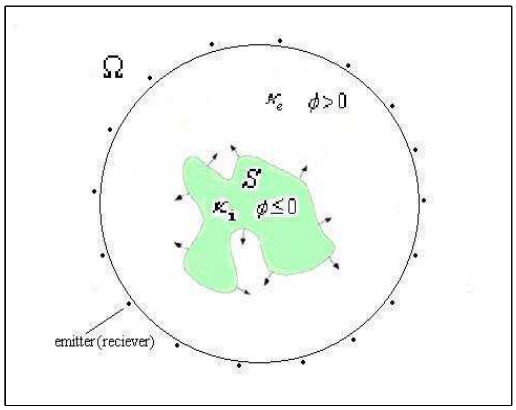

Figure 1.4: The distribution of the characteristic parameter $\kappa(\mathbf{x})$ is defined by a level set function ϕ. In optimization approaches, an evolution of the shape S is performed in order to decrease the mismatch between measured and predicted data.

the shape reconstruction.

1.5.1 Representation of two regions by level sets

In the level-set method the shape of an object is represented implicitly by one higher-dimensional level set function. The boundary of the shape coincides with the zero level set, and the negative values of the level set function define the interior of the shape. Figure 1.3 illustrates this relationship. The figure shows a possible level set function ϕ at some step of a shape evolution (solid line), and a possible modification of this level set function (dashed line) after an update $\delta\phi$ has been applied according to some criterion (e.g. reducing a predefined cost function). Obviously, the implicit representation of a level set function is not unique since there are infinite many level set functions which can define one given shape S.

Usually, the number of components in the domain of interest S is arbitrary (finite) and unknown. During the reconstruction process, typically the need for modelling topological changes arises. Traditional parameterized models for the shape S are not suited for modelling such topological changes since they require reparameterization in that case. The advantage of using the level set technique is that topological changes occur automatically without

the need for reparameterization [31].

In the simplest form of the level set representation, only two regions are considered: an anomaly region and the embedding background medium, both typically with a constant parameter value. The anomaly region (in the following sometimes called 'object') can consists of a finite collection of disjoint compact subdomains enclosing 'holes' filled with the background material, but all the subdomains have the same material (or biotissue) properties. In this case, only one level set function is necessary to define the resulting bimodal distribution that needs to be reconstructed. A level set function $\phi(\mathbf{x})$ defines the piecewise constant coefficient $\kappa(\mathbf{x})$ that characterizes the domain Ω, with $\mathbf{x}$ being the location variable, in the following way

$$\kappa(\mathbf{x},\phi) = \begin{cases} \kappa_i & \text{in} \quad \mathrm{S}, \quad \phi(\mathbf{x}) \leq 0 \\ \kappa_e & \text{in} \quad \Omega\backslash\mathrm{S}, \quad \phi(\mathbf{x}) > 0\,. \end{cases} \tag{1.6}$$

In this way, the distribution of this characteristic parameter in the domain Ω depends on the level set function $\phi(\mathbf{x})$ (see Fig. 1.4). For the computational evolution of the level set functions it is useful to introduce the narrowband $\chi(\mathbf{x})$, which coincides with a neighborhood of $\phi(\mathbf{x})$ with a specific width. Often, the level set function is modified only inside this narrowband for moving the boundary computationally one step. In this thesis, we will present and discuss more general approaches for level set evolution which are tailored to the application of structural inversion in medical imaging from microwaves.

A possible optimization approach for calculating the evolution of the level set function $\phi(\mathbf{x})$ consists in minimizing the least squares cost functional defined as

$$\mathcal{J}(S) = \frac{1}{2}\|Am - b\|^2. \tag{1.7}$$

To formally evolve the level set function $\phi(\mathbf{x})$, a velocity field $v(\mathbf{x})$ is introduced for each point of the domain (see for more details the exposition in [31]). The goal is to decrease the cost functional $\mathcal{J}(S)$ by applying a suitable velocity field $v(\mathbf{x})$ in direction $n(\mathbf{x})$, normal to the boundary of the shape. Usually, the evolution is performed only in the narrowband $\chi(\mathbf{x})$ of the shape boundary. Obviously, the tangential component of $v(\mathbf{x})$ does not contribute to the shape deformation. Mathematically, the general expression for the descent direction of the cost functional contains the scalar product $v(\mathbf{x})n(\mathbf{x})$, where $v(\mathbf{x})$ is calculated appropriately. In this thesis, we will follow a slightly different approach (even though related) by defining an evolution law

$$\frac{d\phi}{dt} = f(\mathbf{x},t)\,, \tag{1.8}$$

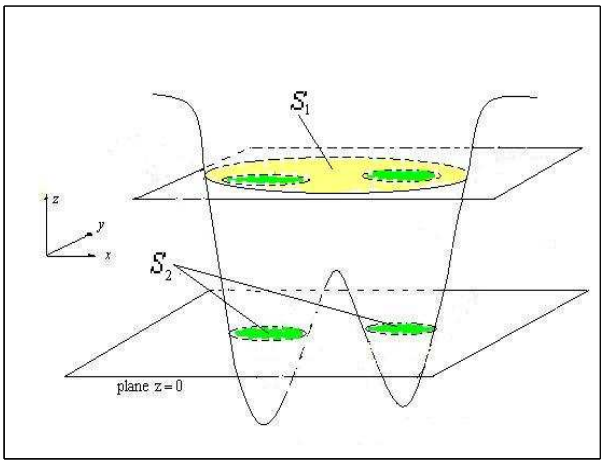

Figure 1.5: A unique level set function representing two materials.

for the level set function ϕ describing the interface between different tissue types (in this case, the tumorous and the healthy tissue). The scalar forcing term $f(\mathbf{x}, t)$, which depends on the position $\mathbf{x}$ and the artificial evolution time t, is determined such that the cost functional (1.7) decreases. In chapter 3 we derive an explicit mathematical expression for $f(\mathbf{x}, t)$ and demonstrate how it is used numerically as part of the reconstruction problem.

1.5.2 Level set representations for multiple regions

In many applications one needs to reconstruct the parameter distribution of interest defined by more than two possible values as, for example, in our case the different dielectric parameters corresponding to the several tissue types inside the breast. The level set approaches in the literature that deal with this problem can be divided into two groups: the techniques which use only one level set function, and the techniques which use two or more level set functions depending on the number of different materials (here bio-tissues) within the domain.

In the first approach, the interfaces of the different materials are represented by the same smooth level set function, but using level-sets for different levels (values). Figure 1.5 illustrates this idea in which the shapes of two materials correspond to two predefined level values, in addition to the

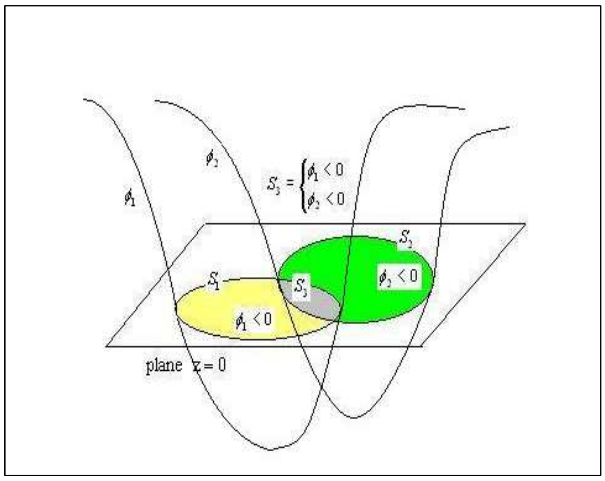

Figure 1.6: A vector level set representation for two materials.

background value. However, this approach has some drawbacks (as it is discussed in [77]) since it might not exist any smooth level function satisfying the necessary requirements (certain topological restrictions apply with this approach).

In the second approach, several level set functions are used to represent a domain composed of multiple regions (each level set function associated with a different material), as in [107, 95]. Note, that the level sets can overlap during the iterative process (see the Fig. 1.6) giving rise to physically not well-defined materials with multiple values. In this case, additional constraints can be introduced in the cost function in order to minimize the overlap area. Alternatively, a slightly different approach of using more than one level set function has been proposed in [102, 22, 77], to deal with this problem. Here, each possible sign combination of the different level set functions defines a different region. This avoids overlap regions with undefined values. Our approach used in this thesis is somehow similar to that approach, even though we modify this general idea to the specific situation of tumor detection in breast tissue, and to the specific algorithm proposed here. For more details see chapter 4 of this thesis. More information regarding alternative level set techniques for inverse scattering problems as discussed in the literature can be found in the recent review [31].

Chapter 2

Mathematical modeling: the direct problem

2.1 Introduction

This chapter presents the basic ideas of the mathematical modeling used throughout this thesis. We begin with Maxwell's equations and the two-dimensional wave propagation problem used here. We then discuss the numerical method employed when solving the forward (and adjoint) problems during the reconstruction. We also present the different breast models we have considered in our investigations, and the model used here for describing dispersion in human tissue.

Associated with any inverse problem there is a direct problem (sometimes called a forward problem). In the case of the scattering of electromagnetic waves from a hidden object, the direct problem seeks to determine the scattered fields measured at the detector positions given some model of the scattering medium, i.e., it calculates some physical response. On the other hand, the inverse problem consists in determining the properties of the scattering medium, given the source configuration and some measurements of the scattered fields.

In general, as mentioned before, the formulations of the direct problem and the inverse problem of any practical application involve all or part of the solution of the other [58]. Often, the direct problem has been studied extensively and is well understood, while the inverse problem is newer and not so well understood. Also, the direct problem is usually well-posed, whereas the inverse problem is usually ill-posed. This is so, because in most physical techniques used for imaging the direct problem provides a unique and typi-

cally stable response given the relevant physical data (or small variations of them), whereas very similar responses can be the effect of different causes in the inverse problem.

We point out that the inverse problem for microwave breast imaging is nonlinear. Hence, most inversion techniques known today require to solve the direct problem many times. Typically, the solution of the inverse problem is achieved by an iterative process, in which successive improvements of an initial guess of the breast model is attempted by minimizing some data misfit cost functional involving the gathered scattered-field data. When employing an adjoint scheme, for example, as part of a gradient based optimization technique, in each iteration of the inversion algorithm, one (or two) direct problems need to be solved. As a consequence, if the forward solver is not efficient, solving the direct problem many times becomes a major computational bottleneck. We will use finite differences modeling and perfectly matched layers (PML) for solving the partial differential equations that describe the propagating waves in a two dimensional configuration. This will model situations in which the patient is lying facedown with the breast naturally extending through a hole in the examination table.

In summary, in our application, solving the forward problem means to calculate the electromagnetic field at the detectors using a model for electromagnetic wave propagation and a model for the scattering medium, which in our case is a two dimensional model of the breast. If we know the properties of the breast (the distribution of its dielectric parameters) and the source configuration, we can calculate the values of the electromagnetic field at each point of the medium, as well as the data gathered at the detector positions. With this data we will infer the spatial distribution of the dielectric parameters, as will be explained in the next chapters.

As in any other practical situation, noise and uncertainty is inevitable. This will be also considered and conveniently modeled in our approach.

2.2 Maxwell's equations

The well-known Maxwell's equations in differential representation and SI units are [105]:

$$\frac{\partial \mathbf{B}}{\partial t}(r,t) + \nabla \times \mathbf{E}(r,t) = 0 \tag{2.1}$$

$$\frac{\partial \mathbf{D}}{\partial t}(r,t) - \nabla \times \mathbf{H}(r,t) = -\mathbf{J}(r,t) \tag{2.2}$$

$$\nabla \cdot \mathbf{B}(r,t) = 0 \tag{2.3}$$

$$\nabla \cdot \mathbf{D}(r,t) = \rho(r,t) \ . \tag{2.4}$$

In these equations, **E**, **H**, **D** and **B** are the electric field, the magnetic field, the electric field displacement, and the electromagnetic induction, respectively. They are vector quantities that completely characterize the electromagnetic field. In (2.1)-(2.4), ρ is the charge density and **J** is the current density. The variables r and t are the position vector and time, respectively. The vector functions **E**, **H**, **D** and **B** completely characterize the electromagnetic field.

If we assume a harmonic dependence on time, the above Maxwell's equations can be written in the frequency domain as:

$$\nabla \times \mathbf{E}(r) = i\omega \mathbf{B}(r) \tag{2.5}$$
$$\nabla \times \mathbf{H}(r) = -i\omega \mathbf{D}(r) + \mathbf{J}(r) \tag{2.6}$$
$$\nabla \cdot \mathbf{B}(r) = 0 \tag{2.7}$$
$$\nabla \cdot \mathbf{D}(r) = \rho(r), \tag{2.8}$$

where $\omega = 2\pi f$ is angular frequency and i is $\sqrt{-1}$.

The Maxwell's equations are not independent. Taking the divergence of (2.1) gives rise to (2.3), and taking the divergence of (2.2) and using the continuity equation

$$\frac{\partial \rho}{\partial t}(r,t) + \nabla \mathbf{J}(r,t) = 0 \tag{2.9}$$

for the electromagnetic field, we arrive at (2.4).

The same holds in the frequency domain. Only two of the equations (2.5)-(2.8) are independent. Hence, in order to apply the Maxwell's equations for the four unknowns **E**, **H**, **D** and **B**, it is necessary to specify the relations between **D** and **E**, and **H** and **B** through the constitutive relations[1]

$$\mathbf{D} = \epsilon \mathbf{E} \tag{2.10}$$
$$\mathbf{B} = \mu \mathbf{H} \ . \tag{2.11}$$

They correspond physically to specifying how much polarization and magnetization a material acquires in the presence of electromagnetic fields. The response of biological tissue, as other materials, to external fields is not instantaneous. For this reason, the permittivity ϵ is treated as a complex

[1]We consider here the case of isotropic media in which the constitutive relations are independent of the field polarization. Moreover, we assume that the medium is linear, so ϵ and μ are not functions of the fields.

function (complex numbers allow specification of a magnitude and a phase). Moreover, the time response of the biological tissue depends on the frequency of the time varying field, so that the permittivity depends on frequency.

On the other hand, biological materials are not magnetic, and therefore, the magnetic permeability μ can be assumed equal to the vacuum magnetic permeability ($\mu_0 = 4\pi \times 10^{-7} henry/m$). In the section 2.4, we discuss the properties of biological systems with more details.

One further constitutive relation can be considered as well. In a conducting material the electromagnetic field itself gives rise to currents. If the field strengths are not too large, we can assume a linear relationship between the field and the created current, so that Ohm's law holds. In this case, we have that

$$\mathbf{J} = \sigma \mathbf{E} + \mathbf{J}_a, \tag{2.12}$$

where σ is the conductivity of the medium, and the vector $\mathbf{J}_a$ is the applied current density. Using the constitutive relations (2.10)-(2.12) we can write (2.5) and (2.6) as:

$$\begin{aligned} \nabla \times \mathbf{E}(r) &= i\omega\mu_0 \mathbf{H}(r), & (2.13)\\ \nabla \times \mathbf{H}(r) &+ i\omega[\epsilon(r,\omega) + i\sigma(r,\omega)/\omega]\mathbf{E}(r) = \mathbf{J}_a(r)\ . & (2.14) \end{aligned}$$

Note that in (2.14) the conductivity term is combined with the permittivity, so we can generalize the permittivity in such a way that the conduction contributes to its imaginary part, and define the (relative) complex permittivity ϵ_r^* as:

$$\epsilon_0\, \epsilon_r^*(r,\omega) = \epsilon_0\, [\epsilon_r(r,\omega) + i\frac{\sigma(r,\omega)}{\epsilon_0\, \omega}]\ . \tag{2.15}$$

2.3 Scalar Maxwell's equation for TM polarized waves

Many interesting physical phenomena in electromagnetics can be described by a scalar approximation of the above vector equations (2.13)-(2.14). In our application, for example, this is the case in the situation in which the patient is lying facedown with the breast naturally extending through a hole in the examination table, and the breast is illuminated by TM polarized waves.

When the electromagnetic properties of the medium, ϵ and σ, do not vary in one direction, e.g., the z direction, the vector equations (2.13) and (2.14) can be reduced to two decoupled scalar equations. These two scalar

equations define two types of waves: transverse electric to z (TE polarized waves) and transverse magnetic to z (TM polarized waves). As a result, the z components of the electromagnetic field, E_z and H_z, can be used to characterize the TM and TE waves, respectively.

If we take the curl of Eq. (2.13), and substitute (2.14) into the result, we arrive at the following equation for the electric field:

$$\nabla \times \nabla \times \mathbf{E} - k^2 \mathbf{E} = i\omega\mu_0 \mathbf{J}_a, \tag{2.16}$$

where

$$k^2(r,\omega) = \omega^2 \mu_0 \epsilon_0 \left[\epsilon_r(r,\omega) + i\sigma(r,\omega)/\epsilon_0\,\omega\right] \tag{2.17}$$

is the squared complex wave number. If we now apply the vector identity $\nabla \times \nabla \times v = \nabla(\nabla \cdot v) - \triangle v$ to (2.16), we obtain:

$$\nabla(\nabla \cdot \mathbf{E}) - \triangle \mathbf{E} - k^2 \mathbf{E} = i\omega\mu_0 \mathbf{J}_a \ . \tag{2.18}$$

In the absence of charge, $\nabla \cdot \mathbf{D} = 0$. Then, from the constitutive relation (2.10) we have $\nabla \cdot \mathbf{E} = -(\mathbf{E} \cdot \nabla\epsilon)/\epsilon$. Introducing this formula into (2.18) we arrive at:

$$\nabla^2 \mathbf{E}(r) + k^2(r)\mathbf{E}(r) + \nabla[\frac{\mathbf{E}(r)\nabla\epsilon(r)}{\epsilon(r)}] = -i\omega\mu_0 \mathbf{J}_a(r) \ . \tag{2.19}$$

Let us now consider the case of TM polarized waves, where the z component of the magnetic field H_z is zero and $\mathbf{E} = (0, 0, E_z)$. Moreover, if the electromagnetic properties of the medium do not vary in the z direction, i.e., $\frac{\partial\epsilon(r,\omega)}{\partial z} = 0$, we can reduce the vector equation (2.19) to the scalar equation

$$\nabla^2 E_z(x,y) + k^2(x,y)E_z(x,y) = -q(x,y) \ , \tag{2.20}$$

for the z component of the electric field E_z. In (2.20), $q(x,y) = i\omega\mu_0 J_{a,z}(x,y)$ is the source.

Equation (2.20) is known as the Helmholtz equation for the z component of the electric field. From now on, we will use this equation to analyze the potentials and limitations of microwave imaging for the application of early breast cancer detection. To solve it, we impose the Sommerfeld radiation condition that guarantees that no waves enter into our domain coming from the infinity. In two dimensions this condition is:

$$\lim_{|\mathbf{x}|\to\infty} \sqrt{|\mathbf{x}|}(\frac{\partial E_z}{\partial|\mathbf{x}|} - ikE_z) = 0 \ , \tag{2.21}$$

where $\mathbf{x} = (x, y)$. Under this condition, which is represented as a suitable boundary condition in our numerical model, the Helmhotz equation has a unique solution.

2.4 Dispersion in biological tissue

The interaction between biological tissue and electromagnetic radiation is strongly influence by the inhomogeneities of the tissue (organic molecules, variation in water content, blood flow, ...). The dependence of this interaction on the frequency has been investigated both, from an empirical and a theoretical point of view. In this section we summarize one of the most widely used dispersion models for biological tissue: the Debye dispersion model.

As it has already been mentioned, the biological tissue does not respond instantaneously to an applied electromagnetic field. This is modeled by the complex permittivity [2]

$$\epsilon^*(\omega) = \epsilon_0\, \epsilon_r^*(\omega) = \epsilon_0\, [\epsilon_r'(\omega) + i\epsilon_r''(\omega)] \tag{2.22}$$

that depends on frequency (this frequency dependence is referred to as the dispersion property). In this expression the complex permittivity ϵ^* (hereafter, permittivity) is expressed as the product between the vacuum permittivity ϵ_0 and the relative complex permittivity ϵ_r (hereafter, relative permittivity). The real part of the relative permittivity, ϵ_r', is related to the stored energy within the medium, while the imaginary part ϵ_r'' is related to the loss of energy within the medium which attenuates the propagation of electromagnetic waves in the medium.

Biological materials contain a large amount of water (typically, between 70% and 80% in soft tissue as muscle, skin, fat, fiber, ...). Hence, the dielectric properties of these materials are mainly dictated by the dielectric properties of water. A water molecule has a permanent dipole, which has the effect that the frequency dependence of the relative permittivity, $\epsilon_r(\omega)$, and of the conductivity, $\sigma(\omega)$, can be approximated by the single-pole Debye relaxation model of the following form [43]:

$$\epsilon_r(\omega) + i\frac{\sigma}{\omega\epsilon_0} = \epsilon_\infty + \frac{\epsilon_s - \epsilon_\infty}{1 - i\omega\tau} + i\frac{\sigma_s}{\omega\epsilon_0}\ , \tag{2.23}$$

where ϵ_∞ is the permittivity at the limit of very high frequency, ϵ_s is the static permittivity, i.e., the low frequency limit, and σ_s is the static conductivity. Moreover, τ is the characteristic relaxation time. Since τ is similar

[2] We point out that the choice of sign for the imaginary part of the complex permittivity depends on the convention regarding whether the time dependence is $exp(-i\omega t)$, as it is usual in physics, or $exp(+i\omega t)$, as it is usual in engineering literature. The signs used in this thesis correspond to those commonly used in physics literature. It is easy to convert from one of these conventions to the others such that we will not dwell much on the small differences in the formulas which we achieve.

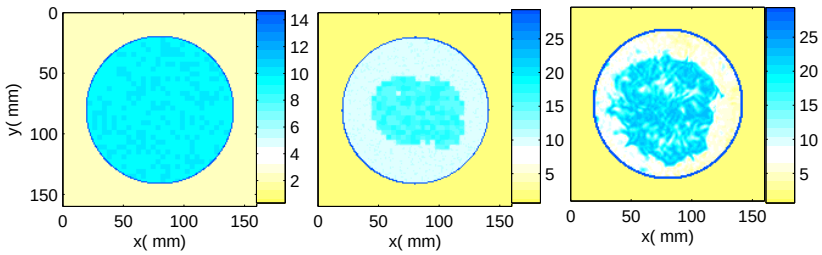

Figure 2.1: Three examples of numerical breast models used in the thesis. Left image: a simple model consisting of only two tissue types (healthy tissue and skin). Center image: a more complicated model with an internal structure created artificially (the dark blue region is fibroglandular tissue and the light blue region is fatty tissue). Right image: a breast model based on magnetic resonance imaging (MRI) data.

for different biological tissues in the microwave regime [40], it will be treated in this thesis (without loss of generality of the results) as a constant ($\tau = 7.0$ ps) everywhere in the interior of the breast. Therefore, for each pixel or region inside the numerical breast phantom used to generate the synthetic data, there are three tissue parameters in our Debye model: ϵ_∞, ϵ_s, and σ_s.

In (2.23), the quantity $\Delta\epsilon = \epsilon_s - \epsilon_\infty$ can be interpreted as the *relaxation strength* and it reflects the response of the biological material as a whole, i.e., the coupling of all dipoles in the system that leads to the response. Although in this thesis we will only consider Eq. (2.23) to model dispersion in tissue, one can also take into account other molecules in the biological tissue besides water molecules and generalize Eq. (2.23) to

$$\epsilon_r(\omega) + i\frac{\sigma}{\omega\epsilon_0} = \epsilon_\infty + \sum_{n=1}^{N} \frac{\epsilon_{s_n} - \epsilon_{\infty_n}}{1 - i\omega\tau_n} + i\frac{\sigma_{s_n}}{\omega\epsilon_0} \ . \tag{2.24}$$

In this equation, ϵ_{∞_n}, ϵ_{s_n}, σ_{s_n} and τ_n are the high frequency permittivity, the low frequency permittivity, the static conductivity, and the relaxation time, each of the $n-th$ molecule type.

2.5 Breast models

The normal breast has a complex tree-like architecture, composed of fibroglandular and fatty tissues, and surrounded by the skin layer. The different

breast structures can be divided in three groups, categorized by the adipose-fibroglandular tissue contents [86]: $30-70\%$, $50-50\%$ and $70-30\%$. The large majority of female breasts belong to the third category.

In this section we present the numerical breast models used in this thesis. The breast models provide macroscopic characteristics of various regions, including point and structural properties. The 2D synthetic breast models (with simulated abnormalities) that we use for testing our shape-based approach are: (i) a simple model with only two types of tissue (healthy tissue and skin), (ii) a model with three types of tissue (fat, fibroglandular tissue and skin) in which we choose an arbitrary shape for the fibroglandular region, and (iii) an MRI-derived breast model which incorporates published information on the typical spatial arrangement of the different tissue types. To generate simulated data and assess the possibilities and potentials of our shape-based reconstruction technique, we introduce a small tumor at different depths below the skin in these models.

Although there is significant variation in the dielectric properties of normal breast tissue due to its strong heterogeneity and its complex interior network, an often used assumption in microwave breast imaging is that the breast is approximately homogeneous wherein the interior healthy tissue is represented by the same set of (average) dielectric properties, possibly (but not always) combined with another value for the surrounding skin.

1. Under this assumption, the first numerical breast model consists of only healthy tissue surrounded by a thin layer of skin as it is shown in the left image of Fig. 2.1. To model the breast heterogeneity, the breast tissue contains random variations in the dielectric properties of up to $\pm 5\%$ over 4 millimeter cubes. A very similar breast model has been used, for example, by [36, 96, 26]. We will also consider this simple model in chapter 3 to analyze the potentials and limitations of microwave breast cancer detection.

As we will see in the next chapter, the complex interior network of the breast tissue is an important issue to take into account when trying to obtain good reconstructions and to avoid false positives.For this reason, in this thesis we intend to keep the complexity of the breast model as realistic as possible. We will consider a 2D model with two distinct tissue types (fatty and fibroglandular) in the interior of the breast, in addition to the surrounding skin. We will use two different models of this kind:

2. A model in which the fibroglandular region is created artificially (see an example in the center image of Fig.2.1). The average values chosen for

both the fatty and the fibroglandular tissue are taken from references [8, 26, 81]. To model anatomical heterogeneity of the biological tissue we add random variations of $\pm 15\%$ in form of fluctuations, distributed over $4 \times 4\ mm^2$ square pixel blocks, centered in these values in both tissue types.

3. An MRI-derived model (based on real MRI images published recently in the literature on breast imaging) containing not only a realistic spatial arrangement of the different tissue types (see an example in the right image of Fig.2.1), but also the heterogeneities of these tissues. In this model the MRI pixel intensities in the heterogeneous tissues are mapped to the Debye parameters so that the MRI image is used as a template of the heterogeneity of the breast tissue. Hence, these models represent the high heterogeneity encountered in real situations. MRI based breast models have been used, among others, by [104, 26, 65, 67].

Before concluding this section, we state a few observations about the dielectric parameters in the Debye model, and the numerical implementation of our breast models in the following.

Since τ is similar for different biological tissue types in the microwave regime [40], it will be treated as a constant ($\tau = 7.0$ ps) everywhere in the breast interior. Therefore, for each pixel or region inside the numerical breast phantom used to generate the synthetic data, there are three parameters in our model: ϵ_∞, ϵ_s, and σ_s.

In general, these three parameters need to be reconstructed for each pixel inside the breast model from the microwave data. However, in realistic breast models these three parameters are not completely arbitrary but correspond to typical breast tissue values. This observation motivates us to simplify our breast model assuming that there exists some functional relation between these three parameters. In Table I of reference [104], for example, we observe that the dispersion parameters of the fibroglandular tissue approximately follow a linear relation. We can write:

$$\epsilon_\infty = a_1 + b_1 \epsilon_s \ , \tag{2.25}$$

$$\sigma_s = a_2 + b_2 \epsilon_s \ , \tag{2.26}$$

with $a_1 = 7.7$, $b_1 = -0.067$, $a_2 = 0.03$, $b_2 = 0.01$. Consequently, in our models we only have to determine one parameter (ϵ_s) at each pixel or region within the breast, and the other two parameters are then given using (2.25)-(2.26). We note that functional relations different from (2.25)-(2.26) (i.e.

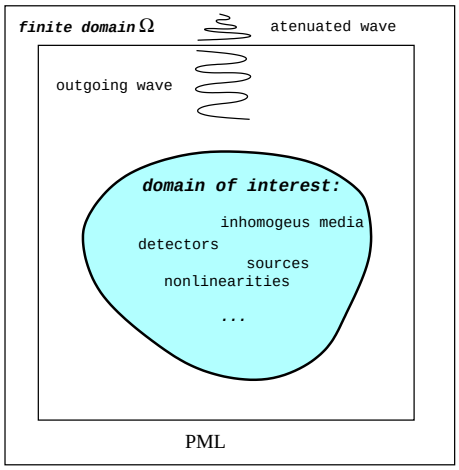

Figure 2.2: The Sommerfeld raditation condition in the infinite domain is represented by absorbing Perfectly Matched Layers (PML).

different from those given in [104]) can be used as well in our technique without any further changes in the algorithm. From a mathematical viewpoint, the assumption (2.25)-(2.26) introduces a constraint into the optimization problem and leads to a subspace search strategy in the space of parameters ϵ_∞, ϵ_s, and σ_s.

2.6 Numerical Method

We have shown in the subsection 2.3 that our model can be described mathematically by the Helmholtz equation (2.20) supplemented by the Sommerfeld radiation condition (2.21) at infinity. In this equation the dielectrical characteristics of different media (fatty and fibroglandular tissues, skin, tumor) are represented by the squared wavenumber k. The electromagnetic sources are characterized by the source term q. In order to obtain a unique solution for the forward problem, the Sommerfeld radiation condition restricts the solutions of the Helmholtz equation in a manner that the scattered wave is only outgoing, and there are no waves incoming from infinity. In this section we describe how we model and solve the Helmholtz equation taking into account this condition numerically by introducing so-called Perfectly Matched Layers (PML).

2.6.1 Perfectly Matched Layers (PML).

Since the Sommerfeld radiation condition restricts the scattered wave to being only of the outgoing type, the physical formulation of the inverse problem is done for an infinite domain. This condition is very difficult to implement by the classical finite-differences or finite elements schemes. It is obvious, that in a given computer implementation we typically have to simulate the original Sommerfeld condition on a numerical grid defined on a finite computational subdomain Ω. But in finite domains we need explicit boundary conditions, for example of the Dirichlet or Neumann type, for terminating the computational domain. These boundary conditions typically will have the numerical effect of introducing artificially reflected waves incompatible with the Sommerfeld radiation condition. To solve this problem, we use the technique of *Perfectly Matched Layers (PML)* introduced originally by Berenger [5]. The basic idea of the PML approach is to add to the computational domain Ω an artificial layer surrounding it. Inside this layer the conductivity increases from the inner boundary to the outer frontier of the PML, thereby gradually (i.e. ideally without numerical reflections) absorbing the outgoing waves until their magnitude has decreased sufficiently. Then, at the outer boundary of the domain augmented by the PML, any suitable boundary condition can be applied without significant reflection due to the smallness of the waves at those points. For a visualization, see Fig. 2.2.

Formally, the equation to solve inside the PML is [30]:

$$c(\mathbf{x})\nabla c(\mathbf{x})\nabla E(\mathbf{x}) + k^2(\mathbf{x})E(\mathbf{x}) = 0. \tag{2.27}$$

Here, $c(\mathbf{x}) \equiv c(\xi) = \dfrac{\epsilon_0\omega}{\epsilon_0\omega + is(\xi)}$, ξ is the distance from a given point inside the PML to its inner boundary, ω is the angular frequency, ϵ_0 is the dielectric permittivity of free space, and i is the imaginary unit. The function $s(\xi)$ [3] characterizes the absorption power inside the PML, which increases gradually towards the exterior boundary of Ω. The wave amplitude decreases towards the outer PML boundary until it reaches values close to zero. Therefore, we can apply the homogeneous Dirichlet condition at the exterior boundary of the PML without problems. See Fig. 2.2 for a visualization of this general procedure.

[3] Note that $s(\xi)$ resembles a conductivity term

2.6.2 Discretization of the Helmholtz equation

Let us consider our 2-D domain as a square grid Ω=$[0, L] \times [0, L]$. Using the PML approach, the mathematical model of our problem can be described as:

$$\begin{cases} \dfrac{\partial^2 E}{\partial x^2} + \dfrac{\partial^2 E}{\partial y^2} + k^2(x,y)E(x,y) = q(x,y), & \text{(x,y)} \in \Omega \backslash \text{PML} \backslash \partial\Omega \\ c(x)\dfrac{\partial}{\partial x}\Big(c(x)\dfrac{\partial E}{\partial x}\Big) + c(y)\dfrac{\partial}{\partial y}\Big(c(y)\dfrac{\partial E}{\partial y}\Big) + k^2(x,y)E(x,y) = 0, & \text{(x,y)} \in \text{PML} \\ E(x,y) = 0, & \text{(x,y)} \in \partial\Omega \end{cases} \tag{2.28}$$

To solve this problem numerically, we use the second order centered finite differences scheme in a homogeneous mesh characterized by a spatial step size h.

The PML is chosen to have N_{PML} layers on each side, and a suitable choice of the absorption function $s(\xi)$ is given by the following parametric function

$$s(\xi) = s_f\Big(\frac{\xi}{hN_{PLM}}\Big)^p, \tag{2.29}$$

where the parameters s_f and p are chosen in order to obtain minimal reflection of the waves. See the details given further below in this section.

Given a square domain of size $L \times L\text{cm}^2$, the total number of points in each direction x and y for our computational grid is $N = L/h$, and using the usual notation $x_i = i \times h$, $y_i = i \times h$, $E_{i,j} = E(x_i, y_j)$, we obtain the discrete version of Eq. 2.28 as

$$\begin{cases} (1 - h^2k_{i,j}^2)E_{i,j} + E_{i+1,j} + E_{i-1,j} + E_{i,j+1} + E_{i,j-1} = h^2 q_{i,j} \\ \text{for } i,j = [N_{PLM}, N - N_{PML}] \\ \\ (c_{i,j}^2 - h^2k_{i,j}^2)E_{i,j} + c_{i,j}^2(E_{i+1,j} + E_{i-1,j} + E_{i,j+1} + E_{i,j-1}) + \\ 4c_{i,j}\Big((c_{i+1,j} - c_{i-1,j})(E_{i+1,j} - E_{i-1,j}) + (c_{i,j-1} - c_{i,j-1})(E_{i,j+1} - E_{i,j-1})\Big) = \\ = 0 \\ \text{for } i,j = [0, N_{PML}] \text{ and } i,j = [N - N_{PML}, L] \\ \\ E_{i,j} = 0, \\ \text{for } i,j = 0 \;\; i,j = L \end{cases} \tag{2.30}$$

This scheme can be written in a corresponding matrix form as $A\overrightarrow{E} = \overrightarrow{q}$ [91]. Its solution $\overrightarrow{E}$ discribes the electric field $E_{i,j}$ in each grid point of the

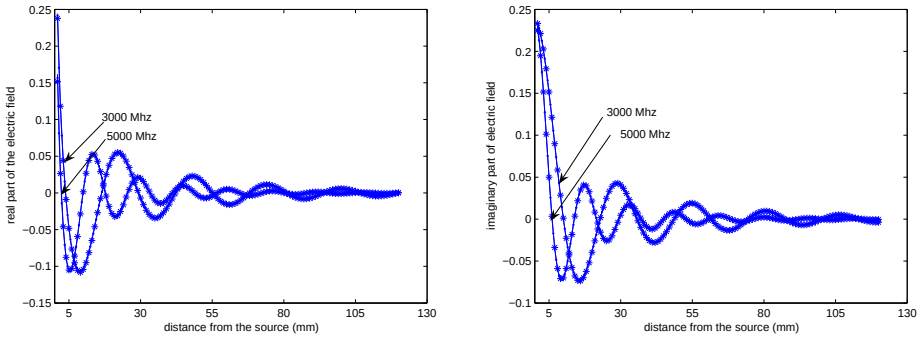

Figure 2.3: Real (left image) and imaginary (right image) part of the calculated electric field calculated with our computational approach for a homogeneous domain surrounded by PML (with $s_f = 5.4$ and $p = 2.0$) and compared to the corresponding analytical infinite space solution (using Green's functions): -$*$- line is the exact Green's function solution, -$\bullet$- line is the solution for step $h = 0.0005$ m, solid line is the solution for step $h = 0.001$ m. We use the frequencies 3 GHz and 5 GHz. The homogeneous domain characteristics are static permittivity equal to 15, conductivity equal to $0.21 S/m$ and infinite permittivity equal to 6.66.

mesh.

In our problem, the value of the PML parameters s_f and p have been determined empirically (see also [60, 91] for related approaches) as $s_f = 5.4$ and $p = 2.0$ by comparing numerically calculated waves for a homogeneous domain surrounded by PML with analytical infinite space solutions. Some of the results are displayed in Fig. 2.3. In more details, in order to check the accuracy of our numerical model, we compared the exact solution, obtained analytically, with the solution calculated by our numerical scheme (using the so-called 'eye-ball' norm, i.e. checking visually their agreement). Here, we have considered a homogeneous domain, characterized by the static permittivity value equal to 15, conductivity $0.21 S/m$ and infinite permittivity 6.66. We introduced a unitary source, emitting at frequencies 3 and 5 GHz, and being located at 2 cm distance from the boundary of the domain. We solved analytically the Helmholtz equation for all the points on a horizontal line in the direction to the opposite side of Ω, using the exact solution described by Green's functions. For the numerical solution, we used two different step sizes: $h = 0.0005$ m and $h = 0.001$ m. For each mesh, the numbers of PML layers were 20 and 10, respectively. The values of the PML parameters which were finally chosen and for which cross sections are displayed in Fig. 2.3 are

$s_f = 5.4$ and $p = 2.0$. The figure shows the real and imaginary parts of the 'analytically' and 'numerically' calculated electric field, which are in good agreement with each other.

Chapter 3

Basic inverse problem: a simple breast model

3.1 Introduction

To understand better the potentials and limitations of our shape-based approach for microwave breast imaging, we first analyze in this chapter the performance of our algorithm for a simple breast model. The model consists of only one type of tissue in the interior of the breast (besides the possible tumor) and of the surrounding skin layer, as shown in the left image of Fig. 2.1 in section 2.5. Furthermore, we will consider that the relaxation time τ in the Debye dispersion model (2.23) is negligible, so that the complex (relative) permittivity is given by

$$\epsilon_r^*(\mathbf{x};\omega) = \epsilon(\mathbf{x}) + i\sigma(\mathbf{x})/\omega\epsilon_0 \ , \tag{3.1}$$

where, for simplicity, we have written $\epsilon = \epsilon_s$, $\sigma = \sigma_s$, and $\mathbf{x} = (x, y)$. Therefore, for each pixel inside the numerical breast phantom there are two parameters in this model: ϵ, and σ. In this chapter, we will assume in the inversion process that the average dielectric properties of the healthy tissue are known. The thickness of the skin layer and its dielectric properties are also assumed to be known. In other words, the unknowns of the inversion are only the main characteristics of the possible tumor: its location, its shape, and its dielectric properties.

As described in section 2.3, for modelling wave propagation we consider the scalar Helmoltz equation

$$\nabla^2 u(\mathbf{x}) + \kappa(\mathbf{x})\, u(\mathbf{x}) = -q(\mathbf{x}) \tag{3.2}$$

in a computational domain Ω. Here, we have used the notation $u = E_z$ and $\kappa = k^2 = \omega^2 \mu_0 \epsilon_0 \epsilon_r^*$. Equation (3.2) is supplemented by the standard Sommerfeld radiation condition in two dimensions

$$\lim_{|\mathbf{x}|\to\infty} \sqrt{|\mathbf{x}|}\left(\frac{\partial u}{\partial |\mathbf{x}|} - iku\right) = 0 \ . \tag{3.3}$$

Equations (3.2)-(3.3) define the *direct problem* describing wave propagation under the assumption that the dielectric properties of the medium, defined by $\kappa(\mathbf{x})$, are known. Since we use a Sommerfeld radiation condition as boundary condition, the computational domain Ω is discretized including appropriate absorbing boundary conditions (PML) as it is described in section 2.6.

The goal of this chapter is to verify whether a shape-based approach is able to estimate the important key characteristics of the tumors in a stable and reliable way. Being able to recover the dielectric properties of the tumor could lead to a higher specificity between benign and malignant tissues, and may lead to a new strategy for determining whether a normal tissue is in the process of becoming malignant.

3.2 Formulation of the inverse problem

In the inverse problem, we assume that the spatial distribution of p different sources q_j $(j = 1, \ldots, p)$ is given. These sources illuminate the breast, one after the other, with various angular frequencies ω_l $(l = 1, \ldots, L)$, and the data are gathered at the detector positions $\mathbf{x}_m$ $(m = 1, \ldots, M)$ around the breast. For simplicity, in our numerical experiments the detector positions coincide with the source positions.

For each source

$$q_j = J_j \delta(\mathbf{x} - \mathbf{x}_j) \ , \tag{3.4}$$

where J_j is the source strength, and for each frequency ω_l we define the vector in the data space $D_j = \mathbb{C}^M$

$$\tilde{G}_{jl} = (\tilde{u}_{jl}(\mathbf{x}_1), \tilde{u}_{jl}(\mathbf{x}_2), \ldots, \tilde{u}_{jl}(\mathbf{x}_M))^T \ \in D_j \tag{3.5}$$

that collects the data at all the detector positions corresponding to a single experiment with one source and one frequency. In (3.5), the fields $\tilde{u}$ solve (3.2)-(3.3) with the correct spatial distribution of the dielectric properties contained in $\tilde{\kappa}(\mathbf{x})$, i.e.,

$$\nabla^2 \tilde{u}_{jl}(\mathbf{x}) + \tilde{\kappa}_l(\mathbf{x})\, \tilde{u}_{jl}(\mathbf{x}) = -q_j \ , \tag{3.6}$$

with

$$\tilde{\kappa}_l(\mathbf{x}) = \omega_l^2 \mu_0 \epsilon_0 [\tilde{\epsilon}(\mathbf{x}) + i\tilde{\sigma}(\mathbf{x})/\omega_l \epsilon_0] \ . \tag{3.7}$$

We can also define for each source q_j the linear measurement operator M_j acting on the solutions of (3.2)-(3.3) as

$$M_j\, u = (u(\mathbf{x}_1), u(\mathbf{x}_2), \ldots, u(\mathbf{x}_M))^T \quad \in D_j, \tag{3.8}$$

and write

$$M_j\, \tilde{u}_{jl} = \tilde{G}_{jl} \qquad j = 1, \ldots, p, \quad l = 1, \ldots, L\,. \tag{3.9}$$

Finally, we gather these data sets (for all sources q_j, and all frequencies ω_l) in the array

$$\tilde{G} = (\tilde{G}_{11}, \tilde{G}_{12}, \ldots, \tilde{G}_{pL}) \ . \tag{3.10}$$

Then, the objective of our inverse problem is to reconstruct the unknown parameter distribution $\tilde{\kappa}(\mathbf{x})$ in the breast interior using the measured data $\tilde{G}$ as in (3.10).

We point out, again, that in the application of microwave imaging for the early detection of small tumors in the breast we are not interested in reconstructing a complete and detailed image of the breast interior, but to answer the question of whether or not there is a tumor and to reconstruct its key properties. In other words, we are interested in the localization, size and dielectric properties of the possible tumor. To this end, we will follow a shape-based approach that uses level set techniques as it is explained in the next sections.

We want to introduce one more operator which will be useful in the following. For some guess κ, and given the measured data $\tilde{G}_{jl}$, the residual operator

$$R_{jl} : P \longrightarrow D_j \ , \qquad\qquad R_{jl}[\kappa] = M_j u_{jl}[\kappa] - \tilde{G}_{jl} \tag{3.11}$$

describes the mismatch between the physically measured data $\tilde{G}_{jl}$ and the data corresponding to the guess κ in the parameter space $P = L_2(\Omega)$. In the inverse problem, we ideally want to find a spatial distribution $\hat{\kappa}$ in P such that

$$R_{jl}[\hat{\kappa}] = 0 \quad \text{for all} \quad j, l \ . \tag{3.12}$$

Certainly, for the 'true' squared complex wavenumber $\tilde{\kappa}$, (3.12) holds if the data are in the range of M_j. Most likely this is not the case if we use real

data, so we generalize our criterion for a solution to the inverse problem defining the least squares cost functional

$$\mathcal{J}_{jl}[\kappa] \;=\; \frac{1}{2}\|R_{jl}[\kappa]\|^2_{D_j}, \tag{3.13}$$

and searching for a minimizer of this cost functional. This cost functional defines the difference between the predicted data, i.e., the solution of the direct problem for the predicted model (as described by κ), and the measurements for the 'real' model. In (3.13), $\| \ \|_{D_j}$ represents the norm in the data space D_j for frequency j.

We recall that the goal in this chapter is to localize a possible small tumor inside the breast, and to estimate its shape and its dielectric properties. To this end, we will formulate the inverse problem as a shape reconstruction problem and cast it in a form that makes use of the level set representation of objects, as it will be explained further below. In this formulation, the unknowns will be (i) the level set function defining the location and geometry of the tumor, and (ii) the permittivity ϵ_i inside the detected tumor. The other dielectric properties (those for the healthy tissue and the conductivity σ_i inside the tumor) are assumed to be known.

3.3 Pixel-based gradient direction of $\mathcal{J}_{jl}$

To solve the shape reconstruction problem we need to introduce first the (pixel-based) gradient direction of the cost functional

$$\mathcal{J}_{jl}[\kappa] \;=\; \frac{1}{2}\|R_{jl}[\kappa]\|^2_{D_j} \;=\; \frac{1}{2} < R_{jl}[\kappa], R_{jl}[\kappa] >_{D_j} \quad . \tag{3.14}$$

We assume that the residual operator (3.11) admits the expansion

$$R_{jl}[\kappa + \delta\kappa] = R_{jl}[\kappa] + R'_{jl}[\kappa]\delta\kappa + O(||\delta\kappa||^2_P), \tag{3.15}$$

where $R'_{jl}[\kappa]$ is the linearized residual operator, which is closely related to the 'sensitivity functions' of the parameter profile with respect to the data [1]. In these expressions, $<>_P$ and $\| \ \|_P$ represent the inner product and the

[1]The (linearized) variations of model output measurements (the system response) with respect to parameter variations can in an intuitive way be described by these sensitivity functions. They show the (linearized) change in the data caused by a unit variation of an individual model parameter

norm in the parameter space, respectively. The linearized residual operator $R'_{jl}[\kappa]$ is defined by

$$R'_{jl}[\kappa] : P \longrightarrow D_j \ , \qquad R'_{jl}[\kappa]\delta\kappa = M_j v_{jl} \ , \tag{3.16}$$

where v_{jl} solves the linearized equation

$$\nabla^2 v_{jl}(\mathbf{x}) + \kappa(\mathbf{x})\, v_{jl}(\mathbf{x}) = -\delta\kappa\, u_{jl} \quad \text{in} \quad \Omega \ . \tag{3.17}$$

Here u_{jl} is the solution to (3.2)-(3.3). Equation (3.17) can be derived by perturbing (3.2) according to $\kappa \to \kappa + \delta\kappa$ and $u_{jl} \to u_{jl} + v_{jl}$ and neglecting terms of higher than linear order in $\delta\kappa$ and v_{jl}.

To derive an expression for the gradient of $\mathcal{J}_{jl}$, we substitute (3.15) in (3.14) for $\kappa \to \kappa + \delta\kappa$ and get

$$\mathcal{J}_{jl}[\kappa + \delta\kappa] = \mathcal{J}_{jl}[\kappa] + \underbrace{\mathtt{Re}\left[< \mathbf{grad}_\kappa \mathcal{J}_{jl}, \delta\kappa >_P\right]}_{\delta\mathcal{J}_{jl}} + O(||\delta\kappa||_P^2) =$$

$$\mathcal{J}_{jl}[\kappa] + \mathtt{Re}\left[< R'_{jl}[\kappa]^* R_{jl}[\kappa], \delta\kappa >_P\right] + O(||\delta\kappa||_P^2) \, . \tag{3.18}$$

From (3.18), we can extract the gradient and write

$$\mathbf{grad}_\kappa \mathcal{J}_{jl}[\kappa] = R'_{jl}[\kappa]^* R_{jl}[\kappa] \ . \tag{3.19}$$

In these equations, $R'_{jl}[\kappa]^*$ is the adjoint operator of $R'_{jl}[\kappa]$ with respect to the spaces P and D [84]. The adjoint operator $R'_{jl}[\kappa]^*$ is defined by

$$\langle R'_{jl}[\kappa]\delta\kappa, \rho\rangle_{D_j} = \langle \delta\kappa, R'_{jl}[\kappa]^*\rho\rangle_P \ , \tag{3.20}$$

where $\langle \ , \ \rangle_{D_j}$ and $\langle \ , \ \rangle_P$ denote the inner products in the data and parameter spaces, respectively, and ρ is a vector in the data space D_j. We assume that the inner products in the parameter space P and in the data space D_j are given by

$$\langle f, g\rangle_{D_j} = \sum_{m=1}^{M} f_m\, \bar{g}_m \ ; \quad \langle A, B\rangle_P = \int_\Omega A\, \bar{B}\, d\vec{x} \ , \tag{3.21}$$

where $f_m = f(\mathbf{x}_m)$ and $g_m = g(\mathbf{x}_m)$, $m = 1, \ldots, M$, are complex numbers defined at the detector positions $\mathbf{x}_m$, and the overline means 'complex conjugate'.

An efficient way to compute the (pixel-based) *gradient direction* of $\mathcal{J}_{jl}$ in κ is to use the adjoint formulation. The following adjoint form of the linearized residual operator is derived in [84]. We give here the main result.

The gradient direction of $\mathcal{J}_{jl}$ in κ is given by

$$\mathbf{grad}_{\kappa}\mathcal{J}_{jl} = -\frac{1}{\omega_l^2\epsilon_0\mu_0}\, u_{jl}\, z_{jl} \ , \tag{3.22}$$

where u_{jl} solves (3.2)-(3.3), and z_{jl} solves the following adjoint equation

$$\nabla^2 z_{jl} + \kappa_l z_{jl} = \sum_{m=1}^{M} \overline{M_j u_{jl}(\mathbf{x}_m) - \tilde{G}_{jl}(\mathbf{x}_m)} \quad \text{in } \Omega \ . \tag{3.23}$$

Note that z_{jl} is similar to the so-called backpropagated wave [84]. We will use in the following this *pixel-based* formulation to define a shape evolution which gradually changes a tumor shape into a descent direction until the cost is minimized.

3.4 Level set representation of tumor shape

To evaluate the possibilities of our approach for microwave breast imaging we artificially introduce simulated tumors of different characteristics in our numerical experiments (see an example in the top left image of Fig. 3.1). Hence, in this chapter, the breast interior is composed of only two types of tissue: the healthy tissue and the tumorous tissue.

An important assumption of our model is that the healthy and tumorous tissue are well distinguished, so that there is an interface between them. Furthermore, we will assume during the reconstruction that the squared complex wavenumber $\kappa(\mathbf{x}) = \omega^2\mu_0\epsilon_0[\epsilon(\mathbf{x}) + i\sigma(\mathbf{x})/\omega\epsilon_0]$ in the breast interior is piecewise constant with only two possible values, namely one for the healthy tissue and another for the tumor.

For modeling the shape S of the tumor we introduce a sufficiently smooth level set function ϕ such that

$$\kappa(\mathbf{x}) = \begin{cases} \kappa_i(\mathbf{x}) & \text{inside } S \text{ where } \phi(\mathbf{x}) \le 0 \\ \kappa_e(\mathbf{x}) & \text{outside } S \text{ where } \phi(\mathbf{x}) > 0 \ . \end{cases} \tag{3.24}$$

Here, $\kappa_i(\mathbf{x})$ and $\kappa_e(\mathbf{x})$ describe the dielectric properties inside and outside a tumor of shape S, respectively. The boundary of the tumor, δS, consists of all the points where $\phi(\mathbf{x}) = 0$, and the tumor itself consists of all points where $\phi(\mathbf{x}) \le 0$.

We will indicate the dependence (3.24) of the parameters κ on the level set function ϕ by

$$\kappa = \kappa[\phi] \ . \tag{3.25}$$

Note that there are in general many possible level set functions which can be used for describing the same tumor, and that every continuous function uniquely specifies a tumor by the above definitions. The main advantage of this implicit representation of the unknown shape by a level set function consists of its capability of automatically splitting and merging shapes during the reconstruction, and, in its generalized form as employed here (in the first part of our algorithm), to create and eliminate an arbitrary number of tumors automatically at any step of the algorithm if this is required by the data.

3.5 The shape reconstruction problem

With the above definitions, we can formulate the shape reconstruction problem using level sets as follows.

Assuming that the dielectric properties of the tumor and the healthy tissue (contained in κ_i and κ_e, respectively) are known, and given some data $\tilde{G}$ as in (3.10), find a level set function $\hat{\phi}$ such that $\kappa[\hat{\phi}]$ reproduces the data.

To solve the shape reconstruction problem for the tumor we will follow a time evolution approach. The goal will be to find an evolution law, of the form

$$\frac{d\phi}{dt} \ = \ f(\mathbf{x}, t) \ , \tag{3.26}$$

for the unknown level set function ϕ which reduces, and eventually minimizes, the least-squares cost functional (3.13). Equation (3.26) describes the evolution of the shape S during an artificial time t. The forcing term $f(\mathbf{x}, t)$ is an unknown that needs to be determined from the data $\tilde{G}$ in each (artificial) *time step*. It will be chosen to point into some descent direction for the cost functional (3.13). We note that only the normal component of a velocity field is needed for moving the shape S (the tangential component does not contribute to the shape evolution). Hence, here and in the following the scalar $f(\mathbf{x}, t)$ will denote the normal component of the velocity.

In order to find such a descent direction, we formally differentiate $\mathcal{J}(\kappa(\phi(t)))$ with respect to the artificial time t and apply the chain rule. We get

$$\frac{d\mathcal{J}}{dt} \ = \ \frac{\partial \mathcal{J}}{\partial \kappa} \frac{\partial \kappa}{\partial \phi} \frac{d\phi}{dt} \ = \mathtt{Re}\left[< \mathbf{grad}_{\kappa} \mathcal{J}, \frac{\partial \kappa}{\partial \phi} \frac{d\phi}{dt} >_P \right] \ =$$

$$\mathtt{Re} \int_{\Omega} R'[\kappa]^* R[\kappa] \, \overline{(\kappa_e - \kappa_i)} \delta(\phi) \, f(\mathbf{x}, t) \, d\mathbf{x} \,, \tag{3.27}$$

where Re indicates the real part of the corresponding quantity. In (3.27), $R'[\kappa]^*$ denotes the formal adjoint of the linearized residual operator $R'[\kappa]$ and the expression $R'[\kappa]^* R[\kappa]$ coincides with the pixel-based Frechét derivative of the parameter-to-data mapping explained in section 3.3.

Using Eq. (3.27), we can select a descent direction for the cost functional by choosing [31]

$$f_1(\mathbf{x}, t) \; = \; - \mathtt{Re} \left(\overline{(\kappa_e - \kappa_i)} \, R'[\kappa]^* R[\kappa] \right) \quad \text{for all } \mathbf{x} \text{ s.t. } \phi(\mathbf{x}) = 0. \tag{3.28}$$

Note that so far the descent direction (3.28) has been specified only at the boundary shape where $\phi(\mathbf{x}) = 0$, so we need to determine a suitable 'extension velocity' to solve (3.26). A trivial extension of the velocity is directly suggested by Eq. (3.27). Using the fact that $\delta(\phi) \geq 0$ we can define

$$f_2(\mathbf{x}, t) \; = \; - \mathtt{Re} \left(\overline{(\kappa_e - \kappa_i)} \, R'[\kappa]^* R[\kappa] \right) \chi_{\phi,d}(\mathbf{x}) \quad \text{for all} \quad \mathbf{x} \in \Omega \,, \tag{3.29}$$

where $\chi_{\phi,d}(\mathbf{x})$ is a 'narrowband' function that approximates $\delta(\phi)$. The narrowband function which is one in a small neighborhood of the shape boundary and zero elsewhere is defined as:

$$\chi_{\phi,d}(\mathbf{x}) \; = \; \begin{cases} 1 & \text{for all} \quad \mathbf{x} \in \Omega \quad \text{s.t} \quad |\mathbf{x}_0 - \mathbf{x}| < d \quad \text{and} \quad \phi(\mathbf{x}_0) = 0 \\ 0 & \text{otherwise.} \end{cases} \tag{3.30}$$

We point out that the parameter d defines the degree of the approximation. As it will be explained next, during the first stage of our shape reconstruction algorithm we will choose to neglect the narrowband function completely so that

$$f_3(\mathbf{x}, t) \; = \; - \mathtt{Re} \left(\overline{(\kappa_e - \kappa_i)} \, R'[\kappa]^* R[\kappa] \right) \quad \text{for all} \quad \mathbf{x} \in \Omega \,. \tag{3.31}$$

This search direction $f(\mathbf{x}, t)$ has the property that it can be applied even if there is no initial shape available when starting the algorithm (expression (3.31) is defined and typically non-zero in the whole domain Ω). Therefore, it allows for the creation of objects at any point in the domain, by lowering a positive-valued level set function until its values become negative. This property is useful for avoiding certain types of local minima which often occur in level set formulations that are solely based on the propagation of an already existing shape (where the counterpart to expression (3.31) is zero or almost zero at large parts of Ω). We refer to the discussion given in [31] on the different extension velocities used in the literature.

Numerically discretizing (3.26) by a straightforward finite difference discretization of the time derivative with time-step $\delta t^{(n)} > 0$ in step n, and interpreting $\phi^{(n+1)} = \phi(t^{(n)} + \delta t^{(n)})$ and $\psi^{(n)} = \psi(t^{(n)})$ yields the iteration rule

$$\phi^{(n+1)} \;=\; \phi^{(n)} \;+\; \delta t^{(n)}\, f^{(n)}(\mathbf{x}), \quad \phi^{(0)} = \phi_0. \tag{3.32}$$

Regularization and smoothing.

So far we have not really insisted in the fact that our level set function ϕ should be sufficiently smooth inside the domain of interest. The level set function ϕ defines the tumor which may be very small (milliliter sized). Our experience has shown us the need of applying some smoothing to the updates in each step of the algorithm. Otherwise, undesired small artifacts appear during the reconstruction process that make it difficult the reliably detect these small tumors.

In our regularization approach we enforce that the updates to the level set function describing the shapes are smoothly varying to a certain degree. Let $\Psi = R'[\kappa]^*\zeta$ be the update for some residual vector $\zeta \in D_j$ that takes into account the sensitivity map of the inverse problem. Then, we can convolve these (unregularized) updates Ψ calculated by $R'[\kappa]^*\zeta$ with a Gaussian kernel of variance $\sigma > 0$

$$f_\sigma(x) \;=\; \frac{1}{4\pi\sigma} \exp\left(-\frac{|x|^2}{4\sigma}\right) \tag{3.33}$$

which produces the smoothed update

$$\hat{\Phi} \;=\; f_\sigma * \Psi \;=\; \int f_\sigma(x-y)\Psi(y)dy. \tag{3.34}$$

Practically, this can be done by solving the initial value problem for the heat equation

$$\begin{aligned} v_t - \Delta v = 0 \quad \text{for} \quad & t \in [0,\eta] \\ & v(0) = \Psi \end{aligned} \tag{3.35}$$

on Ω with $\eta = \sigma$ and with suitably chosen boundary conditions, and putting

$$\hat{\Phi} \;=\; v(\eta). \tag{3.36}$$

Here, the smoothing time η can be considered as a regularization parameter: for $\eta = 0$ no regularization takes place, whereas with increasing η the updates become increasingly smoothed. See the general discussion on regularization schemes led in [44, 31].

3.6 Estimation of the dielectric properties of the tumor

In the shape reconstruction problem described in the previous section, we assumed that the values corresponding to the dielectric properties of the tumor and (an average value for) the surrounding tissue were given, even though they might not necessarily match the real values. With these assumptions, our algorithm finds the location and shape of a tumor that minimizes the cost functional (3.13) for the given dielectric parameters. If these parameters are incorrectly estimated, we expect that the shape will also be slightly incorrect in order to compensate for this error in the model. It is now natural to assume that, if there is any hope at all in reconstructing simultaneously the parameter values and the shape of the tumor from the given data, the final cost value will be the smaller the more we approach the correct values. With this assumption we will get a clearly defined global minimum of the cost functional for the simultaneous estimation of the correct shape and the corresponding correct parameter value. In the following, we want to investigate to what extend this statement is true, and whether it can be used for finding the dielectric properties of the tumor simultaneously with the shape.

To this end, we will start a shape reconstruction with a low relative permittivity equal to $\epsilon_i = 15$. We recall that ϵ_i is the only unknown dielectric property in this chapter, the other dielectric properties, κ_e, and σ_i, are assumed to be known. Upon convergence of this initial step, we find the tumor shape that minimizes the cost functional (3.13) for this parameter value, and we store the minimum value of the cost functional achieved in this search. We then successively increase ϵ_i by one unit $\delta\epsilon$ (in our numerical simulations we choose $\delta\epsilon = 1$) in each step, and we proceed in a similar way by computing the tumor shape that minimizes (3.13) for these new parameter values storing the corresponding minimum cost values. We stop the search when ϵ_i arrives at some predefined maximal value (which in our case is 65).

It is important to remark that in each of these reconstruction steps we start the search of the shape from the final result of the previous permittivity value. In this way, we have to perform only very few iterations of the shape reconstruction algorithm in order to achieve convergence. This is so because the optimal shape only changes very little when varying slightly the internal permittivity value.

At the end of this procedure, we obtain a curve corresponding to the achieved minimal values of the cost functional as a function of the permittivities ϵ_i, see the center right image of Fig. 3.1. We select the shape and

the dielectric properties of the tumor as the solution of the reconstruction problem which correspond to the global minimum of this curve.

We mention that, in principle, it is also possible to address the simultaneous estimation of the dielectric tumor parameters together with the shape by incorporating the tumor parameters into the set of unknowns of our evolution problem and looking for descent directions for them in each step of the algorithm. However, our experience is that this strategy does not work well for small tumors due to the existence of many local minima. Therefore, we have chosen to employ the above described alternative technique which is able to find all local and global minima for these additional parameters and the corresponding optimal shapes. In some sense, our alternative technique is a hybrid strategy that combines a gradient technique for the shape of the tumor and a sampling strategy for its dielectric properties.

3.7 Basic inversion algorithm

In the following we describe the numerical algorithm for detection and characterization of very small objects in the breast (tumors in their early stage of development) whose dielectric parameter values are significantly different from those of the fluctuations in the healthy tissue. The reconstruction algorithm consists of two stages:

- *First stage. Localization of the tumor.* Assuming a fixed permittivity value $\epsilon_i^{(0)} = 15$ inside the tumor, we find a series $S^{(q)}$ such that the cost (3.13) decreases with increasing $q = 0, 1, \ldots$ (see the top right image of Fig. 3.1). The value $\epsilon_i^{(0)}$ is chosen arbitrarily but slightly bigger than the value for the healthy tissue. In fact, we experimentally find that the location of the tumor is quite robust with respect to the choice of this value and gives about the same location if we choose a different one as long as this value is sufficiently different from the background value, ϵ_e, of the healthy tissue. It is important to note that we assume no initial tumor in this stage.

- *Second stage. Estimation of its shape and dielectric properties.* Here we find a series of pairs $(S^{(n)}, \epsilon_i^{(n)})$ such that the cost (3.13) decreases with increasing $n = 0, 1, \ldots$. We use as a good starting guess $(S^{(0)}, \epsilon_i^{(0)})$ the one provided by the *first stage*.

We now give more details of the algorithm. For visualization of the algorithm, we frequently refer to a typical test case displayed in Fig. 3.1. More

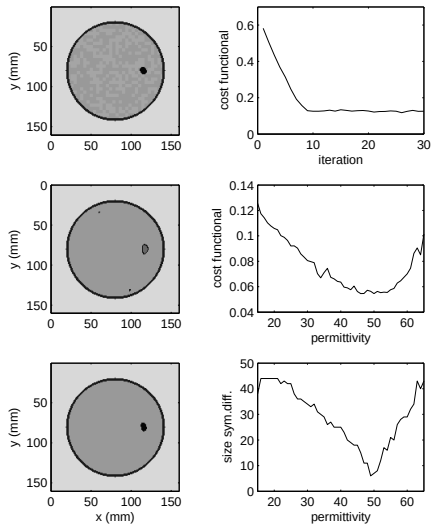

Figure 3.1: First numerical experiment: a tumor with the true permittivity value $\epsilon_i = 49$. Tumor size = 63 pixels. Background fluctuations = $\pm 10\%$. Noise level of data = $\pm 0.5\%$. Left column from top to bottom: reference permittivity profile (top), reconstructed profile at the end of the first stage of the algorithm (center), and reconstructed profile at the total minimum cost value of the second stage of the algorithm (bottom). Right column from top to bottom: evolution of the cost functional (3.13) during the first stage of the algorithm (top), the minimal cost value for each permittivity value during the second stage of the algorithm (center), and the size of the symmetric difference between the true tumor shape and the reconstructed tumor shape for each permittivity value during the second stage of the algorithm (bottom). The global minimum of the cost functional during this second stage of the algorithm is achieved at the permittivity value $\epsilon_i = 50$.

details to this test case are given, together with more numerical experiments, in section 3.8.

We start the first stage with a constant positive-valued level set function $\phi^{(0)} > 0$, which means that initially there is no shape present in the domain and no preference is given for any initial location of a tumor. Therefore, the first task of the algorithm will be to 'create' one or more objects at positions where the probability of a tumor is high. Then, we apply (3.32) with $f^{(1)}$ given by (3.31). As step-size criterion for the choice of $\delta t^{(1)}$ in (3.32) we look for the smallest choice of $\delta t^{(1)}$ which changes approximately (and preferably not more than) 5 pixel values in the domain (notice that this step-

size criterion does not require to run additional forward or adjoint problems and is therefore without additional computational cost.) This means that after applying the update (3.32) in the first step of the algorithm, a small shape (about 5 pixels in size) will be created at a location indicated by the sensitivity structure of the data. Then, we continue deforming this shape by calculating iteratively new forcing terms $f^{(n)}$, given by (3.31), and the corresponding new corrections of the level set function updating the latest best guess.

Each of these new steps uses the data of 5 frequencies (between 0.5 and 2 GHz) one after the other, which yields a so-called 'sweep' of our algorithm. In each update we choose a step-size such that about 5 pixel values change at this update (hitting exactly the target value of 5 pixels is sometimes difficult, in which cases we allow for fewer or more pixels to change in these updates). During this first stage of the inversion, 30 sweeps are applied in order to optimize the initial shape corresponding to the parameter value $\epsilon_i = 15$. At the end of this initial loop, we have found an optimized shape and a corresponding value of the least squares cost functional which are the final result of this initial reconstruction procedure. The result of the first stage reconstruction is displayed in the center left image of Fig. 3.1. The evolution of the cost functional is presented in the upper left image of this figure. Note, that we visually highlight the found shape of the tumor in these images by artificially surrounding it with a small band of darker color. Two 'ghosts' appear during this search.

Thereafter, we start the second stage of our algorithm whose aim is to optimize simultaneously the parameter value inside the tumor and its shape.

During this second stage of the algorithm, we continue in an efficient way by probing the corresponding minimal cost values achieved by the next higher permittivity values. Accordingly, we increase the value of ϵ_i by a fixed small step-size $\delta\epsilon$, and repeat the above search for the shape starting from the reconstructed shape corresponding to $\epsilon_i = 15$ but now assuming the value $\epsilon_i = 15 + \delta\epsilon$. Then we continue with the permittivity value $\epsilon_i = 15 + 2\delta\epsilon$ using as starting guess the reconstructed shape for $\epsilon_i = 15 + \delta\epsilon$. During this second stage we restrict the velocity $f(\mathbf{x}, t)$ to a narrowband in a small neighborhood of the tumor shape at each iteration. Hence we use a velocity given by (3.29). Doing so, we suppress in this second stage the ability of our level set updates to create new shapes far away from already existing ones. Since we already have found the location(s) of the possible tumor(s) at this stage of the algorithm, no new shapes are desired in this second stage. Instead, we can concentrate on refining the details of the already discovered shape(s). Moreover, in order to achieve more refined details in this second

stage, we restrict the line search criterion to a change of at most 2 pixels per update (again, in very few updates it might happen that it is difficult to achieve this step-size, in which cases a different number of pixels is allowed to change). We perform from 5 to 10 iterations for the set of 5 frequencies per permittivity value, and we store: (i) the minimum value of the cost functional (3.13), and (ii) the size of the 'symmetric difference' between the real and the reconstructed tumors (i.e., the added number of pixels which either belong to the correct tumor but not to the reconstructed one, or belong to the reconstructed tumor but not to the correct one). Once we have found these values for each probing permittivity, we search for the global minimum of the cost functional and interpret the corresponding permittivity value of the tumor and its corresponding shape as the reconstructed estimates of tumor characteristics. We emphasize that the size of the symmetric difference is monitored here only in order to investigate and validate the performance of our algorithm, but that it is not used in the reconstruction task itself (because it would require the knowledge of the correct tumor shape). The symmetric difference and the cost functional curves are displayed in Fig. 3.1 (center and bottom left images, respectively). The bottom left image corresponds to the final reconstruction result.

3.8 Numerical Experiments

In the numerical experiments presented here we investigate a 2D tomographic configuration as shown in the top left image of Fig. 3.1. In our experimental setup, a 12.0-cm-diameter breast, covered by a 3 mm-thick skin layer, is immersed in a matching fluid environment. 40 'transducers' are equidistantly distributed around the breast. The transducers illuminate it, one after the other, with microwaves of different frequencies. We use here 0.5, 0.8, 1.0, 1.5 and 2.0 GHz. The average relative permittivity and conductivity values for the breast tissue (background medium) are assumed to be $\epsilon_e = 9$ and $\sigma_e = 0.4$ S/m, respectively. To simulate the heterogeneity of the normal breast tissue, as measured by Chaudhary *et al.* [23] and Joines *et al.* [53], we add random variations of ± 10 %, distributed over 4×4 mm^2 squares, around these values. The skin layer has a permittivity value of $\epsilon_{skin} = 34$ and a conductivity value of $\sigma_{skin} = 1$ S/m. The surrounding 'matching' fluid medium is chosen to be slightly lossy with values $\epsilon_{liquid} = 2.5$ and $\sigma_{liquid} = 0.04$ S/m.

It is one of our goals in this chapter to investigate if our algorithm is able to specify the dielectric properties of a detected tumor together with its location and approximate size. For this purpose, we will apply our algorithm

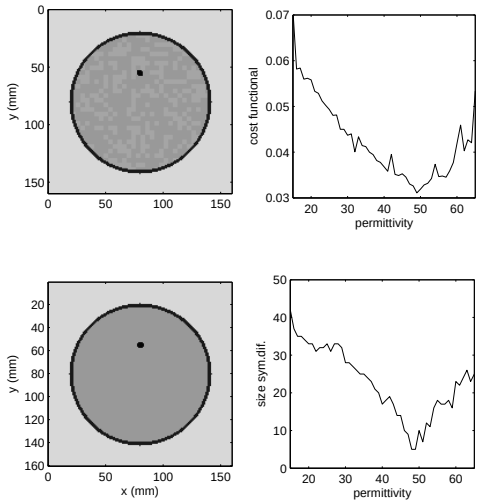

Figure 3.2: Experiment 2 (a): a very small tumor. Tumor size = 23 pixels. True permittivity value $\epsilon_i = 49$. The tumor is located deep in the breast. The objective of this experiment is to show the limitations of the algorithm for the simultaneous determination of size and parameter values of deeply located small tumors in relation to the level of the background fluctuations in the breast. Shown are reconstructions of the tumor assuming ± 5 percent of background tissue fluctuations. We display a block of four images, of each of which the top left shows the true permittivity profile, the bottom left shows the final reconstruction of stage 2 of the algorithm, the top right shows the minimum value of the cost functional for each permittivity value during the second stage of the algorithm, and the bottom right image shows the size of the corresponding symmetric difference between the true shape of the tumor and the reconstructed shape for each permittivity value.

to two different types of tumors, the first one having a constant permittivity value of $\epsilon_i = 36$ and the second one having the value $\epsilon_i = 49$. Both tumors have a conductivity value of $\sigma_i = 4$ S/m. We consider tumors with different sizes and positions in our numerical experiments. The combination of all reliably estimated characteristics for a given tumor (dielectric properties, size, shape, etc.) could help the physician in the task of characterizing a detected tumor as 'benign' or 'malignant'.

We solve (3.2) with a second order finite differences scheme and a perfectly matched layer (PML) for numerically terminating the computational domain. We use a mesh of 160×160 pixels. Each pixel is a square of $1 \times 1\ mm^2$. The numerically simulated 'true' data (corresponding to the assumed 'true'

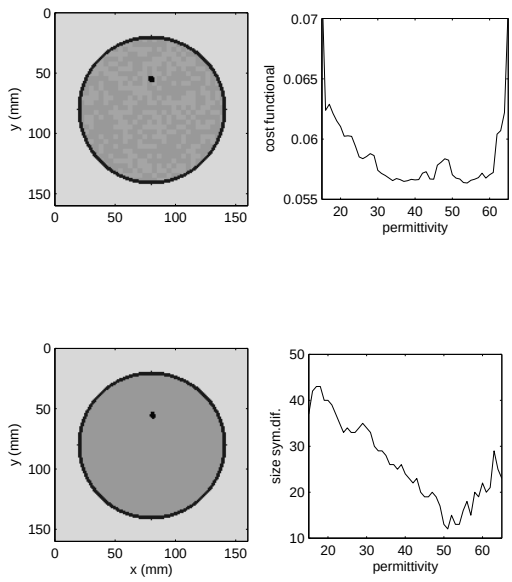

Figure 3.3: Experiment 2 (b): same as in Figure 3.2 but with ±10 of percent background tissue fluctuations.

breast) is perturbed by ±0.5% white Gaussian noise. In the following we show several results for breast imaging that illustrate the performance and robustness of our level-set based algorithm.

Figure 3.1 shows the results for a tumor that is located 2.0 cm beneath the surface. In this numerical setup, the tumor has a size of 63 pixels and its 'true' permittivity value is $\epsilon_i = 49$. The remaining values are as described previously. The top left image of this figure shows the 'true' permittivity profile. During the first stage, the algorithm tries to detect whether there is a tumor, and if so, to find its approximate location. For this, a low permittivity value $\epsilon_i = 15$ of the tumor is assumed (being actually quite far from the 'true' one $\epsilon_i = 49$). The center image of the left column of the figure shows the final reconstruction after 30 sweeps or iterations of this first stage of the algorithm. Each sweep uses each of the five frequencies exactly once. The top right image of the figure displays the evolution of the cost functional (3.13) during these 30 iterations. It is apparent that the cost functional (as well as the corresponding reconstructed shape) stabilizes after about 10 iterations at a relatively low cost value. A comparison of the reconstructed tumor with the correct one (displayed in the top left image of

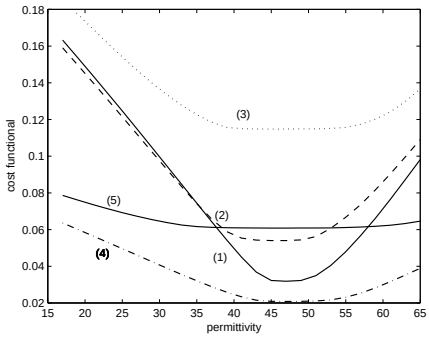

Experiment 3 (a):
cost assuming true tumor shape

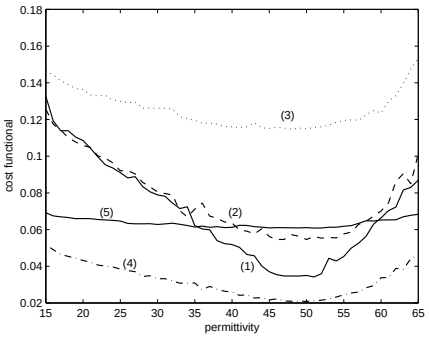

Experiment 3 (b):
cost for reconstructed tumor shape

Figure 3.4: The graphs in the left image (Experiment 3(a)) display the values of the cost functional for each permittivity value between $\epsilon_i = 15$ and $\epsilon_i = 65$ assuming that the correct shape of the true tumor is known. The graphs in the right image (experiment 3(b)) show the corresponding calculated cost values assuming instead the shapes which have been reconstructed by the algorithm for each permittivity value. The individual graphs of both images correspond to the following situations. Graph (1) (solid): ± 5 % background fluctuations, ± 0.5 % noise in the data, conductivity of surrounding skin $\sigma_s = 1$ S/m; graph (2) (dashed): same as in graph (1) but with ± 10 % background fluctuations; graph (3) (dotted): same as in graph (1) but with ± 2.5 % noise in the data; graph (4) (dash-dotted): same as in graph (1) but with $\sigma_s = 4$ S/m; graph (5) (solid): ± 10 % background fluctuations, ± 1.5 % noise in the data and $\sigma_s = 4$ S/m (the most 'difficult' case considered here). The 'flatter' a given curve is, the more difficult it will be for the algorithm to find the correct global minimum of the combined cost functional in the simultaneous search for shape and permittivity value.

the figure) demonstrates that (i) the tumor has been detected reliably (ii) its location has been estimated correctly and (iii) its size has been approximated quite well taking into account that the permittivity value assumed for the reconstructed tumor is incorrect and far away from the true one. Certainly, the reconstructed size can be improved, as it will be done during the second stage of the algorithm when searching also for the correct parameter value.

The second stage of the algorithm starts with the reconstruction of the first stage as initial guess. It minimizes the cost functional in only few iterations for a set of equidistant permittivity values between $\epsilon_i = 15$ and $\epsilon_i = 65$. For demonstration purposes we used here 10 iterations for each permittivity value, even though fewer would suffice. This minimized cost functional is

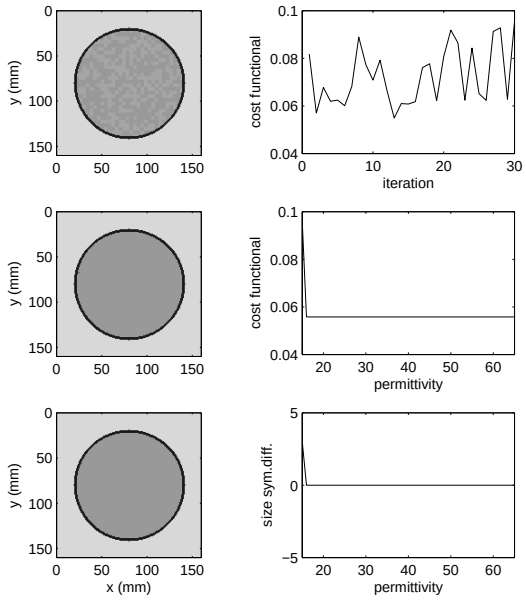

Figure 3.5: The same situation and arrangement of images as described in Fig. 3.1, but now without a tumor present in the 'true' breast. The objective of this experiment is to verify whether the algorithm can reliably distinguish between the situation with a tumor present in the 'true' breast and that one without a tumor present assuming random background fluctuations of about ± 10 percent in the parameters of the breast tissue and $\pm 0.5\%$ of noise in the data.

displayed in the center image of the right column of Fig. 3.1 as a function of the permittivity value. Once this second stage has been completed, we look for the global minimum of this curve and we take the corresponding permittivity value and its shape as the estimates of the tumor characteristics. We plot in the bottom left image of Fig. 3.1 our final estimated shape.

In order to monitor the quality of our reconstruction, and taking advantage of the fact that in our 'simulated' setup we actually 'know' the true tumor, we plot in the bottom right image of Fig. 3.1 the size of the symmetric difference (in number of pixels) between the reconstructed tumor and the true tumor shapes. We observe that both curves (displayed in the center and the bottom of the right column) show a clear minimum around the 'true' permittivity value $\epsilon_i = 49$. We conclude from this observation that our algorithm has been able not only to estimate the true permittivity value sufficiently well, but also to provide us with a good estimate of the corre-

sponding size of its shape: only very few (of the order of five) pixels are estimated incorrectly at this minimum value of the cost.

The second numerical experiment, whose results are displayed in Fig. 3.2, is designed in order to investigate the limitations of the second stage of our algorithm in the task of simultaneously estimating the parameter values of a tumor which has been detected and correctly located during the first stage of the algorithm. A small tumor of only 23 pixels and a permittivity value of $\epsilon_i = 49$ is located at 3.0 cm beneath the surface. Here the question arises which level of noise (in particular background fluctuations) can be tolerated in cases that the size of the tumor is very small and the tumor is located quite deep in the breast. We display in the top four images of the Fig. 3.2, subtitled as 'experiment 2 (a)', the reconstruction of our algorithm assuming that the background fluctuations are at the level of $\pm 5\%$ (as usual we also have added here $\pm 0.5\%$ of additive noise in the data). In the top left and bottom left images we plot the 'true' and the reconstructed permittivity profiles, respectively. In the top right image we plot the minimal cost value for each permittivity, and in the bottom right image we plot the size of the symmetric difference between true and reconstructed tumors. In Fig. 3.3, subtitled as 'experiment 2 (b)', show the reconstruction for the same situation but with stronger background fluctuation at the level of $\pm 10\%$. The arrangement of images in 'experiment 2 (b)' is the same as in 'experiment 2 (a)'. We observe that, for such a small and deeply located tumor, a reliable estimate of the true permittivity value can still be achieved by the algorithm for the case of $\pm 5\%$ background fluctuations, but that this is no longer possible if the background fluctuations reach the level of $\pm 10\%$. In the latter case, no clear minimum of the cost functional with respect to the permittivity value can be found during the second stage of the algorithm. Nevertheless, we want to emphasize that in both experiments the presence of the tumor is still clearly detected by our algorithm, along with a good estimate of its size.

A more systematic investigation of the limitations of the algorithm for the purpose of the simultaneous reconstruction of its size and permittivity value is displayed in Fig. 3.4. This study can also provide indications of the limitations of more general microwave imaging systems for this purpose. The general setup of this experiment is the same as that used in Fig. 3.1. However, three limiting factors of the algorithm are now modified: (i) the level of unknown background fluctuations of the parameters, (ii) the level of noise added to the data, and (iii) the conductivity value of the skin. Note that a high conductivity value of the skin has a 'shielding-effect' since the probing microwaves cannot easily penetrate into the breast.

As one part of this comparison we assume that the correct ('true') shape

of the tumor has been found and only the permittivity value needs to be reconstructed. In other words, we assume the prior knowledge of the location and exact shape of the tumor. In the upper image of Fig. 3.4 we display the least squares mismatch (3.13) between the 'true' (noisy) data and those data which have been calculated assuming probing permittivity values between $\epsilon_i = 15$ and $\epsilon_i = 65$. It is clear that a very flat curve of the least squares cost (3.13) with respect to the permittivity value will make it very difficult for the algorithm to estimate the correct permittivity value by a least squares search. In this case, the least squares cost does not depend significantly on the permittivity value. The exact parameter values corresponding to each of the curves from (1) to (5) are explained in detail in the caption of the figure. Interpreting these curves, we expect that the situations with a moderate level of noise in the data, represented by curves (1), (2) and (4), will allow us to reliably determine the permittivity value in addition to size and location of the tumor. These curves show sufficient variation of the least squares cost (3.13) with respect to the permittivity value (a 'gradient' or 'slope' being sufficiently different from zero). On the other hand, the situations (3) and (5), where the level of noise in the data has been increased, are expected to make it hard to recover these characteristics simultaneously with the shape. In these cases, the corresponding curves are almost flat (their slope or gradient almost being zero) in a large neighborhood of the correct permittivity value. From this figure, we conclude that the level of additive noise in the data is one of the more limiting factors in the simultaneous reconstruction of shape and permittivity value of the tumor, whereas the background fluctuations and the conductivity value of the skin are less restrictive.

As the other part of this comparison, we show in the bottom image of Fig. 3.4 the results when the correct shape of the tumor is not known. In other words, the corresponding curves achieved during this second part of the comparison take into account the simultaneous reconstruction of both the shape and the permittivity value of the tumor in order to minimize (3.13). These curves are those which correspond to the center right images of Fig. 3.1 (the second stage of our reconstruction algorithm) when assuming the modified values as used here. Comparing these curves with those of the upper image, we see that our algorithm reproduces their general tendency without knowing the correct shape. We observe, though, that the slopes of the curves obtained in the lower image are in general smaller (their gradients being closer to zero) than those of the upper image, and that the achieved minimized cost values are also slightly smaller. This behavior is due to the fact that an incorrectly assumed permittivity value during the reconstruction can partly be compensated by the algorithm by producing a slightly modified

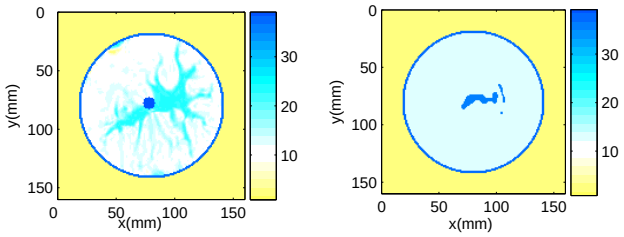

Figure 3.6: An example of a tomographic situation where the assumed binary model of this chapter represents an oversimplification. Here we know the average values of dielectric properties of breast, but the algorithm is not able to localize and characterize correctly the tumor. Left: reference profile, right: reconstruction with the basic algorithm.

shape. Nevertheless, this 'compensation effect' is not significant and does not change the location of the total minimum of these curves. Therefore, the simultaneous detection of size and permittivity value is indeed possible, as long as the curves shown in the upper image (which assume a perfectly reconstructed shape) have a sufficiently pronounced total minimum. Notice also that the cost value achieved by our algorithm when probing with the 'correct' permittivity value of $\epsilon_i = 49$ is almost identical to the one shown in the upper image, which indicates that our algorithm has been able to provide a very good approximation to the true shape of the tumor.

Figure 3.5 displays the results of our algorithm in a situation where no tumor is actually present in the breast. The arrangement of images in this figure is the same as in Fig. 3.1. The natural question that arises here is whether the typical but unknown background fluctuations, and the noise in the data, might give rise to 'ghosts' in the reconstructions which could be interpreted as a tumor (a 'false positive'). Recall that during the first stage of our algorithm we artificially enforce the creation of a tumor in the first step. Since the initial guess does not contain a tumor, there is no other way to start the search than to create a tumor. We observe, however, that during the first stage of the algorithm this created tumor does not grow, but instead is repeatedly removed. It might reappear at some later iteration, maybe at some other location, but also then it is removed by following iterations. We observe that none of these 'ghost objects' during the iterations of the first stage behaves stably, such that this first stage already indicates that there is in fact no tumor present. The evolution of the cost functional (3.13) during this stage of the algorithm shows highly erratic oscillations around the noise level 0.05 (see the top right image of Fig. 3.5), not showing any clear

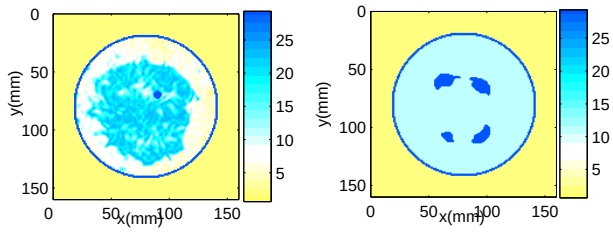

Figure 3.7: Another example of a tomographic situation where the simple binary model assumed in this chapter represents an oversimplification. Here we also do not know the average values of dielectric properties of the breast, and the algorithm is not able to localize and characterize correctly the tumor. Left: correct profile, right: reconstruction with the basic algorithm.

tendency of reduction for a given reconstruction. The final result of this first stage is, in this particular case, a small 'ghost' whose size consists of very few pixels (less than 5). As it can be seen, the first iterations of the second stage of the algorithm removes this 'ghost tumor' immediately, such that it is lost permanently. The now added 'narrowband' does not allow for the creation of a new tumor: a shape which has been removed completely during the second stage of the algorithm cannot be recovered. The final cost value remains constant at the value which represents the background fluctuations and the additional noise in the data. Moreover, the 'final shape' is empty, indicating correctly that there is no tumor present in the domain. Notice that it is already apparent at the end of the first stage of the algorithm that there is no tumor (since the cost is not clearly reduced), such that it is not really necessary to perform the second stage if there is no tumor present.

3.9 Limitations of the basic inversion algorithm

So far we have investigated the performance of our 'basic inversion algorithm' in the situations in which the numerically simulated data are generated with an 'almost binary' breast model (up to the assumed fluctuations), which is similar to the one assumed during the reconstruction. This was helpful in order to understand the fundamental behavior of level-set based reconstruction techniques in this application. Certainly, as we have shown in section 1.2, the structure of the real breast is typically more complex and does not

follow a strictly binary assumption. We present here two numerical experiments which demonstrate that a more refined breast model is required for the inversion in more realistic situations. Such a more refined model will be introduced and discussed then in the next chapter 4 of this thesis.

Figures 3.6 and 3.7 show two results of our basic inversion algorithm when applied to more realistic breast models. Here, the 'true' data are generated with an MRI-derived breast model for being as realistic as possible. These reference models are displayed in the left images of the corresponding figures. Roughly, the white and blue regions represent the fatty and fibroglandular tissue regions, with clearly visible variations of tissue parameters inside these regions and with a clearly visible interface between the regions of different tissue type. The added tumors are shown in a dark blue color. The results of our basic reconstructions, assuming a binary profile with only two possible values (one for the healthy tissue and another for the tumor, in addition to the known skin region), are shown in the right images of the figures. The results show that the big difference between the basic model and the true breast structure in these examples makes it impossible to reliably detect and characterize the hidden tumors. The basic algorithm cannot be applied in these situations. This motivates the development of a substantially generalized model as performed in the next chapter 4 of this thesis.

3.10 Summary

We have presented a novel shape based algorithm for the early detection and characterization of breast tumors from microwave data, which we call here the 'basic inversion algorithm'. It uses a binary model for the breast tissue and aims at investigating general aspects of level set based inversion from microwave data for breast screening. A level set technique has been employed in order to free the iterative algorithm from topological restrictions. The presented algorithm consists of two parts. The goal of the first part is to detect a tumor and to give a first estimate of its location and size. The second part starts with the result of the first part and aims at refining the information of location and size of the tumor while at the same time estimating its correct permittivity value. We have shown that the task of detecting and locating a hidden tumor by our algorithm is very stable and reliable. If there is no tumor present in the breast, the algorithm may create ghost objects during its first part due to the chosen line search criterion. However, these ghost objects are small and unstable and change location during the iteration, and, more importantly, the behavior of the cost functional during the first part

shows clearly that these objects cannot be interpreted as true tumors. Moreover, the 'ghost objects' disappear automatically during the first few steps of the second part of the algorithm due to the chosen narrowband strategy. Once a 'true' tumor has been detected and localized, the second part of the algorithm is able to reliably estimate its correct permittivity value simultaneously with its size and location. Only for very small tumors which are hidden deep in the breast, and in the presence of strong data noise, this characterization task of the tumor fails (we emphasize again that the detection and location task of the algorithm is not affected by these severe conditions). We have shown that in this case the least squares cost functional is nearly flat in a large neighborhood of the correct values (its 'slope' or 'gradient' is almost zero) and does not show a clear global minimum at the correct permittivity value. Different algorithms, aiming at simultaneously minimizing the least squares cost with respect to both the permittivity value and tumor shape by a strict gradient scheme, might trigger the stopping criterion at a premature and wrong permittivity value in these situations due to local minima. Finally, we have shown that the breast model used in the basic algorithm might be oversimplified when applied to real breast anatomies. This indicates the need for a more generalized and more complex reconstruction algorithm which is able to handle correctly and reliably real breast structures. In the next chapter 4 we will address this issue.

3.11 Publications and presentations

The following publications and presentations have resulted from the research described in this chapter.

Publications

- Natalia Irishina , Miguel Moscoso y Oliver Dorn , "Detection of small tumors in microwave medical imaging using level sets and MUSIC,", *Proc. PIERS, Cambridge*, pp. 43-47, 2006.

- Irishina Natalia, Oliver Dorn and Miguel Moscoso :'A level set evolution strategy in microwave imaging for early breast cancer detection', 'Computers and Mathematics with Applications', v.56, n3, 2008.

- Irishina Natalia, Oliver Dorn and Miguel Moscoso: 'Level-set techniques for microwave medical imaging', 6th International Congress on

Industrial and Applied Mathematics, 16-20 July, 2007, Zurich, Switzerland, WILEY-VCH Verlag GmbH, in: Proceedings in Applied Mathematics and Mechanics (PAMM), Volume 7, Issue 1, Date: December 2007, Pages: 1151601-1151602.

- N. Irishina, M. Moscoso and O. Dorn, 'Microwave tomography for breast cancer detection using level sets', Proc. 23rd International Review of Progress in Applied Computational Electromagnetics Conference ACES 2007, March 19-23, 2007, Verona, Italy, pp. 1955-1960 (2007).

- Irishina N, Moscoso M, Dorn O, 'Iterative microwave inversion for breast cancer detection using level sets', 14th European Conference for Mathematics in Industry, JUL 10-14, 2006 Univ Carlos III Madrid, Leganes, SPAIN, PROGRESS IN INDUSTRIAL MATHEMATICS AT ECMI 2006 Book Series: MATHEMATICS IN INDUSTRY Volume: 12 Pages: 592-596 Published: 2008

Presentations

- 2007, July 16-20 Level set techniques for microwave medical imaging (by N. Irishina, O. Dorn and M. Moscoso, presented by N. Irishina) 6th International Congress on Industrial and Applied Mathematics (ICIAM 07), Zurich, Switzerland.

- 2007 March 19-23 Microwave imaging for early breast cancer detection using a shape-based strategy (by N. Irishina, M. Moscoso and O. Dorn, presented by N. Irishina) The 23rd International Review of Progress in Applied Computational Electromagnetics ACES 2007, Verona, Italy

- Natalia Irishina , Miguel Moscoso y Oliver Dorn : Oral communication 'A shape based algorithm for microwave breast imaging', International Congress 'Mathematics for Industry',ECMI 2006 ', Madrid, Spain, July 10-14, 2006.

- 2006 March 26-29 New Level Set Strategies for Tumor Detection in Microwave Imaging (by N. Irishina, M. Moscoso, O. Dorn, presented by M. Moscoso) Progress in Electromagnetics Research Symposium (PIERS) 2006, Special session on Inverse Problems, (org. M. Cheney and O. Dorn), Cambridge, MA, USA

- 2005 June 26-30, Evolution strategies for shape reconstruction in microwave medical imaging, special session on 'Microwave imaging', Applied Inverse Problems Conference, Royal Agricultural College, Conference Center, England.
- Oliver Dorn, Natalia Irishina y Miguel Moscoso : Oral communication 'Microwave imaging with level sets', International Congress on 'Imaging', Lake Arrowhead, June, 2005.

Chapter 4

Structural inversion

4.1 Introduction

In this chapter, we consider breast models with more realistic internal structures. The breast models have three types of healthy tissue: fatty tissue, fibroglandular tissue, and the surrounding skin layer, as shown in the center and right images of Fig. 2.1 in section 2.5, and in Fig. 4.1 below. An important assumption throughout the chapter is that in all these breast models there are well defined interfaces between the different types of tissue. Furthermore, we will consider that the frequency dependence of the dielectric properties of the breast tissue is given by the Debye model

$$\epsilon_r^*(\mathbf{x};\omega) = \epsilon_\infty(\mathbf{x}) + \frac{\epsilon_s(\mathbf{x}) - \epsilon_\infty(\mathbf{x})}{1 - i\omega\tau} + i\frac{\sigma_s(\mathbf{x})}{\omega\epsilon_0}\ , \tag{4.1}$$

where ϵ_r^* is the complex relative permittivity, ϵ_∞ is the relative permittivity at infinite frequency, ϵ_s is the static relative permittivity, and σ_s is the static conductivity. In equation (4.1), τ is the relaxation time.

As in the previous chapter, to model wave propagation in a 2D heterogeneous breast Ω, illuminated by TM waves, we consider the scalar Helmholtz equation

$$\nabla^2 u(\mathbf{x}) \ + \ \kappa(\mathbf{x};\omega)u(\mathbf{x}) \ = -\, q(\mathbf{x}) \quad \text{in } \Omega\,, \tag{4.2}$$

supplemented by the Sommerfeld boundary condition. Here, $\kappa(\mathbf{x};\omega) = \omega^2\mu_0\epsilon_0\epsilon_r^*$ is the (squared) complex wavenumber, where $\epsilon_r^*(\mathbf{x};\omega)$ is the frequency-dependent complex relative permittivity given by (4.1).

In this chapter, we will show that the use of microwaves, combined with an adequate tomographic imaging strategy based on level set techniques, enables us to detect small tumors even in those cases where the strong heterogeneity

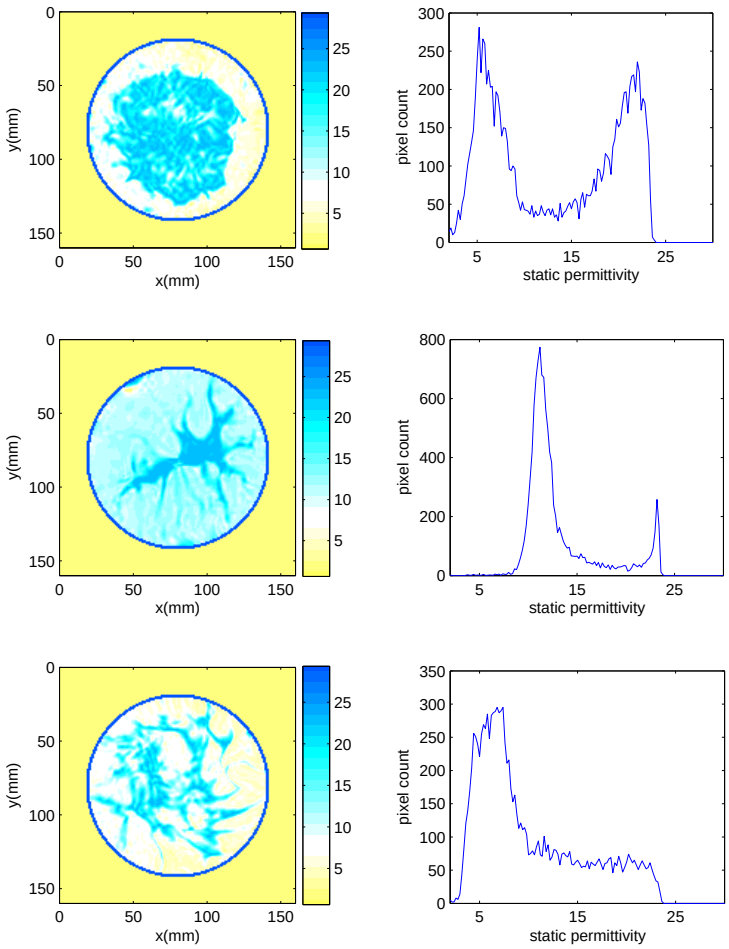

Figure 4.1: Synthetic MRI derived models [26]. Left column: the static permittivity maps; right column: the corresponding histograms of the static permittivity distribution.

	$\phi \leq 0$	$\phi > 0$
$\psi \leq 0$	tumor	fibre
$\psi > 0$	tumor	fat

Table 4.1: Representation of the fatty, fibroglandular, and tumor tissue by the level set functions ψ and ϕ.

of the healthy tissue substantially obscures the tumor response in the data. In addition, our generalized strategy provides information about the breast tissue composition that could be used in conjuction with other tomographic approaches. Our numerical experiments demostrate that the incorporation of a good estimate of the internal breast structure is necessary to detect the tumor in difficult situations, e.g. when the tumor is located deep inside the breast or when it is small.

Even though we will reconstruct also the fatty and fibroglandular regions, *our main objective* will still be to simultaneously (i) locate a tumor, (ii) estimate its size, and (iii) characterize its dielectric properties. In order to achieve these goals, we will introduce a four-stage reconstruction scheme where the complexity of the unknown (in our case, the static permittivity map $\epsilon_s(\mathbf{x})$) increases at each stage of the algorithm until arriving at the complete breast model. We will show that a significant improvement in the accuracy of the reconstruction process is obtained in this way.

The rest of the chapter is organized as follows. In section 4.2 we generalize the level set technique for representing the shapes of the different tissue types and we derive the evolution laws used for updating the level sets during the reconstruction process. In section 4.3 we present our four-stage reconstruction strategy. In section 4.4 we present the numerical experiments which confirm the robustness of our structural approach. Finally, section 4.5 summarizes the work presented in this chapter and gives some conclusions.

4.2 Structural inversion with level sets

In this section we present our shape reconstruction method using level sets.

A crucial feature of our model (and our algorithm) is the assumption that beneath the skin there are a well defined region containing fibroglandular tissue with dielectric properties which are distinct from those of the fatty tissue, and a tumor with dielectric properties distinct from those of both the

fatty and the fibroglandular tissues.

In the level set approach of shape reconstruction, the unknown shapes of the fibroglandular region and the tumor will be implicitly represented by two different 'level set functions' $\psi(\mathbf{x})$ and $\phi(\mathbf{x})$. We introduce two sufficiently smooth level set functions ψ and ϕ such that

$$\kappa(\mathbf{x}) \;=\; \begin{cases} \kappa_{_{tum}}(\mathbf{x}) & \text{where} \quad \phi(\mathbf{x}) \leq 0, \\ \kappa_{_{fib}}(\mathbf{x}) & \text{where} \quad \phi(\mathbf{x}) > 0 \text{ and } \psi(\mathbf{x}) \leq 0\ , \\ \kappa_{_{fat}}(\mathbf{x}) & \text{where} \quad \phi(\mathbf{x}) > 0 \text{ and } \psi(\mathbf{x}) > 0\ . \end{cases} \tag{4.3}$$

Here, the functions $\kappa_{_{fib}}$ and $\kappa_{_{fat}}$ denote the (squared) wavenumber inside the fibroglandular and fatty tissue regions, respectively, and $\kappa_{_{tum}}$ denotes the wavenumber inside the tumor. See also Table 1. In our approach, we will assume that the internal permittivity profiles of the fatty and fibroglandular regions are described by space-dependent functions, whereas those inside the tumor are assumed to be constant for all practical purposes due to the smallness of the tumor. We will indicate the dependence (4.3) of the parameter κ on the level set functions ϕ and ψ, by $\kappa = \kappa[\phi, \psi]$.

We recall that, acording to (4.1), κ depends on four parameters: τ, ϵ_s, ϵ_∞ and σ_s. However, as it was explained in section 2.4, τ is similar for different biological tissues in the microwave regime, so it will be considered as a known constant ($\tau = 7.0$ ps) in our model. Furthermore, motivated by published experimental values from the literature we will assume that in many realistic breast models the remaining three parameters are not completely independent. In fact, the dispersion parameters of the fibroglandular tissue in Table I of reference [104] approximately follow a linear functional relationship. This observation motivates us to simplify our breast model assuming that there exists some functional relation between these three parameters as it is expressed in (2.25)-(2.26). Consequently, in our models κ will only depend on one independent parameter (in our case, ϵ_s). The other two parameters are then given using (2.25)-(2.26).

Nevertheless, according to the above described model, we need to specify from the data five different unknowns instead of just one in the classical pixel-based approach: the two level set functions, the two space-dependent static permittivity profiles of the fatty and fibroglandular tissues, and the constant static permittivity value of the tumor.

In order to derive evolution laws for the individual unknowns, we write (4.3) in the alternative form

$$\kappa(\mathbf{x}) \;=\; \kappa_{_{tum}}(1 - H(\phi)) + H(\phi)\Big[\kappa_{_{fib}}(1 - H(\psi)) + \kappa_{_{fat}} H(\psi)\Big]\ , \tag{4.4}$$

where H denotes the Heaviside step function whose value is zero for negative arguments and one for positive arguments. In other words, we have now $\kappa = \kappa(\phi, \psi, \kappa_{fib}, \kappa_{fat})$, such that the least squares output cost functional can be written as

$$\mathcal{J}(\kappa(\phi, \psi, \kappa_{fib}, \kappa_{fat})) \;=\; \frac{1}{2}\|R(\kappa(\phi, \psi, \kappa_{fib}, \kappa_{fat}))\|^2 \;. \tag{4.5}$$

Notice that we have formally not included κ_{tum} in the list of unknowns since we will treat this important parameter with a special technique in our approach as explained further below.

Let us introduce an artificial evolution time t for the above specified unknowns of the inverse problem. Then, the goal is to find evolution laws

$$\frac{d\phi}{dt} \;=\; f(t) \quad , \qquad \frac{d\psi}{dt} \;=\; g(t) \tag{4.6}$$

$$\frac{d\kappa_{fib}}{dt} \;=\; h_{fib}(t) \quad , \qquad \frac{d\kappa_{fat}}{dt} \;=\; h_{fat}(t) \;, \tag{4.7}$$

such that the cost functional $\mathcal{J}$ (4.5) decreases with time. Consequently, the cost will also depend on the artificial evolution time, $\mathcal{J} = \mathcal{J}(t)$, such that we can formally calculate its time-derivative using the chain rule

$$\frac{d\mathcal{J}}{dt} \;=\; \frac{d\mathcal{J}}{d\kappa}\Big[\frac{\partial\kappa}{\partial\phi}\frac{d\phi}{dt} + \frac{\partial\kappa}{\partial\psi}\frac{d\psi}{dt} + \frac{\partial\kappa}{\partial\kappa_{fib}}\frac{d\kappa_{fib}}{dt} + \frac{\partial\kappa}{\partial\kappa_{fat}}\frac{d\kappa_{fat}}{dt}\Big] \tag{4.8}$$

$$= \mathtt{Re}\left\langle \mathcal{R}'[\kappa]^* R[\kappa]\,,\, \frac{\partial\kappa}{\partial\phi}f(t) + \frac{\partial\kappa}{\partial\psi}g(t) + \frac{\partial\kappa}{\partial\kappa_{fib}}h_{fib}(t) + \frac{\partial\kappa}{\partial\kappa_{fat}}h_{fat}(t)\right\rangle_P$$

where `Re` indicates to take the real part of the following complex quantity. As in the case of the simple breast model (see chapter 3), $R'[\kappa]^*$ is the adjoint of the linearized residual operator $R'[\kappa]$, and the expression $R'[\kappa]^* R[\kappa]$ represents the Fréchet derivative of $R[\kappa]$ with respect to κ. From (4.4) we derive by straightforward formal calculation that

$$\frac{\partial\kappa}{\partial\phi} \;=\; \delta(\phi)\Big[\kappa_{fib}(1 - H(\psi)) + \kappa_{fat}H(\psi) - \kappa_{tum}\Big], \tag{4.9}$$

$$\frac{\partial\kappa}{\partial\psi} \;=\; H(\phi)\delta(\psi)(\kappa_{fat} - \kappa_{fib}), \tag{4.10}$$

$$\frac{\partial\kappa}{\partial\kappa_{fib}} \;=\; H(\phi)(1 - H(\psi)), \tag{4.11}$$

$$\frac{\partial\kappa}{\partial\kappa_{fat}} \;=\; H(\phi)H(\psi). \tag{4.12}$$

Therefore, denoting $G_{\mathcal{J}}[\kappa] = R'[\kappa]^* R[\kappa]$, the following choices for the forcing functions point into descent directions of the least squares cost (4.5)

$$\begin{aligned} f(t) &= -C_{_\phi}(t)\mathtt{Re}\Big[G_{\mathcal{J}}[\kappa]\Big(\kappa_{_{fib}}(1-H(\psi)) + \\ &\qquad \kappa_{_{fat}}H(\psi) - \kappa_{_{tum}}\Big)\Big] \qquad (4.13) \\ g(t) &= -C_{_\psi}(t)\mathtt{Re}[G_{\mathcal{J}}[\kappa]H(\phi)(\kappa_{_{fat}} - \kappa_{_{fib}})] \qquad (4.14) \\ h_{_{fib}}(t) &= -C_{_{fib}}(t)\mathtt{Re}[G_{\mathcal{J}}[\kappa]]H(\phi)(1-H(\psi)) \qquad (4.15) \\ h_{_{fat}}(t) &= -C_{_{fat}}(t)\mathtt{Re}[G_{\mathcal{J}}[\kappa]]H(\phi)H(\psi), \qquad (4.16) \end{aligned}$$

where $C_{_\phi}$, $C_{_\psi}$, $C_{_{fib}}$ and $C_{_{fat}}$ are positive-valued (possibly evolution-time-dependent) constants which steer the speed of the evolution of each component individually. These constants can also be chosen zero, in which case the corresponding quantity does not evolve. Note that in the above formulas only the time-dependence of the functions $f(t)$, $g(t)$, $h_{_{fib}}(t)$ and $h_{_{fat}}(t)$ has been written explicitly (for simplicity), even though they are (for each given time) also functions of the space variable $\mathbf{x}$. Note, as well, that the forcing terms (4.13)-(4.16) have be extended to the whole domain Ω as we did previously in chapter 3.

Numerically discretizing the evolution laws (4.6) and (4.7) by a straightforward finite difference time-discretization with time-step $\delta t^{(n)} > 0$ in step n yields the iteration rules

$$\begin{aligned} \phi^{(n+1)} &= \phi^{(n)} + \delta t^{(n)} f^{(n)}, \qquad (4.17) \\ \psi^{(n+1)} &= \psi^{(n)} + \delta t^{(n)} g^{(n)}, \qquad (4.18) \\ \kappa_{_{fib}}^{(n+1)} &= \kappa_{_{fib}}^{(n)} + \delta t^{(n)} h_{_{fib}}^{(n)}, \qquad (4.19) \\ \kappa_{_{fat}}^{(n+1)} &= \kappa_{_{fat}}^{(n)} + \delta t^{(n)} h_{_{fat}}^{(n)}, \qquad (4.20) \end{aligned}$$

with suitable initializations for the four quantities at the (discretized) evolution time $t^{(0)}$.

4.3 Four-stage reconstruction strategy

In this section we describe the four stage reconstruction algorithm for the detection and characterization of very small tumors. In order to achieve this goal, the structural reconstruction of fibroglandular and fatty regions and their characterizations will be essential. The main idea of our reconstruction strategy can be summarized as follows:

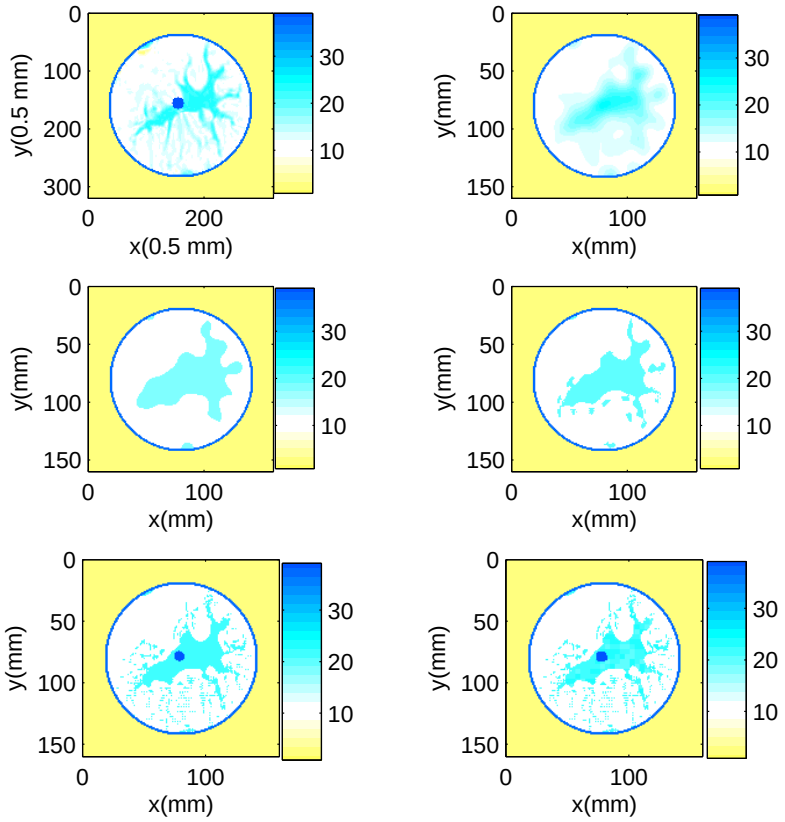

Figure 4.2: An example for our reconstruction algorithm using one of the numerical models from figure 4.1. Top row: reference static permittivity profile and the reconstructed static permittivity map at the end of stage I (right). Center row: reconstructions at the beginning (left) and at the end of stage II (right). Bottom row: reconstruction at the end of stage III (left) and the final reconstruction corresponding to the minimum value of the cost functional during the IV stage (right).

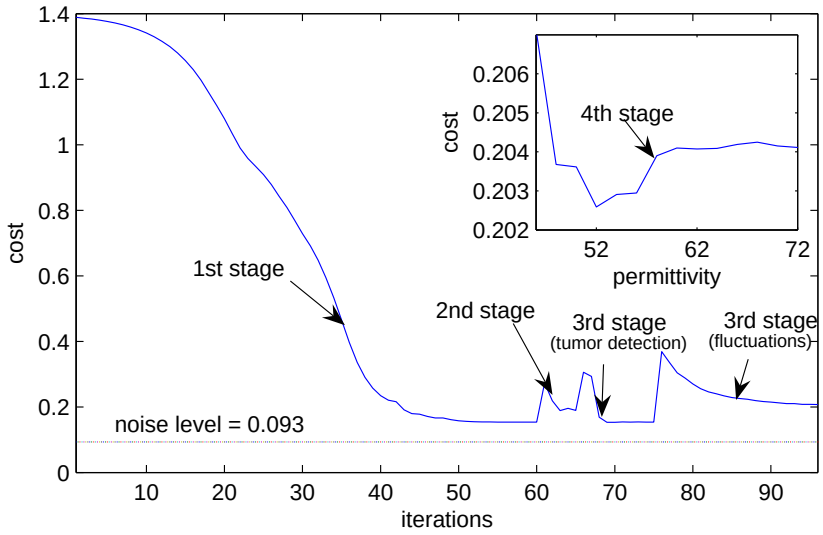

Figure 4.3: Evolution of the cost during the reconstruction process. The inset corresponds to the minimal values found for each ϵ_{tum}^s during the search in the fourth stage of the algorithm.

We define four stages of increasing complexity. At each new stage, the reconstructed breast model incorporates more features of the complete breast, so it is more refined than the reconstruction of the previous stages. In particular, we use at each stage of the algorithm the result of the preceeding stages for defining a good starting guess.

This strategy of using in each stage submodels with increasing complexity, until arriving at the complete breast model in the last stage, allows us to avoid certain local minima in the underlying optimization problem. Furthermore, it helps us in arriving at a stable and reliable reconstruction process.

A quick overview of the four stages is given next. A more detailed discussion of each stage follows further below. During this quick overview we illustrate basic stages of the algorithm referring to Fig. 4.2 which shows the corresponding results for a test case. The setup of this test case is described in more details also further below.

- *First stage. Pixel-based reconstruction.* At the beginnig of the reconstruction we do not assume neither an initial shape of the fibroglandular region nor a tumor. We start the inversion by a classical pixel-based iterative reconstruction to achieve successive improvements of an initial

guess, which in our case is a homogeneous profile with arbitrary dielectric properties. This amounts to setting the level set functions $\phi = 1$ and $\psi = 1$ everywhere within the domain, and $C_\phi = C_\psi = C_{fib} = 0$ and $C_{fat} > 0$ in the general model presented in section 4.2. The stage ends when the cost functional is minimized (see Fig. 4.3). A result of such a reconstruction at the end of this stage can be seen, for example, in the top right image of Fig. 4.2.

- *Second stage. Shape-based reconstruction of the fibroglandular region.* The goal of this second stage is to find a first estimate of the fibroglandular region assuming that there is no tumor. We set $\phi = 1$, and $C_\phi = 0$, $C_\psi > 0$, $C_{fib} > 0$ and $C_{fat} > 0$ in the general model presented in section 4.2. The estimate of the fibroglandular region does not need to be exact and it will be refined later. From a starting guess $(\psi^{(0)}, \kappa_{fib}^{(0)}, \kappa_{fat}^{(0)})$ extracted from the result of the first stage (see the center left image in Fig. 4.2), as will be explained below, we find a series of $(\psi^{(n)}, \kappa_{fib}^{(n)}, \kappa_{fat}^{(n)})$, $n = 0, 1, \ldots, N_2$, such that the cost functional $\mathcal{J}^{(n)}$ decreases. The second stage ends when $\mathcal{J}^{(n)}$ does not decrease anymore (see Fig. 4.3). An example of a reconstruction at the end of the second stage can be seen in the center right image of Fig. 4.2.

- *Third stage. Location and shape of the tumor.* Once we have obtained a first estimate of the shapes and dielectric properties of the fibroglandular and fatty tissue, we proceed in a similar way to detect the possible tumor and to approximate its location and shape. We assume no initial tumor shape in this stage. Initially, we set $C_\phi > 0$, $C_\psi > 0$, and $C_{fib} = C_{fat} = 0$ in the general model derived in section 4.2. We use as a starting guess, $(\phi^{(0)}, \psi^{(0)}, \kappa_{fib}^{(0)}, \kappa_{fat}^{(0)})$, the result $(\phi = 1, \psi^{(N_2)}, \kappa_{fib}^{(N_2)}, \kappa_{fat}^{(N_2)})$ given by the second stage. Assuming a fixed static permittivity value $\epsilon_{tum}^{(0)} = 35$ inside the tumor, we find a series $(\phi^{(n)}, \psi^{(n)}, \kappa_{fib}^{(n)}, \kappa_{fat}^{(n)})$ which minimizes the cost functional $\mathcal{J}^{(n)}$, $n = 0, 1, \ldots, N_3$. The value $\epsilon_{tum}^{(0)}$ is chosen arbitrarily but slightly bigger than the values for the healthy tissue. We stop the iteration process when the cost functional does not decrease anymore. An example of a reconstruction at the end of this stage can be seen in the bottom left image of Fig. 4.2. Observe that the location and size of the tumor have been approximated very well although the assumed value of ϵ_{tum} is not correct (the correct value in this example is 53).

- *Fourth stage. Characterization of the tumor.* In this last stage of the

algorithm we address the probably most difficult task: to specify the correct dielectric properties and the shape of the detected tumor. We assume here that the shapes and internal properties of the fatty and fibroglandular regions have already been estimated well, so we keep $(\psi, \kappa_{fib}, \kappa_{fat})$ fixed. Therefore, $C_{\psi} = C_{fib} = C_{fat} = 0$ and $C_{\phi} > 0$. To find the optimal values $(\phi^{opt}, \kappa_{tum}^{opt})$ that fit the data, corresponding to the global minimum of the cost functional, we use a hybrid strategy combining a gradient technique for the shape of the tumor and a sampling strategy for its dielectric properties. See the inset Fig. 4.3 that shows the minimal cost values versus the static permittivity. We pick the reconstruction corresponding to the global minimum of this curve as our final reconstruction (shown in the bottom right image of Fig. 4.2).

It is interesting to compare the quality of our reconstruction in this test case with the 'classical' pixel-based reconstruction (certainly using our own implementation) presented in the top right image. The level set strategy provides a much clearer identification of the tumor key characteristics and a more accurate estimate of the complex structure of the breast interior than our pixel-based scheme. This certainly makes sense since the level set strategy takes into account important structural information regarding typical breast tissue, which cannot easily be incorporated in a classical pixel-based scheme.

In the following we give more details of the algorithm.

We start the inversion process by a classical pixel-based iterative approach. We assume to know the dielectrical properties and the width of the skin layer, as well as the properties of the surrounding medium. The reconstruction at the end of this first stage of the algorithm is shown in the upper right image of Fig. 4.2. Observe that at the end of this stage it is difficult or impossible to accurately estimate key characteristics of a tumor like its position and size, or even to reliably assess the presence of the tumor.

We mention here that pixel-based schemes might be optimized to capture microwave imaging applications, yielding possibly slightly better results than those of our straightforward pixel-based implementation for this first stage. Nevertheless, the 'oversmoothing effect' of regularized pixel-based schemes will still apply which makes it difficult (in most cases impossible) to extract the important information directly from the results of these schemes for very small tumors embedded in heterogenous breast tissue.

The goal of the second stage is to estimate the shape of the fibroglandular region assuming that there is no tumor present. To estimate the fibroglandular region we first replace the reconstructed pixel pattern achieved during the previous stage by a bimodal distribution: we only consider in this stage healthy tissue (fat and fibroglandular) ignoring the possible presence of a hidden tumor. To this end, we compute the mean value of the reconstructed permittivity distribution and introduce a level set function $\psi(\mathbf{x})$ which is positive at the locations of lower permittivity value (fat) and negative at the locations of higher permittivity value (fibre). The assigned values to κ_{fat} and κ_{fib} are the average values in each of the corresponding fatty or fibroglandular regions. The result is a bimodal distribution defined by the introduced level set function $\psi(\mathbf{x})$. The center left image of Fig. 4.2 is an example of such an initial guess.

We update the level set function $\psi(\mathbf{x})$ using the corresponding descent direction of the cost functional (see section 4.2 for details). In each region, defined by $\psi(\mathbf{x})$ and denoted by $D_{fat,fib}$, we update the (average) values $\kappa_{fat,fib}$ calculating the following corrections

$$\delta\kappa_{fat,fib} = \int_{D_{fat,fib}} G_{\mathcal{J}}[\kappa](\mathbf{x})\, d\mathbf{x} \tag{4.21}$$

from the data. The result of the second stage of the algorithm is shown in the center right image of figure 4.2.

Once we have obtained a first estimate of the shape of the fibroglandular tissue, we proceed in a similar way to detect and find the location and shape of a possible tumor during the third stage of the algorithm. Notice that introducing a tumor has an effect also on the optimality property of the fibroglandular tissue region as found in the second stage, such that we also keep evolving this region during this new stage. Now, the distribution of $\kappa(\mathbf{x})$ will take four values assumed to be fixed: three values indicating healthy tissue (skin, fat, and fibroglandular), and a fourth value indicating the tumorous tissue. The initial guesses for the first three of these values are taken from the previous stages, whereas the fourth value (the permittivity of the tumor) will be chosen arbitrarily but slightly bigger than the values for fat and fibroglandular tissue.

In the third stage, we will have to evolve two level set functions simultaneously: ϕ which models the tumor, and ψ which models the fibroglandular region. During the first steps we choose $C_{_\psi} > 0$, $C_{_\phi} > 0$, and $C_{_{fib}} = C_{_{fat}} = 0$ in the general model case derived in the previous chapter. Upon convergence we locate and estimate the shape of the tumor together with the corresponding optimal area of the fibroglandular tissue.

Note that, so far, we have not yet taken into account the internal structure of fatty and fibroglandular tissue. Actually, this task can be accomplished easily with our general formulation. If it is desired, during the evolution, we can not only correct in each step the two level set functions, but we can also extract from the data pixel-by-pixel updates for the internal profiles in the fatty and fibroglandular regions. A nice feature of our adjoint based shape reconstruction scheme using level sets is that there is no extra cost involved for finding updates for those tissue variations in each step of the algorithm. All what is needed is the knowledge of the pixel-based Frechét derivative $R'[\kappa]^* R[\kappa]$ which anyway is part of the calculation of the updates for our level set functions. Accordingly, at the end of this third stage we will choose $C_{_\psi} > 0$, $C_{_\phi} > 0$, $C_{_{fib}} > 0$ and $C_{_{fat}} > 0$ in the general model derived in the previous subsection. In the numerical examples in which we have chosen to approximate the effect of these unknown internal profiles on the data, we have initialized the search by adding arbitrary fluctuations of a typical type into the fatty and fibroglandular regions (which certainly will not agree with the true profile). The result of the third stage of our algorithm is presented in the bottom left image of Fig. 4.2.

In the last stage of the algorithm we address the probably most difficult task, namely specifying the correct dielectric properties and the shape of the detected tumor. In the previous stages we have used an arbitrary value for the static permittivity value for the tumor which satisfies certain criteria but which is unlikely to be the correct value. It is clear that the correctly estimated value will depend on the details of the other reconstructed features of the breast, most notably on the estimated size of the tumor. Since we have already estimated during the first three stages in a very reliable way those features of the breast which correspond to the fatty tissue and the fibroglandular tissue, we will concentrate in this fourth step on the correct estimation of the tumor and its correct dielectric properties. The shape of the fibroglandular tissue, as well as the internal properties of the fatty and fibroglandular regions, are fixed in this stage. Therefore, $C_{_\psi} = C_{_{fib}} = C_{_{fat}} = 0$ and $C_{_\phi} > 0$.

We will consider two different strategies for finding the correct values inside the tumor(s). The first and most straightforward strategy consists in applying a gradient-based strategy which updates in each step of the algorithm (with no extra cost) the internal tumor profiles, now considered as space dependent functions, in the same way as we have updated in stage three the internal profiles of the fatty and fibroglandular regions. This strategy is applied in the numerical experiment shown in figure 4.8 from subsection 4.4.1, where two tumors with different internal static permittivity values need to

be characterized simultaneously from the same data set.

However, this joint search of the dielectric tumor properties and the tumor shape (and size) is an optimization problem which often suffers from many local minima and extremely slow convergence when using such a traditional gradient based search strategy. Moreover, it is very difficult to find good criteria for the right balance in the step sizes for the joint updates of the shape and the dielectric properties of the tumor when using this strategy.

We propose an alternative technique (in a certain sense a hybrid strategy combining a gradient technique for the shape of the tumor and a sampling strategy for its dielectric properties) for finding the global minimizer of our cost functional in a stable and efficient way from the given data, which was already described in the previous chapter devoted to the simplified model. We will use this alternative technique in those cases where the result of the third stage indicates that there is only one tumor present in the breast. We remind the reader that in this alternative technique we assume that the static permittivity inside the tumor is a constant value which needs to be estimated (together with the tumor shape) from the data. We choose as final reconstruction the shape and the permittivity value which correspond to the global minimum of the curve which maps minimal cost values (from the shape reconstruction for each of the probed internal static permittivity values) against the corresponding internal static permittivity values.

4.4 Numerical experiments

In this section we have divided the numerical experiments into three groups according to their difficulty. There are three sets of experiments in which we gradually reduce the amount of correct 'prior' information available for estimating the breast tissue properties, and we decrease the signal-to-noise ratio (SNR)[1]. They also correspond to the chronological order in which they have been obtained in our research.

- **Set of experiments I**. In subsection 4.4.1 we assume that the average values of the dielectric properties of the healthy tissue (fat, fibre

[1]Signal-to-noise ratio is an electrical engineering concept, defined as the ratio of a signal power to the noise power corrupting the signal:

$$SNR(dB) = 10\, log_{10} \frac{\sum_{i=0}^{N_{det}} A_i^2}{\sum_{i=0}^{N_{det}} (D_i - A_i)^2}, \tag{4.22}$$

A_i is the data in the detector i for the 'real' image, D_i is the data with noise, N_{det} is the number of detectors. A lower SNR indicates a higher degree of noise in the data

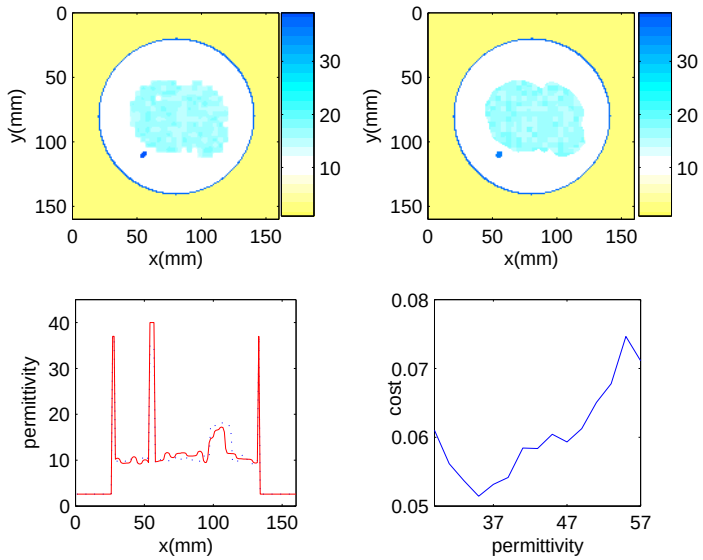

Figure 4.4: Top left image: reference permittivity profile illustrated by the dispersion Debye parameter ϵ_s ($\pm 15\%$ of fluctuations). Top right: reconstructed permittivity profile of ϵ_s. Bottom left: cross sections along the tumor location of the reference ϵ_s (solid line) and the reconstructed ϵ_s (dashed line). Bottom right: minimal cost value for each value of the dispersion Debye parameter ϵ_s during the fourth stage of the algorithm.

and skin) are known. The width of the skin layer is assumed to be known as well. Accordingly, we will choose $C_{fib} = C_{fat} = 0$ during the reconstructions. The 'true' synthetic data in these experiments are generated numerically from the 'true' breast model using the same 160x160 mm^2 grid as used during the reconstructions. We add $\pm 0.5\%$ of Gaussian noise to the obtained data, so the resulting SNR is 50 dB. The breast model we consider in these experiments corresponds to the model shown in the center image of Fig. 2.1. It has a well differentiated fibroglandular region with average static permittivity value $\epsilon_s = 22.6$ (the corresponding values of ϵ_∞ and σ_s are 6.1 and 0.3 S/m, respectively), and fatty tissue around the fibroglandular region with average static permittivity $\epsilon_s = 10$ ($\epsilon_\infty = 6,9$ and $\sigma_s = 0.15$ S/m). The average values chosen for both the fatty and the fibroglandular tissue are taken from references [8, 104, 26, 81]. To model the anatomical heterogeneities of the biological tissue we add random variations of $\pm 15\%$ in form of fluctuations, distributed over 4×4 mm^2 squares, around these

values in both tissue types. This presumably covers realistic fluctuations in real human breast [23, 99, 53]. The dilectric parameters of the skin are: $\epsilon_s = 34$, $\epsilon_\infty = 4$ and $\sigma_s = 1.1$ S/m.

- **Set of experiments II**. In subsection 4.4.2 we do not assume prior knowledge of the average dielectric properties of the fatty and fibroglandular tissue. However, the properties of the skin layer (dielectric properties and width) are still assumed to be known. Now the 'true' synthetic data are obtained using a finer grid (320x320 mm^2) than the 160x160 mm^2 grid used during the inversion process, so the 'effective' SNR (which incorporates this difference in the grid sizes as 'additional noise') decreases significantly. The resulting effective SNR is 26 dB. In this set of experiments we used MRI-derived breast models that offer a more complex internal structure and a more realistic heterogeneity of the tissue. These models are shown in Fig. 4.1 together with their histograms that display the range and distributions of the static permittivities. The average values of the fibroglandular regions are: $\epsilon_s^{fiber} = 23,19$ (top), $\epsilon_s^{fiber} = 24,1$ (middle), and $\epsilon_s^{fiber} = 19,33$ (bottom). The average values of the fat regions are: $\epsilon_s^{fat} = 8,20$ (top), $\epsilon_s^{fat} = 11,65$ (middle), and $\epsilon_s^{fat} = 9,20$ (bottom). The dielectric parameters of skin are: $\epsilon_s = 37$, $\epsilon_\infty = 4$, and $\sigma_s = 1.1$ S/m.

- **Set of experiments III**. In subsection 4.4.3 we further increase the difficulty of the reconstructions by assuming no 'prior' knowledge about the properties of any tissue type contained in the breast. In particular, the properties of the skin layer are also unknown. As in **Set of experiments II**, we use MRI-derived breast models and different grids for generating the synthetic data and for the reconstruction task.

In all the cases, we introduce a small diameter tumor at different depths below the skin to generate the sythetic data. The considered tumors have different sizes (the diameters range from 3 to 8 mm) and static permittivities ϵ_s (which may indicate the grade of malignancy of the tumor) which both need to be reconstructed from the data. As typical values for the remaining electromagnetic parameters inside the tumors we apply $\epsilon_\infty = 3.9$ and $\sigma_s = 0.7$ S/m. Since the sizes of the tumors, sought in our numerical simulations, are at the resolution limit of typical microwave imaging strategies, we will neglect here their possible internal structure and assume that their internal dielectric parameters are spatially independent when creating simulated data. The 12.0-cm-diameter breast, immersed in a slightly lossy environment with dielectric parameters $\epsilon_{liquid} = 2.5$ and $\sigma_{liquid} = 0.04$ S/m, is surrounded by

40 equidistantly distributed electromagnetic 'transducers' that illuminate it, one after the other, with microwaves of different frequencies.

4.4.1 Set of experiments I

The breast model of the numerical example shown in Fig. 4.4 is composed of a compact region of fibroglandular tissue with $\epsilon_s^{fib} = 16.3$, and a well differentiated surrounding layer of fatty tissue with $\epsilon_s^{fat} = 10$. The shape of the fibroglandular region and the small heterogeneities of the breast tissue are created artificially. This model is not derived from an MRI image. A small tumor of $\epsilon_s^{fib} = 40$ is inserted in the fatty tissue not very far from the external boundary of the breast. Therefore, this is an easy example to study the performance of the algorithm. Besides, we assume a complete and correct knowledge of the properties of the skin layer. This figure shows that (i) the tumor has been detected reliably, (ii) its location has been estimated correctly and (iii) its size and dielectric parameters have been approximated very well. In addition, the reconstruction of the shape of the fibroglandular region was successful.

An assumption used in the previous example was that the parameter values of the skin layer were known. In figure 4.5, we examine the robustness of our algorithm when these parameters are chosen incorrectly. For this numerical experiment, we compute the 'true' data using a 2.0 mm-thick skin layer with ϵ_s, ϵ_∞ and σ_s, equal to 37, 4.0 and 1.1 S/m, respectively. However, for the reconstruction we assumed a 1.5 mm-thick skin layer with ϵ_s, ϵ_∞ and σ_s, equal to 39, 4.1 and 1.0 S/m, respectively. Hence, the assumed parameters are not correct and represent a modeling error. In this experiment, the tumor is located closer to the center of the 2D coronal plane of the breast. Its static permittivity value is $\epsilon_s^{tum} = 45$. Also here the figure shows that our algorithm is able to identify the tumor and provides information on its size and dielectric properties (the estimated static permittivity is 42).

In figure 4.6, we investigate the sensitivity of our algorithm to the number of antennas. In this numerical example we use fewer antennas (20 instead of 40), and the breast model has a higher average static permittivity value in the fibroglandular region of $\epsilon_s = 22.6$. This is a typical static permittivity value of the fibroglandular tissue in denser breast [104], [81]. The static permittivity of the tumor is now $\epsilon_s^{tum} = 50$. As it can be seen in figure 4.6, the tumor is detected and well located. However, the static permittivity value inside the tumor is in this case underestimated (here 40). Other numerical experiments with 40 antennas (and the same breast model parameters), not shown here, provided a better estimate of the tumor permittivity value (47).

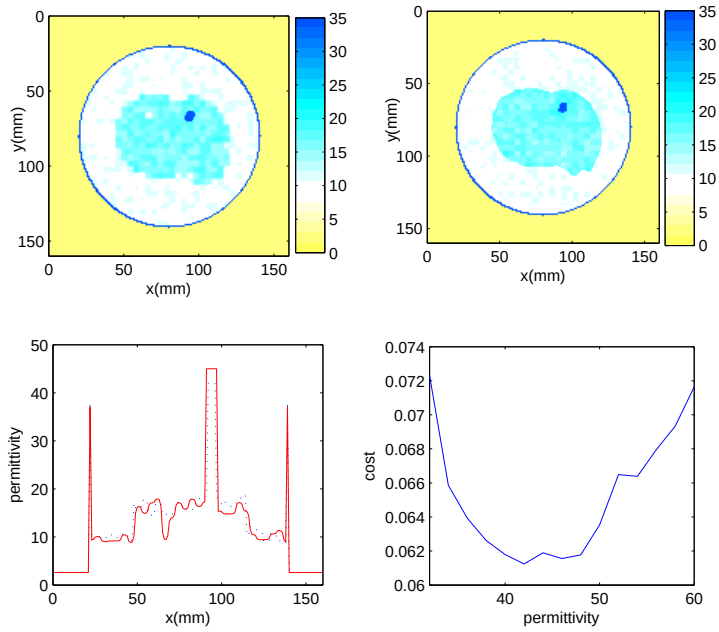

Figure 4.5: The probe of the robustness of the detection of a hidden tumor of size 6×8 mm^2 from slightly incorrect assumed skin values during the reconstruction. Top left image: reference permittivity profile illustrated by the dispersion Debye parameter ϵ_s. Top right: reconstructed permittivity profile of ϵ_s. Bottom left: cross sections along the tumor location of the reference ϵ_s (solid line) and the reconstructed ϵ_s (dashed line). Bottom right: minimal cost value for each value of the dispersion Debye parameter ϵ_s during the fourth stage of the algorithm.

Next, we consider in the experiment displayed in figure 4.7 a situation where no tumor is actually present in a breast with the same set of dielectric parameters as in figure 4.5. The natural question that arises here is whether the typical but unknown background fluctuations, and the noise in the data, might give rise to 'ghosts' in the reconstructions which could be interpreted as a tumor (a 'false positive'). Recall that at the third stage of our algorithm we artificially enforce the creation of a tumor in the first step which evolves during the succeeding updates, see the small spot at the lower right border of the fibroglandular region in the top right image of the figure. We observe, however, that the final reconstruction at the bottom left of figure 4.7 indicates that this 'tumor candidate' actually has an estimated static permittivity value of $\epsilon_s^{tum} = 19$ which is very close to the fibroglandular tissue value of

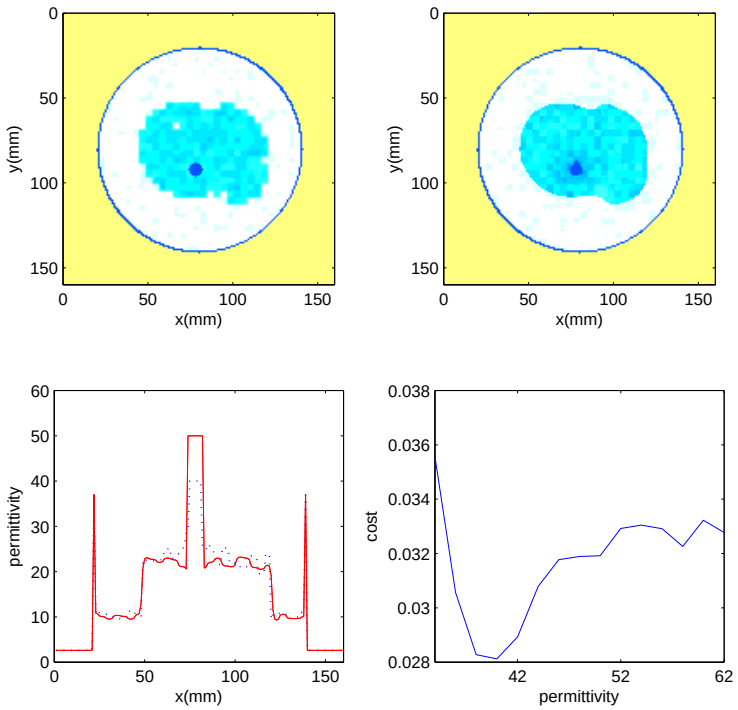

Figure 4.6: The dependence of the reconstruction on the number of antennas. Fewer antennas (20 instead of 40) are used here for finding a tumor located within a denser fibroglandular tissue ($\epsilon_s^{tum} = 50$, $\epsilon_s^{fib} = 22.6$, $\epsilon_s^{fat} = 10$, and $\pm 15\%$ fluctuations). The results are displayed in a panel of four figures as figure 4.5. The color map corresponds to the colorbar shown in figure 4.5.

this experiment (16.3) and far from a typical tumor value. Therefore, the algorithm correctly indicates that no tumor is present in the breast.

Now we investigate a situation where more than one tumor are present with different internal static permittivity values. We will apply a gradient-based reconstruction technique during stage IV of the algorithm in those cases where the result of stage III indicates that there are more than one tumor in the breast. This allows us to reconstruct individual static permittivity values for these two tumors. In more details, the set of parameters of the breast model used in the experiment of figure 4.8 is the same as in figure 4.5. There are two tumors present in the breast, the first one being located 4 cm beneath the skin ($\epsilon_s^{tum} = 35$), and the second one being located 4.2 cm beneath the skin ($\epsilon_s^{tum} = 55$). We observe that both tumors are well located

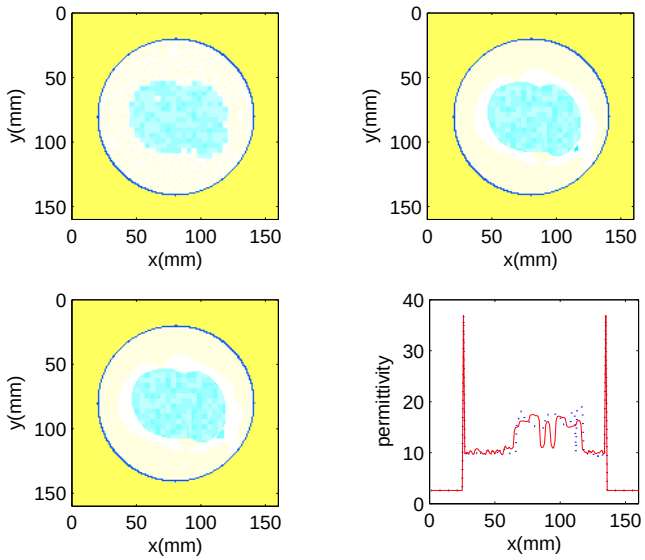

Figure 4.7: The behavior of the algorithm if no tumor is present in the breast. The breast has values $\epsilon_s^{fib} = 16.3$, $\epsilon_s^{fat} = 10$, and $\pm 15\%$ fluctuations. The figure shows the reference permittivity profile (top left), the reconstructed profile at the end of the third stage of the algorithm (top right), the reconstructed profile at the end of the algorithm (bottom left), and the minimal values of the cost functional vs. ϵ_s^{tum} (bottom right). The color map corresponds to the colorbar shown in figure 4.5.

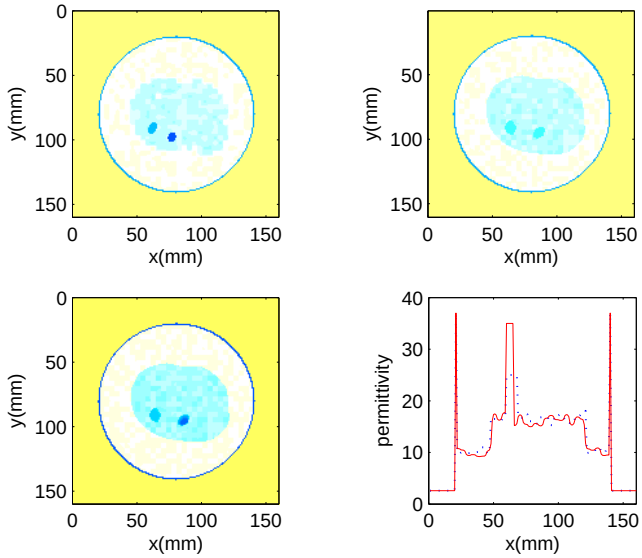

Figure 4.8: The behavior of the algorithm if two different tumors are present in the fibroglandular region tissue ($\epsilon_s^{tum_1} = 35$, $\epsilon_s^{tum_2} = 55$, $\epsilon_s^{fib} = 16.3$, $\epsilon_s^{fat} = 10$, and $\pm 15\%$ fluctuations). The top left image shows the reference permittivity profile illustrated by the dispersion Debye parameter ϵ_s. Top right image: reconstructed permittivity profile ϵ_s at the end of the third stage of the algorithm. Bottom left: final reconstructed profile. Bottom right: cross sections along the tumor location (y= 91 mm) of the reference ϵ_s (solid line) and the reconstructed ϵ_s (dashed line). Reconstructed values of the static permittivity are $\epsilon_1^{tum} = 27$ and $\epsilon_2^{tum} = 34$. The color map corresponds to the colorbar shown in Fig. 4.5.

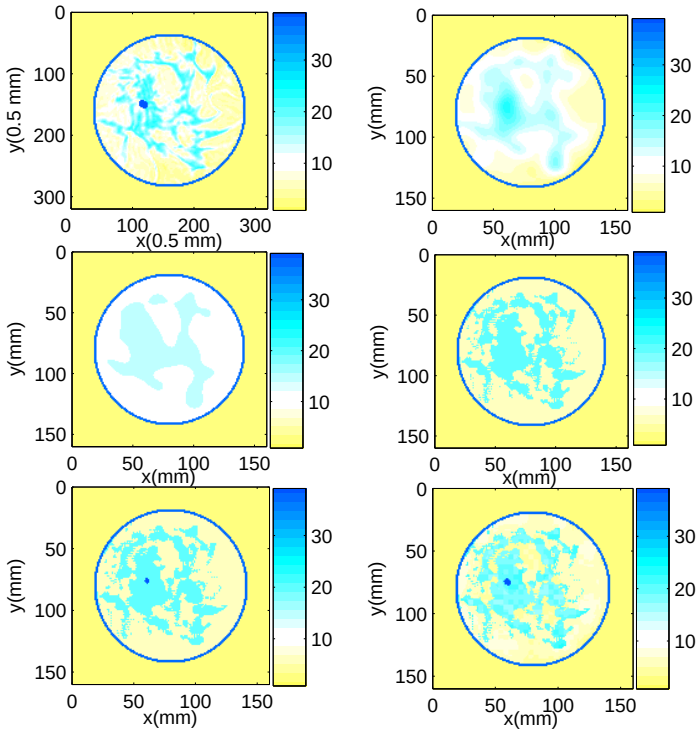

Figure 4.9: Numerical experiment for a case of a less dense breast with fibroglandular tissue intermixed with fat and a tumor of permittivity value $\epsilon_{st}^{tumor} = 50$. First row: reference permittivity profile (left) and the reconstructed pixel by pixel profile at the end of the first stage of the algorithm (right). Second row: initial guess (left) and final reconstruction at the end of the second stage (right) showing a good estimate of the fibroglandular shape. Bottom row: the reconstruction result at the end of the third stage (left) and at the end of our algorithm (right).

and their sizes are well estimated. However, the discrimination between these two tumors is only qualitative (which, as mentioned in section 4.3, might be due to the existence of local minima in the gradient search for these values). The reconstructed values of the static permittivity are here $\epsilon_1^{tum} = 27$ and $\epsilon_2^{tum} = 34$.

4.4.2 Set of experiments II

In the following experiments we do not assume that the average dielectric properties of the fatty and fibroglandular tissues are known. We only assume that the properties of the surrounding skin layer are known. We emphasize

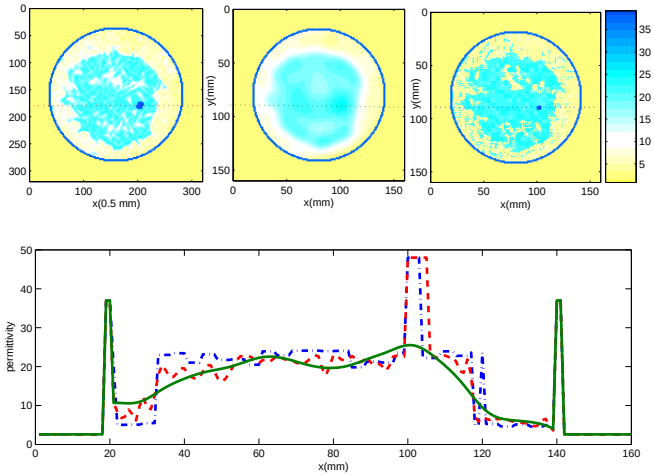

Figure 4.10: Numerical experiment for the breast with a large fibroglandular tissue intermixed with fat and a tumor of permittivity value $\epsilon_{st}^{tumor} = 48$. First row: reference permittivity profile (left), the pixel by pixel reconstructed image (center) and the reconstructed profile at the end of the algorithm (right). Second row: a cross section through the correct tumor position (dashed line), for the pixel by pixel reconstructed image (solid line) and the reconstructed image (dashed-dotted line), for constant x coordinate.

that the breast models used in this set of experiments mimic the complex network of glandular, connective and fatty tissue in the breast interior. The first numerical experiment has already been discussed during the description of the algorithm (see again Fig. 4.2). The results are displayed in a panel of six images: the top left image is the reference static permittivity distribution; the top right image is the result of the pixel by pixel reconstruction during the first stage of the algorithm; the center left image is the initial guess for the second stage; the center right image is the reconstruction at the end of the second stage; the bottom left image is the reconstruction at the end of the third stage; the bottom right image is the final reconstruction. This figure shows that (i) the tumor has been detected reliably, (ii) its location has been estimated correctly and (iii) its size and dielectric parameters have been approximated well. The static permittivity ϵ_s^{tum} of the inserted 8 mm-diameter tumor is 53 while the reconstructed value is 50. In addition, the reconstruction of the shape of the fibroglandular region was successful.

Figure 4.9 displays the results for another numerical experiment in which

the fibroglandular tissue is not compact but scattered within the breast interior. The breast contains predominantly fat intermixed with fibroglandular tissue. The inserted tumor has a static permittivity $\epsilon_s^{tum} = 50$. The arrangement of the images is the same as in Fig. 4.2. Although this case represents a more challenging reconstruction due to the complex shape of the fibroglandular region, the results show that the algorithm is able not only to detect and locate the presence of a small tumor, but also to provide a good estimate of its size and permittivity value (here 48).

In Fig. 4.10 we compare in more detail the reconstructions obtained with a 'classical' pixel-based strategy (upper row, center image) and with our level set based strategy (upper row, right image). The reference map of tissue structure (upper row, left image) contains predominantly fibroglandular tissue and a well differentiated layer of surrounding fatty tissue. The inserted tumor has a static permittivity value $\epsilon_s^{tum} = 48$. The lower row of Fig. 4.10 shows the cross sections through the three profiles as indicated in the first row (green solid line: pixel by pixel reconstruction, blue dashed-dotted line: our reconstruction, and red dashed line: real image). It is apparent that in this case, where the tumor is small and is located quite deep, the 'classical' pixel-based reconstruction could not detect reliably the presence of the tumor. On the other hand, we sucessfully accomplished the task of detecting, localizing and characterizing this small tumor. In addition, the reconstruction of the shapes of the healthy tissues and the estimation of their dispersion parameters was also successful.

In Fig. 4.11 we assess the potential of using our algorithm to reconstruct a tumor of irregular shape. The results of the study is displayed as in Fig. 4.10. This figure shows that, when the tumor is big enough (a 10-mm-diameter tumor in this case), the algorithm is able not only to locate the tumor well and to characterize its dielectric properties, but also to approximate quite well its irregular shape. We note that since the tumor is bigger in this example, one can now guess the presence of the tumor in the 'classical' pixel-based reconstruction shown in the center image of the upper row. However, the quality of our reconstruction, shown in the right image, is superior to the pixel-by-pixel reconstruction.

4.4.3 Set of experiments III

We show here an example of a complete reconstruction of a breast interior including the detection and characterization of a small tumor. Now, we do not assume any 'prior' knowledge about the interior of the breast (except of the structural information that the breast consists of skin, fat, fiber, glands

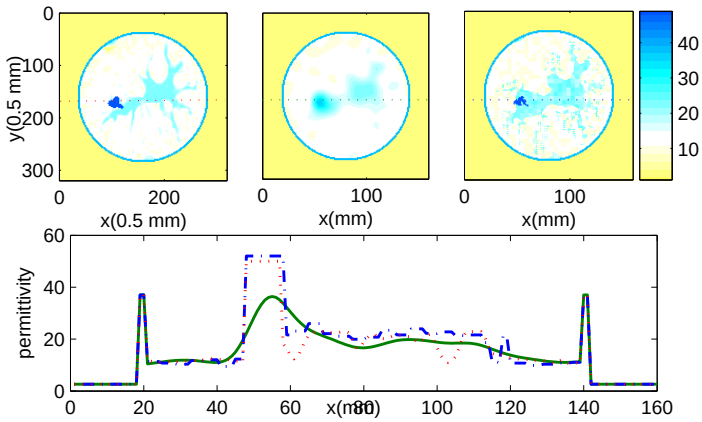

Figure 4.11: Numerical experiment for testing the capacity of the algorithm to approximate the irregular shape of the tumor with bigger size. Tumor's permittivity value is $\epsilon_{st}^{tumor} = 50$. First row: reference permittivity profile (left), the pixel by pixel reconstructed image (center) and the reconstructed profile at the end of the algorithm (right). Second row: a cross section through the correct tumor position (dashed line), for the pixel by pixel reconstructed image (solid line) and the reconstructed image (dashed-dotted line), for constant x coordinate.

and a possible tumor). Neither the details of the tissue structure nor the dielectric properties of the breast tissue are assumed to be known. Thus, in contrast to the previous experiments, the characteristics of the skin layer have to be reconstructed from the boundary data as well. In order to address this even more complex problem, we introduce two intermediate steps in our algorithm that will be called *pre-stage* 1 and *pre-stage* 2.

The *pre-stage* 1 is applied at the beginning of the algorithm (before the first stage). Assuming a fixed width of the skin layer, it is mainly devoted to the retrieval of the static permittivity of the skin, contained in $\kappa_{in} = \kappa_{skin}$. In the numerical example shown next, we fixed the width of the skin layer to 0.5 mm (typical values range from 0.5 to 3 mm). Since the data gathered on the boundary is also sensitive to the dielectric properties of the breast interior we simultaneously search for κ_{in} and $\kappa_{out} = \kappa_{interior}$. Thus, we start the algorithm with a fixed skin width and an initial piecewise profile as shown in the left upper image of Fig. 4.12. The initial values of the static permittivity inside and outside the skin layer, which regions are denoted by D_{in} and D_{out} respectively, are chosen arbitrarily but within the range of the values reported in the literature (in our case we choose $\epsilon_{s,in} = 30$ and $\epsilon_{s,out} = 8$). To correct these values we apply a similar formula as (4.21). We extract the following updates

$$\delta\kappa_{in,out} = \int_{D_{in,out}} G_{\mathcal{J}}[\kappa](\mathbf{x})\, d\mathbf{x} \tag{4.23}$$

from the boundary data. These updates are successively applied inside (D_{in}) and outside (D_{out}) the skin layer until the cost functional is minimized. Since higher frequencies penetrate less in the breast than lower frequencies, we use the 5 GHz data to update the static permittivity value inside the skin layer, and the 1 GHz data to update the value in the breast interior. The result of the *pre-stage* 1 is shown in the right upper image of Fig. 4.12.

Note that, so far, we have only estimated the values of the dielectric properties inside and outside the skin layer. The width of the skin layer has remained fixed. We postpone this search to the beginning of the third stage of our algorithm, right after the second stage, once we have found a good estimate of the shape of the fibroglandular region.

In *pre-stage* 2 we look for the properties of the skin layer (κ_{skin} and the width γ) along with better estimates of the remaining properties of the breast interior (except the possibility of a tumor) that would be affected for changes in κ_{skin} and γ. In other words, the unknows during the *pre-stage* 2 are: ψ, κ_{fib}, κ_{fat}, κ_{skin}, and γ. As in *pre-stage* 1 we use the 5 GHz data to estimate the properties of the skin layer (κ_{skin} and γ), and the lower frequencies (from 1 to 4 GHz) to estimate the properties in the interior (ψ, κ_{fib}, and κ_{fat}). We

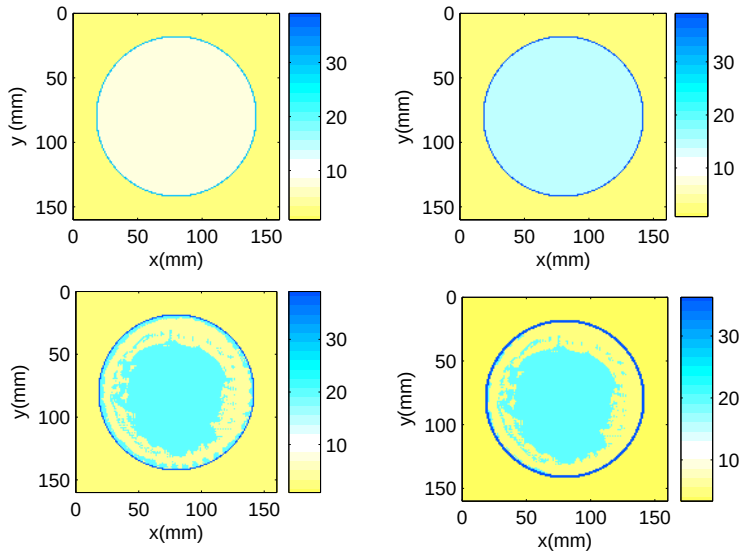

Figure 4.12: Example of two intermediate steps for the skin reconstruction. First row: arbitrary initial guess for domain and skin layer (left); updated domain and skin after the first step(right). Second row: static permittivity map as the result of the second stage of reconstruction(left) and updated reconstruction after the second step (right) as initial guess for the third stage.

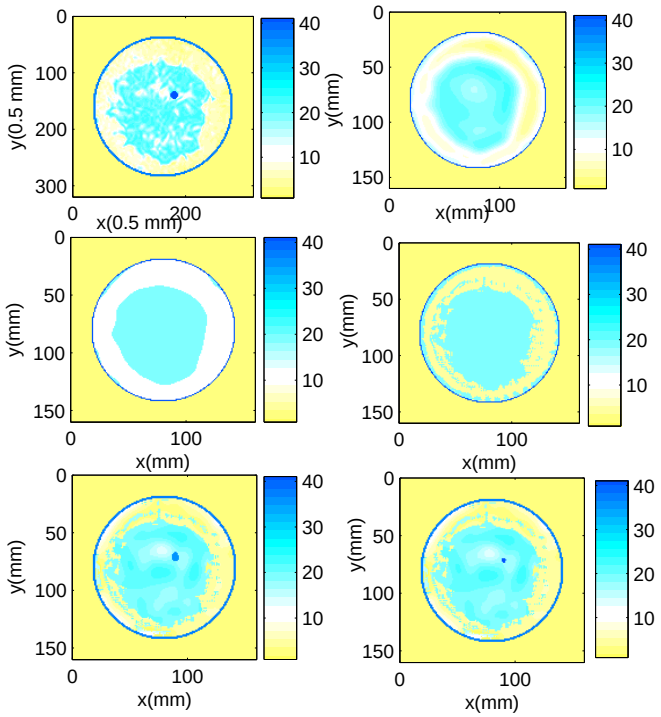

Figure 4.13: Numerical experiment with skin parameters reconstruction. The sequence of images is the same as in 4.2. 'Real'static permittivity of tumor is $\epsilon_s^{tum} = 48$ and the reconstructed is 50 .

apply (4.23) to update κ_{skin}, (4.21) to update κ_{fib} and κ_{fat}, and (4.18) to update ψ. Since, according to the literature, the skin width is restricted to $0.5 < \gamma < 3$ mm and our numerical resolution is about 0.5 mm, we apply a sampling strategy to find its optimal value. The bottom row of Fig. 4.12 shows the permittivity profile before (left image) and after (right) this *pre-stage*.

We note, that the computational cost of these two *pre-stages* is low. Only a few iterations are needed due to a quick convergence, and the estimates of the skin properties are generally very good. In this case, the reconstructed and real permittivities in the skin layer are $\epsilon_s^{skin} = 37$, and the reconstructed and the 'real' average skin width is 2 mm.

Figure 4.13 displays the complete reconstruction process of the static permittivity map for a case in which we insert a small tumor of permittivity $\epsilon_s^{tum} = 48$ in the fibroglandular region, as it is shown in the top left image. The arrangement of the images is the same as in Fig. 4.2. It is remarkable that, even in this case in which all the parameters of the breast interior including the non-uniform distribution of the dielectric properties of the healthy tissues (skin, fat and fibroglandular) and their shapes are reconstructed directly from the data, our algorithm is able to recover the main features of the breast interior, including the detection, localization and characterization of the small tumor.

Finally, a more detailed comparison between a 'classical' pixel-based reconstruction and our four-stage algorithm is presented in Fig. 4.14. Although the pixel-based approach gives rise to a good reconstruction of the fibroglandular region (see the center image of the top row), there is no indication of the presence of the tumor in that image. The cross sections shown in the bottom row show clearly the difference between the estimates obtained from these two approaches.

4.5 Summary

We have presented a novel shape based algorithm for the early detection and characterization of breast tumors from microwave data. A level set technique has been employed in order to free the iterative algorithm from topological restrictions. We have shown that the task of detecting and locating a hidden tumor by our algorithm is very stable and reliable. Once a tumor has been detected and localized, the algorithm is also able to estimate its size and correct permittivity value. Therefore, given certain knowledge of static permittivity values for different classes of tumors (such as benign or malig-

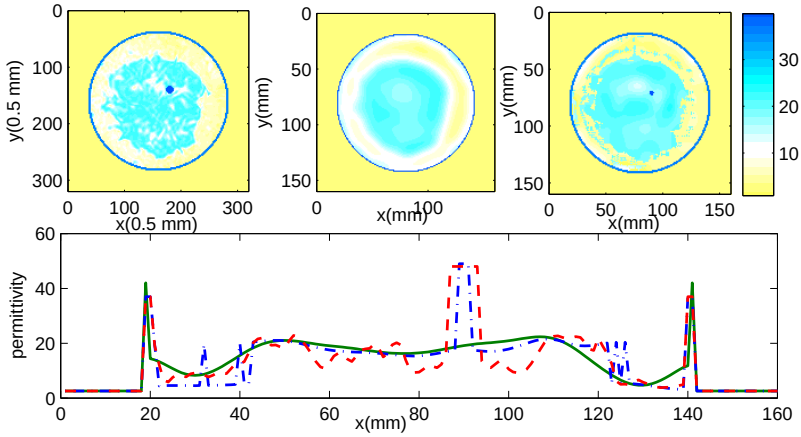

Figure 4.14: Comparison between the pixel by pixel reconstruction profile and the result by four-stages reconstruction, assuming unknown all the interior dielectric parameters of breast (from figure4.13). Tumor's static permittivity value is $\epsilon_{st}^{tumor} = 48$. First row: reference permittivity profile (left), the pixel by pixel reconstructed image (center) and the reconstructed profile at the end of the algorithm (right). Second row: a cross section through the correct tumor position (dashed line), for the pixel by pixel reconstructed image (solid line) and the reconstructed image (dashed-dotted line), for constant x coordinate.

nant tumors), our algorithm can provide reliable information which helps distinguishing between these different classes. The combination of all reliably estimated characteristics for a given tumor (dielectric properties, size, shape, etc.) could help the physician in the task of characterizing a detected tumor as 'benign' or 'malignant'.

The reconstructed spatial distributions in the microwave images do not exactly match the true ones, yet the estimations are very good in all cases. We believe that this study represents an important step in the development of shape based tomographic imaging strategies. Certainly, not all questions could be answered in the framework of this thesis. One issue which remains open is for example the validation against clinical microwave data to determine the potential and limitations of our algorithm in real applications. We mention, though, that we have tested our algorithm on the experimental 'Marseille data set' [4] with good success. The results of this study are shown in the next chapter 5.

Overall, this study shows the potential of our shape based reconstruction approaches for early breast cancer detection, given that the images were reconstructed without a priori information of the anatomical structure of the breast by means of an iterative algorithm of several stages. In particular, we have shown the inherent benefit of a complete structural inversion for detecting small tumors from microwave data compared to the more traditional pixel-based approach.

4.6 Publications and presentations

The following publications and presentations have resulted from the research described in this chapter.

Publications

- Natalia irishina,Miguel Moscoso and Oliver Dorn,' Microwave Imaging for Early Breast Cancer Detection Using a Shape-based Strategy, IEEE Trans.Biomed.Eng. (manuscript No. TBME-00362-2008.R2, accepted for publication), 2008.

Presentations

- 2007, October 15-20 Level set techniques for structural inversion in medical imaging, interdisciplinary workshop on mathematical meth-

ods in biomedical imaging and intensity-modulated radiation therapy (IMRT), Centro de Ricerca Matematica Ennio de Giorgi, Pisa, Italy.

- 2008, September 8-13, lecture 4, CIME summer school on Level Set and PDE based Reconstruction Methods: Applications to Inverse Problems and Image Processing, Cetraro (Cosenza), Italy.

- 2008, June 23 A level set technique for structural inversion in inverse, Mathematical Models in Life Sciences & Engineering conference, MIMS Workshop on New Directions in Analytical and Numerical Methods for Forward and Inverse Wave Scattering, University of Manchester, UK.

Chapter 5

Inversion against real data

5.1 Introduction

The inversion against real boundary data can be considered as an important test for the quality of numerical algorithms, even if these have been tested successfully already on simulated data. Simulated data have the danger of favouring the so-called 'inverse crime', which means that the model of simulating the data has the same complexity as the model used in the inversion. There are several 'tricks' which can be used in data simulation for avoiding this inverse crime (e.g. creating data with a different grid size than the one used for the reconstruction), but in the end a reconstruction algorithm needs to show that it works reliably with experimental data as well. Certainly, it cannot be expected that data from poorly performed physical experiments with unknown experimental errors can lead to good reconstructions. However, there have been published in the literature high quality experimental data from controlled setups which can be used for testing numerical algorithms. We will test our algorithm in this chapter against one of these data obtained from the data-set of the Marseille group at Institute Fresnel [4].

In this chapter we present the results of the reconstructions from real data using our novel numerical algorithm for breast cancer detection 4.3. Here we do not need to reconstruct the internal structure of the breast such that the basic model introduced in chapter 3 will be sufficient for processing the data. Certainly, the reconstruction problem is in principle similar to the tumor detection problem. with a slightly lower degree of complexity. For the reconstructions of this chapter we use the mathematical techniques described in chapter 3.

The testing of the algorithm is done by the inversion of the electromag-

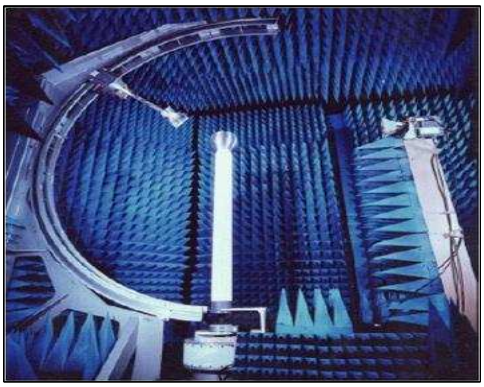

Figure 5.1: Anechoic camera in Institut Fresnel for generating the real data [4].

netic field scattered from cylindrical objects, as measured by the Institut Fresnel (http://www.loe.u-3mrs.fr/rf.htm). The experimental data were obtained in the anechoic chamber of the center Commun de Ressourses Microondes at Marseille, France (see figure 5.1). All details of the free-space camera used in the recovery from experimental data can be found in [4] and [42].

This chapter is organized as follows. In the following subsections 5.1.1 and 5.1.2 we describe the two setups used for gathering the experimental data. Section 5.2 describes the numerical model which is used for the reconstructions, and the calibration details. In section 5.3, we present the results of our reconstructions for both setups. Section 5.4 gives some conclusions.

5.1.1 First experimental setup

In figure 5.2 the scheme of the first experimental setup is shown. This setup corresponds to the experiments 1 and 2 described below, and consists of an anechoic chamber which is 14.5 m long, 6.50 m wide and 6.50 m high. The emitter is placed at a fixed position on a circular rail, while a receiver is rotating with an arm placed at the domain center. The emitter illuminates the targets from different positions by TM or TE waves, depending on whether the electric or magnetic field is parallel to the cylinder axis, respectively. The range of the frequencies is between 1 and 8 GHz. The receiving antennas are positioned on a circle of radius $d = 0.76$ m, and the emitter is located at a distance $d = 0.72$ m from the center of camera. The targets in all

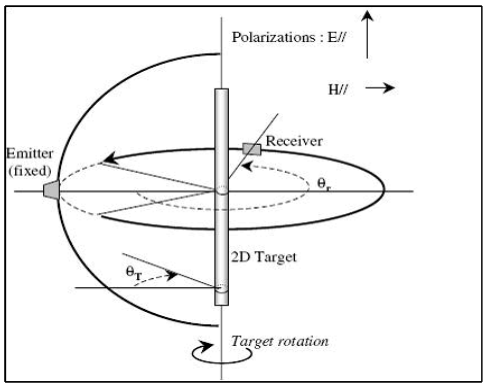

Figure 5.2: Scheme of the first experimental setup for the reconstruction from real data [4].

the experiments are designed to be very long in the direction perpendicular to the observation plane where the antennas are located. Therefore, a 2D dimensional configuration can be used for the reconstruction.

In the left image of Fig. 5.4, we illustrate the dielectrical reference profile for the first experimental setup. We choose the numerical domain to be a square of size 1.8 m x 1.8 m, such that all emitters and receivers are captured by the setup. We mention that our FDFD discretization is not optimal for this setup, due to the relatively large antenna-scatterer distance. Nevertheless, it can be applied as we show in this section. The size of the pixels in our setup is 0.01 m. The computational domain includes 8 PML at the edges in order to avoid numerical reflections from the artifial boundaries. The targets to be reconstructed are two long filled plastic cylinders with circular cross sections of radius $r = 0.015$ m and permittivity $\epsilon_i = 3.0 \pm 0.3$.

The data for the TM illumination at 1 and 2 GHz, corresponding to the 36 emitter positions and 49 receiver positions used in our reconstructions, are obtained from the datafile *twodielTM-8f.exp* [4].

5.1.2 Second experimental setup

In figure 5.3 we present the second experimental setup. It corresponds to the experiments 3 and 4 shown below. The same faradized anechoic chamber as in the first experimental setup is used in these experiments (see [42] for more details), but the dimension of the circular rail used to generate the

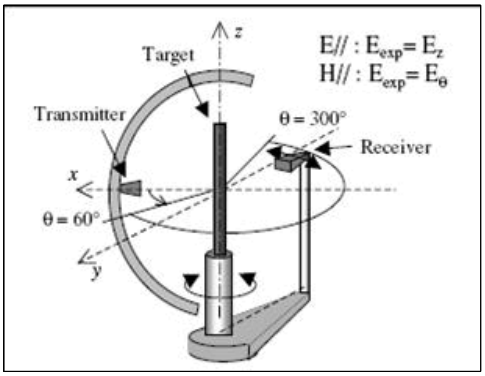

Figure 5.3: Scheme of the second experimental setup for the reconstruction from real data [42].

data is different and the emitting antenna can rotate around the object. The emitting and the receiving antennas are now placed at a distance of $d = 1.67$ from the the center of the domain. The receiver rotates around the center of the domain gathering data at 241 equidistant positions for each of the 8 emitter positions. In these experiments, the frequency of the illuminating waves ranges from 2 to 10 GHz.

In the left image of Fig. 5.6 we illustrate the configuration of this second experimental setup. Now, the targets to be reconstructed are a 8-cm-diameter foam cylinder (with permittivity $\epsilon_{i1} = 1.45 \pm 0.15$) and a 3.1-cm-diameter plastic cylinder (with permittivity $\epsilon_{i2} = 3.0 \pm 0.3$) embedded inside the foam cylinder. See the zoom at the top right corner of the left image of Fig. 5.6. We choose the size of the square domain being equal to 3.62 m x 3.62 m.

The data for the TM illumination at 2 GHz used in our reconstructions, corresponding to 8 emitter positions and 81 receiver positions, are obtained from the datafile $FoamDielIntTM$ [42].

5.2 Numerical model and calibration

As mentioned, the targets in all these experiments are designed very long in the direction perpendicular to the plane in which the antennas are located, such that a 2D approximation can be used for the reconstruction. Since we

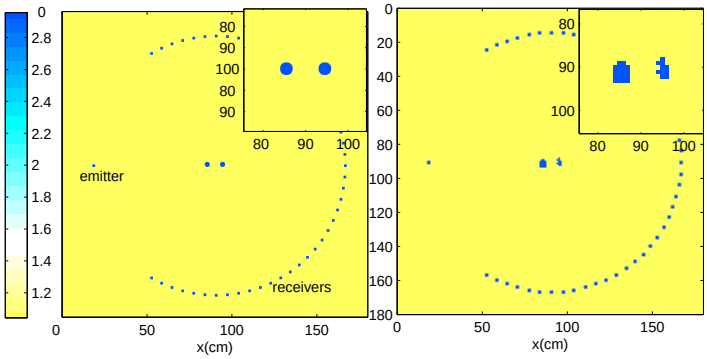

Figure 5.4: First reconstruction: two plastic cylinders of diameter 3.0 cm, separated 9.0 cm from each other. The permittivity values of the cylinders are assumed to be known. Left: 'true' permittivity profile. Right: reconstructed profile. The zooms at the upper right corners show the areas of interest.

only consider TM polarized illumination, the scalar Helmholtz equation

$$\nabla^2 u + \kappa(\mathbf{x}) u = -q(\mathbf{x}) \quad \text{in } \Omega, \tag{5.1}$$

with the standard *Sommerfeld radiation condition* approximates well the non-zero component of the electric field u. Here, $\kappa(\mathbf{x})$ is the complex wave number given by $\kappa(\mathbf{x}) = \omega^2 \mu_0 \epsilon_0 \left[\epsilon_r(\mathbf{x}) + i\frac{\sigma(\mathbf{x})}{\omega\epsilon_0}\right]$, where $\epsilon_r(\mathbf{x})$ is the relative permittivity and $\sigma(\mathbf{x})$ is the conductivity. q is the source.

Since in our model we use (unitary) point sources to generate the incident fields, and in the experiments these fields are generated by horn antennas, we first need to calculate the calibration factor for each frequency and source position in order to compare the simulated and the 'true' measured fields. To find the calibration factor we compute the ratio between these fields, and we multiply the simulated data by this factor [6]. It is obvious that this crude approximation of the highly directive antennas by a uniformly radiating line source reduces the quality of the reconstructions. We believe that better reconstructions would be possible with our reconstruction technique when using a more adapted numerical forward solver. Here, we have to assume that this modelling error adds to the data error as additional modelling noise.

5.3 Reconstruction results

5.3.1 First experimental setup

In the first two experiments our purpose is to detect and estimate the key properties of a pair of plastic cylinders within the medium. The number of cylinders is not known a priori in our reconstructions. In the first experiment, the average permittivity of the two cylinders is assumed to be known ($\epsilon_i = 3$), while in the second experiment it is unknown. The results are shown in Fig. 5.4 and Fig. 5.5, respectively.

Since in the first experiment we assume prior information about the dielectric properties of the objects, the inversion reduces to a shape optimization problem. We start our reconstruction with an initially positive level set function (equal to 1) in the entire domain, meaning that we do not assume any initial object within the medium. In the first update of our algorithm the possible objects are created automatically by lowering the initial level set function to negative values using the sensitivity structure of the data. This typically creates small objects very close to the correct locations, and only a few more iterations, as explained in [50], are needed to refine the details of their shapes. Fig. 5.4 shows the 'true' (left image) and reconstructed (right image) permittivity distributions. We also show the zoom of the area of interest at the top right corner of both images. We note that the reconstructed objects are well located and their sizes are well approximated.

In the second experiment, we consider the same experimental setup and dataset as in the previous case, but we do not assume the permittivity of the cylinders to be known. Therefore, we have generalized the algorithm in order to *simultaneously* (i) locate the objects, (ii) estimate their sizes, and (iii) estimate their dielectric properties. With this purpose, we monitor the minimized cost functional for a series of assumed permittivity values at the end of our algorithm in order to determine the value which yields the global minimum of the combined search for size and permittivity. The results of this reconstruction are displayed in Fig. 5.5 in a panel of four images. The top left image shows the 'true' permittivity profile, and the bottom left image shows the reconstructed profile at the end of our algorithm. The top right image shows the reconstructed profile at the end of an intermediate stage of our algorithm during which we only look for the locations and shapes of the objects, choosing an arbitrary permittivity value inside them. This value is chosen to be slightly bigger than the value for the background medium, so there is some contrast between the objects and the surrounding medium. Finally, the bottom right image shows the minimal values of the cost functional

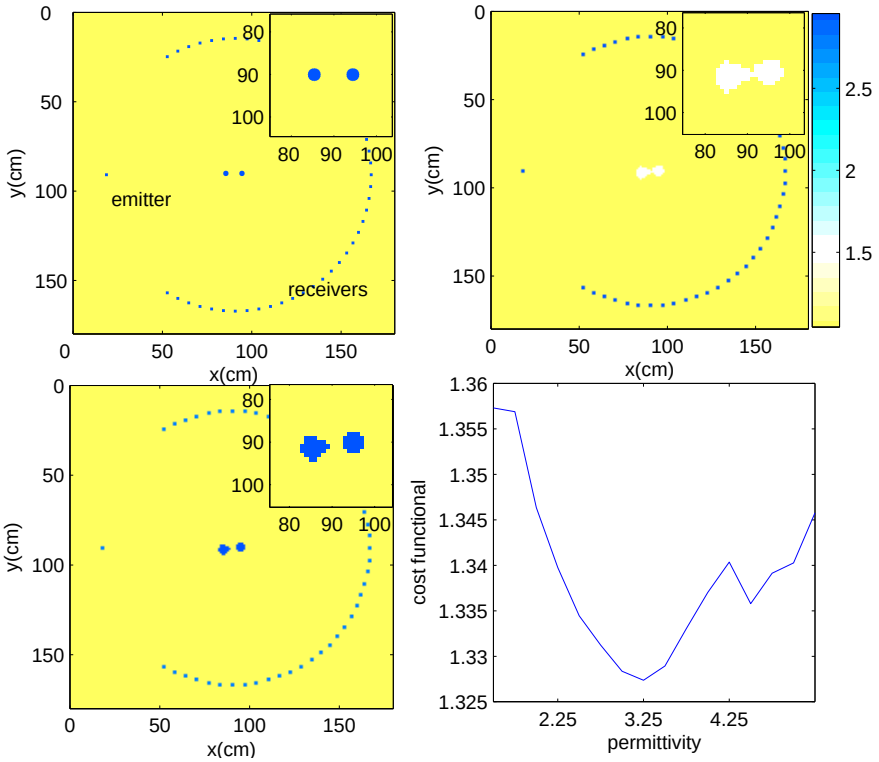

Figure 5.5: Second reconstruction: we consider the same objects as in the first experiment. However, we do not assume knowledge of the permittivity of the objects. Top left: 'true' profile. Top right: reconstruction at the end of the intermediate stage of the algorithm. Bottom left: finally reconstructed profile. Bottom right: minimal cost value for each permittivity value inside the cylinders.

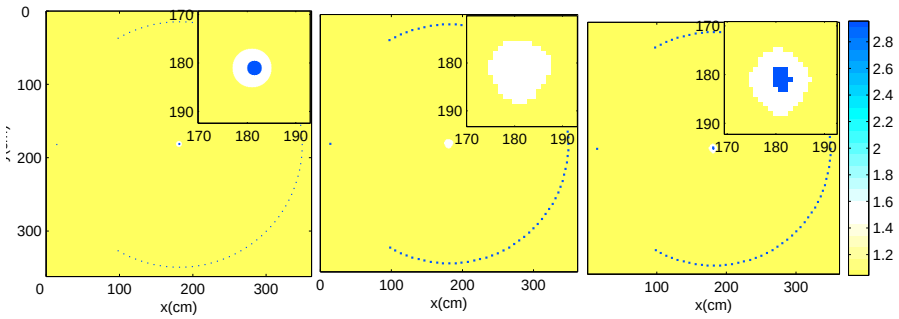

Figure 5.6: Third reconstruction: a non-homogeneous object consisting of a 3-cm-diameter plastic cylinder embedded in a 8-cm-diameter foam cylinder. From left to right the images illustrate: the 'true' profile, the reconstructed profile at the end of the intermediate stage of the algorithm, and the finally reconstructed profile. The zooms at the upper right corners show only the areas of interest.

achieved during the last stage of the algorithm, where we *simultaneously* look for the shapes and permittivities of the detected objects. We observe that in this case, the reconstructed objects are also well located and their sizes are well approximated. Moreover, the estimated permittivity value inside the cylinders (here 3.25) is within the range of the values given in the experiment.

5.3.2 Second experimental setup

In the third and the fourth experiments we reconstruct a more complex object: a plastic cylinder embedded in a foam cylinder (see the left image in Fig. 5.6). In the third experiment we assume the permittivity average values of these two parts of the object to be known. Therefore, $\epsilon_{i1} = 1.45$ and $\epsilon_{i2} = 3.0$ are known and fixed during this reconstruction. The results of this reconstruction are displayed in Fig. 5.6. The left image corresponds to the 'true' permittivity profile. The central image is the result at the end of the intermediate stage of the algorithm where we only search for a homogeneous object, with permittivity $\epsilon_{i1} = 1.45$, using the first level set function. The right image of Fig. 5.6 shows the final reconstruction achieved at the end of the second stage of the algorithm, where we introduce the second level set

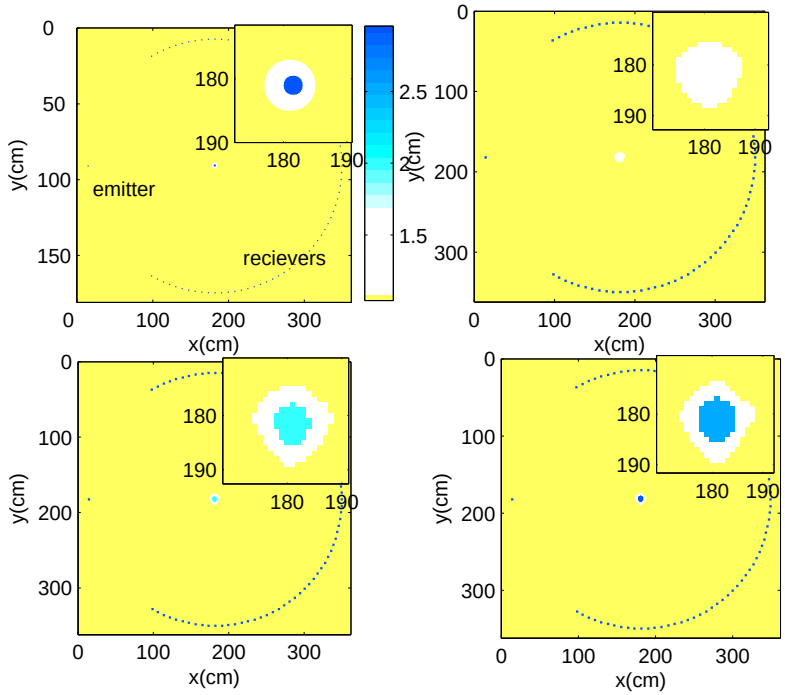

Figure 5.7: Fourth reconstruction: the same object as in the third experiment. However, we do not assume to know the piecewise constant permittivity distribution. Top left: 'true' profile. Top right: reconstructed profile at the end of the first stage of our algorithm. Bottom left: reconstructed profile at the end of the second stage of our algorithm. Bottom right: finally reconstructed profile.

function searching for an additional region with a possibly higher contrast value $\epsilon_{i2} = 3.0$. As it can be observed in this image, the object is well located and its structure is well estimated.

In the next experiment, shown in Fig. 5.7, we do not assume the knowledge of the piecewise constant permittivity distribution of the object. The 'true' permittivity profile is depicted in the top left image of Fig. 5.7. We start the reconstruction by considering only one level set function (initially equal to 1 in the entire domain) that will define an object with a permittivity value slightly higher than the background medium (here, $\epsilon_{i1} = 1.15$) once it is lowered to negative values at the first iterations of the algorithm. A few more iterations lead to the result at the end of this first stage presented in the top right image of Fig. 5.7. Since the 'true' object has a higher average per-

mittivity value than the one assumed during this stage, this is compensated by the algorithm by reconstruction a slightly bigger object at this stage. At the beginning of the second stage of the algorithm, we introduce a second level set function (also, initially equal to 1 in the entire domain) to look for a higher contrast region. The second level set function will define a region with permittivity $\epsilon_{i2} = 2.0$. After a few more iterations, we find the result presented in the bottom left image. During the third, and final, stage of the algorithm we gradually change the permittivities inside the two recovered regions. We define a parameter grid over the two-dimensional parameter space $\epsilon_{i1} - \epsilon_{i2}$ and we carry out a shape optimization problem for each node of the parameter grid. We monitor the minimized cost values for each node, and we choose the reconstruction corresponding to the global minimum of this two-dimensional graph as our final reconstruction. The result of this two dimensional search is displayed in the bottom right image of the Fig. 5.7. The estimated values of the permittivities in the final reconstruction are $\epsilon_{i1} = 1.25$ and $\epsilon_{i2} = 2.5$, which are slightly lower than the real ones.

5.4 Summary

In this chapter we presented the results of testing a novel nonlinear inversion algorithm based on level sets and designed for the early detection of breast cancer, as described in this thesis, against the experimental 'Marseille data'. This study shows that our algorithm gives good reconstructions when it is used with experimental data. It also shows the potential of a shape based reconstruction approach for detecting and imaging dielectric objects from real data.

5.5 Publications and presentations

The following publications and presentations have resulted from the research described in this chapter.

Publications

- (2008) Detecting and imaging dielectric objects from real data: a shape based approach, Irishina N, Alvarez D, Dorn O and Moscoso M, Mathematical and Computer Modelling (submitted)

Presentations

- Detecting and imaging dielectric objects from real data: a shape based approach, XI JORNADAS Mathematical Models in Medicine, Business & Engineering Valencia, September 8th-11th, 2008

Chapter 6

Conclusions and future work

In this thesis the image reconstruction method from the microwave boundary data was discussed. We have presented a novel shape based numerical algorithm for the early detection and characterization of breast tumors from microwave data. As the regularization tools, the prior information of the typical ranges of the dielectric permittivity values for the breast tissues components and the existence of the well shaped interfaces between the different breast tissues have been used. These prior data restrict the space of possible solutions of the ill-posed inverse problem. A level set technique has been employed in order to represent implicitly the interfaces of the different breast components and to free the iterative algorithm from topological restrictions. We have shown that the task of detecting and locating a hidden tumor by our algorithm is very stable and reliable. Once a tumor has been detected and localized, the next stages of the algorithm are able to estimate its correct permittivity value simultaneously with its size and location. Therefore, given certain knowledge of static permittivity values for different classes of tumors (such as benign or malignant tumors), our algorithm can provide reliable information which helps distinguishing between these different classes. The combination of all reliably estimated characteristics for a given tumor (dielectric properties, size, shape, etc.) could help the physician in the task of characterizing a detected tumor as 'benign' or 'malignant'.

In chapter 1 we have overviewed the main directions in the scientific research concerning the breast cancer detection, between them the microwave imaging, which is the object of this thesis. Afterwards, in chapter 2 we have defined the direct problem in microwave imaging and our mathematical and numerical 2D model for the case of the early breast cancer detection.

In chapter 3 we have presented the general theoretical framework for the novel reconstruction algorithm. In this thesis we have followed an optimiza-

tion approach when iteratively reconstructing the distribution of dielectric parameters structure of the breast interior. The objective to reduce and, eventually, to minimize the least squares cost functional, has been undertaken by its evolution in the decreasing direction, using the level set functions for the reconstruction of the object shapes, since it solves the problem of the topological changes during the reconstruction and stabilizes the inversion.

In the next chapter 4 we have discussed the application of the novel algorithm to the realistic breast models, based on the real magnetic resonance images.

Finally, in chapter 5 we have presented the numerical results after successfully proved our numerical algorithm against the real database obtained in the anechoic chamber of the center Commun de Ressourses Micro-ondes at Marseille, France.

Overall, this study shows the potential of shape based reconstruction approaches for early breast cancer detection using microwaves. The distributions of the dielectric parameters were reconstructed without a priori information of the anatomical structure of the breast through an iterative algorithm. The reconstructed spatial distributions in the microwave images do not exactly match the true ones, yet the estimations are very good in all cases. We believe that this study represents an important step in the development of shape based tomographic imaging strategies. Although, further questions remain as to the validation against clinical microwave data to determine its real potential and limitations.

In our future investigations we are planning to reconstruct not only the static permittivity of tumor but more dielectric parameters as well. In our future research we plan to extend our algorithm to a 3D situation. Another way for the future investigation is to use the statistical Bayesian approach: to estimate the posterior probability distribution of the unknown parameters, given the data and the prior information about the sought solution. the reconstructions using the statistical approach [55], [56], [63].

In lately appeared work of A. Carpio and M-L. Rapn the method of topological derivative was used for the reconstruction of objects shapes [19]. We are looking forward in using this method in our future work as well.

Bibliography

[1] B. Alberts, D. Bray, J. Lewis, M. Raff, K. Roberts, and J.D. Watson, "Molecular Biology of the Cell", Chapter 10, 2nd ed., New York: Garland, 1989.

[2] S. R. Arridge, "Optical tomography in medical imaging", *Inverse Problems*, vol. 15, R41, 1999.

[3] S. R. Arridge, J. P. Kaipio, V. Kolehmainen, M. Schweiger, E. Somersalo, T. Tarvainen and M. Vauhkonen,"Approximation errors and model reduction with an application in optical diffusion tomography", *Inverse Problems*, vol. 22, 175-195, 2006.

[4] K. Belkebir and M. Saillard, "Special section : Testing inversion algorithms against experimental data", *Inverse Problems*, vol. 17, pp. 1565-1571, 2001.

[5] J. Berenger,"A perfectly matched layer for the absorbtion of electromagnetic waves," *J. Math. Phys.*, vol. 114, pp. 185-200, 1994.

[6] R. F. Bloemenkamp, A. Abubakar and P. M. van den Berg, "Inversion of experimental multi-frequency data using the contrast source inversion method", *Inverse Problems*, vol.17, pp. 1611-1622, 2001.

[7] P. Blomgren, G. Papanicolaou and H. Zhao,"Super-Resolution in Time-Reversal Acoustics", *Journal of the Acoustical Society of America*, vol. 111, pp. 230-248, 2002.

[8] E. J. Bond, X. Li, S. C. Hagness, and B. D. Van Veen,"Microwave imaging via space-time beamforming for early detection of breast cancer," *IEEE Trans. Antennas Propagat.*, vol. 51, pp. 1690-1705, 2003.

[9] L. Borcea, "Electrical impedance tomography, topical review," *Inverse Problems*, vol. 18, pp. 99-136, 2002.

[10] L. Borcea, G. Papanicolaou, and C. Tsogka, "Theory and applications of time reversal and interferometric imaging," *Inverse Problems*, vol. 19, pp. 5139-5164, 2003.

[11] L. Borcea, G. Papanicolaou, and C. Tsogka, "Interferometric array imaging in clutter," *Inverse Problems*, vol. 21, pp. 1419-1460, 2005.

[12] L. Borcea, G. Papanicolaou, and C. Tsogka, "Coherent Interferometric Imaging," *Geophysics*, vol. 71, pp. S1165-S1175, 2006.

[13] L. Borcea, G. Papanicolaou, and C. Tsogka, "Adaptive interferometric imaging in clutter and optimal illumination", *Inverse Problems*, vol. 22, pp. 1405-1436, 2006.

[14] L. Borcea, G. Papanicolaou, and C. Tsogka, "Optimal Waveform Design for Array Imaging", submitted for publication.

[15] A. Broquetas, J. Romeu, J. M. Ruis, A. R. Elias-Fuste, A. Cardama, and L. Jofre, "Cylindrical geometry: A further step in active microwave tomography", *IEEE Trans. Microwave Theory Tech.*, vol. 39, pp. 836-844, 1991.

[16] B. Brooksby, B. W. Pogue, S. Jiang, H. Dehghani, S. Srinivasan, C. Kogel, T. D. Tosteson, J. Weaver, S. P. Poplack, and K. D. Paulsen, "Imaging breast adipose and fibroglandular tissue molecular signatures by using hybrid MRI-guided near-infrared spectral tomography," *Proc. Natl. Acad. Sci. USA.*, vol. 103, pp. 8828-8833, 2006.

[17] A. E. Bulyshev, S. Y. Semenov, A. E. Souvorov, R. H. Sveson, A. G. Nazarov, Y. E. Sizov, and G. P. Tatsis, "Computational modeling of three-dimensional microwave tomography of breast cancer," *IEEE. Trans. Biomed. Eng.*, vol. 48, pp. 1053- 1056, 2001.

[18] A. M. Campbell, D. V. Land,"Dielectric properties of female human breast tissue measured in vitro at 3.2 GHz," *Phis. Med. Biol.*,vol.37, pp. 193-210, 1992.

[19] A. Carpio and M-L. Rapn, "Solving inhomogeneous inverse problems by topological derivative methods," *Inverse Problems*, vol 24, pp. 45014-45046, 2008.

[20] K. L. Carr,"Microwave radiometry: its importance to the detection of cancer" IEEE Trans. Microwave Theory Tech., vol. 37, pp. 1862-1869, 1989.

[21] K. L. Carr, P. Cevasco, P. Dunlea, J. Shefer,“ Radiometric sensing : an andjuvant to mammography to determine breast biopsy”, IEEE MTT-S Int.Microwave Symp.Dig., vol. 2, pp. 929-932, 2000.

[22] T. F. Chan and X. C. Tai, “Level set and total variation regularization for elliptic inverse problems with discontinuous coefficients,” *J. Comput. Phys.* , vol. 193, pp. 40-66, 2003.

[23] S. S. Chaudhary, R. K. Mishra, A. Swarup, and J. M. Thomas, “Dielectric properties of normal and malignant human breast tissues at radiowave and microwave frequencies,” *Ind. J. Biochem. Biophys.*, vol. 21, pp. 76-79, 1984.

[24] W.C. Chew,“Waves and Fields in Inhomogeneous Media”, 2nd edition, New York, IEEE.

[25] M. Cheney, D. Isaacson, J. C. Newell,“Electrical impedance tomography”, SIAM, Rev. 40, pp. 85-101, 1999.

[26] M. Converse, E. J. Bond, B. D. Van Veen, and S. C. Hagness, “A computational study of ultra-wideband versus narrowband microwave hyperthermia for breast cancer treatment”, *IEEE Trans. Microwave Theory Tech.*, vol. 54, pp. 2169-2180, 2006.

[27] G. Derveaux, G. Papanicolaou, and C. Tsogka, “Resolution and denoising in near-field imaging,” *Inverse Problems*, vol. 22, pp. 1437-1456, 2006.

[28] O. Dorn,“ A transport-backtransport method for optical tomography”,*Inverse Problems*,vol. 14, pp. 1107-1130, 1998.

[29] O. Dorn, H. Beretete-Aguirre, J. G. Berryman, G. C. Papanicolaou, “A non linear inversion method for 3D-elcetromagnetic imagingusing adjoint fields” *Inverse Problems*, vol. 15, pp. 1523-1558, 1999.

[30] O. Dorn, E. Miller, and C. Rappaport, “A shape reconstruction method for electromagnetic tomography using adjoint fields and level sets,” *Inverse Problems*, vol. 16, pp. 1119-1156, 2000.

[31] O. Dorn and D. Lesselier, “Level set methods for inverse scattering,” *Inverse Problems*, vol. 22, pp. R67-R131, 2006.

[32] J. G. Elmore, M. B. Barton, V. M. Moceri, S. Polk, P. J. Arena, and S. W. Fletcher, "Ten-year risk of false positive screening mammograms and clinical breast examinations", *The New England J.of Med.*, vol. 338, pp. 1089-1096, 1998.

[33] H. W. Engl, M. Hanke and A. Neubauer, "Regularization of inverse problems", *Mathematics and its Applications.*, Kluwer Acadenic Publishers, vol. 375, 1996.

[34] M. El-Shenawee, and E. L. Miller, "Spherical harmonics microwave algorithm for shape and location reconstruction of breast cancer tumor", *IEEE Trans. Med. Imag.*, vol. 25, pp. 1258-1271, 2006.

[35] E. C. Fear and M. A. Stuchly, "Microwave system of breast cancer," *IEEE Microwave Guided Wave Lett.*, vol. 9, pp. 470-472, 1999.

[36] C. E. Fear, S. C. Hagness, P. M. Meaney, M.Okoniewski, and M. A. Stuchly, "Enhancing breast tumor detection with near-field imaging" *IEEE Microwave Mag.*, pp. 48-56, March 2002.

[37] E. C. Fear, P. M. Meaney and M. A. Stuchly, "Microwaves for breast detection?" *IEEE Potencials*, February-March, pp. 12-18, 2003.

[38] M. Fink, 'Time reversal of ultrasonic fileds - Part I: Basic principles,'*IEEE Trans. Ultrasonic Ferroelectr. Freq. Control*, vol. 39, pp. 555-567, 1992.

[39] K. R. Foster, H. P. Schwan , "Dielectric properties of tissue", *CRC Crit.Rev.Biomed.Eng.*, vol. 17, pp. 25-104, 1989.

[40] C. Gabriel, S. Gabriel, R. W. Lau, and E. Corthout, "The dielectric properties of biological tissues: Part I, II, and III," *Phys. Med. Biol.*, vol. 41, pp. 2231-2249, 1996.

[41] S. Gabriel, R. W. Lau, and C. Gabriel,"The dielectric properties of biological tissues: III. Parametric models for the dielctric spectrum of tissues," *Phys. Med. Biol.*, vol. 41, pp. 2271-2293, 1996.

[42] J. M. Geffrin, P. Sabouroux and C. Eyraud, "Free space experimental scattering database continuation : experimental set-up and measurement precision", *inverse Problems*, vol. 21, pp. S117-S130, 2005.

[43] D. K. Ghodgaonkar and A. B. Daud ,"Calculation of Debye Parameters of Single Debye Relaxation Equation for Human Skin in Vivo," *Proceed. Nat. Conf. on Telecom. Technology.*, Shah Alam, Malaysia, 2003.

[44] P. Gonzalez-Rodriguez, M. Kindelan, M. Moscoso, and O. Dorn, "Hystory matching problem in reservoir engineering using the propagation-backpropagation method," *Inverse Problems*, vol. 21, pp. 565-590, 2007.

[45] B. Guo, L. Jian, and H. Zmuda, "A new FDTD formulation for wave propagation in biological media with Cole-Cole model", *IEEE Microw. Wireless Compon. Lett.*, vol. 16, pp. 633-635, 2006.

[46] S. C. Hagness, A. Taflove, and J. E. Bridges,"Two-dimensional FDTD analysis of a pulsed microwaved confocal system for breast cancer detection: fixed-focus and antenna-array sensors," *IEEE Trans. Antennas Propagat.*, vol. 45, pp. 1470-1479, 1998.

[47] S. C. Hagness, A. Taflove, and J. E. Bridges,"Three-dimensional FDTD analysis of a pulsed microwaved confocal system for breast cancer detection: design of an antenna-array element," *IEEE Trans. Antennas Propagat.*, vol. 47, pp. 783-791, 1999.

[48] M. A. Hernández-López,M. Quintillán-González, S. González García, A. Rubio Bretones, and R. Gómez Martín, "A rotating array of antennas for confocal microwave breast imaging", *Microwave and Optical Tech. Lett.*, vol. 39, pp. 307-311, 2003.

[49] N. Irishina, M. Moscoso, and O. Dorn,, "Detection of small tumors in microwave medical imaging using level sets and MUSIC,", *Proc. PIERS, Cambridge*, pp. 43-47, 2006.

[50] N. Irishina, O. Dorn, and M. Moscoso,, "A level set evolution strategy in microwave imaging for early breast cancer detection ,", *Computers and Mathematics with Applications*, vol. 56, pp. 607-618, 2008.

[51] S. Jacobsen and P. R. Stauffer. " Can we settle with single-band radiometric temperature monitoring during hyperthermia treatment of chestwall recurrence of breast cancer using a dual-mode transceiving applicator?", *Physics in Medicine and biology*, vol. 52, pp. 911 , 2007.

[52] L. Jofre, M. S. Hawley, A. Broquetas, E. de los Reyes, M. Fernando, and A. R. Elias-Fuste, "Medical imaging with a microwave tomographic scanner", *IEEE Trans. Biomed. Eng.*, vol. 37, pp. 303-312, 1990.

[53] W. T. Joines, Y. Zhang, C. Li, and R. L. Jirtle, "The measured electrical properties of normal and malignant human tissues from 50 to 900 MHz," *Med. Phys.*, vol. 21, pp. 547-550, 1994.

[54] J. P. Kaipio, V. Kolehmainen, E. Somersalo and M. Vauhkonen, "Statistical inversion and Monte Carlo sampling methods in electrical impedance tomography," *Inverse Problems*, vol. 16, pp. 1487-1522, 2000.

[55] J.Kaipio and E. Somersalo, " Statistical and Computational Inverse Problem," *Applied Mathematical Sciences*, vol. 160, Springer, 2004.

[56] J. P. Kaipio, V. Kolehmainen, M. Vauhkonen and E. Somersalo, Inverse problem with structural prior information, *Inverse Problems*, vol. 15, pp. 713-729, 1999.

[57] K. Kang , X. Chu, R. Dilmaghani and M. Ghavami," Low-complexity Cole-Cole expression for modelling human biological tissues in FDTD method," *Electronic letters* vol.43, n. 3, 2007.

[58] J.B. Keller, *Inverse Problems*, Am. Math. Monthly, vol. 83, pp. 107-118, 1976.

[59] K. R. Foster and H. P. Schwan," Dielectric properties of tissues and biological materials: a critical review," *Critical Reviews in Biomedical Engineering*, vol.17, pp. 25-104, 1989.

[60] M. Kilmer, E. Miller, C.Pappaport" Preconditionres for structural matrices arising in subsurface object detection" Center for Electromagnetic reseach , Electrical and Computer Engineering department, North-Estern University, Boston, MA 02115 , 2002.

[61] A. D. Kim and M. Moscoso, "Radiative transport theory for optical molecular imaging," *Inverse Problems*, vol. 22, pp. 23-42, 2006.

[62] V. Kolehmainen, M. Lassas, P. Ola," Electrical Impedance Tomography Problem With Inaccurately Known Boundary and Contact Impedances," *IEEE Trans. Med. Imaging* , vol.27, pp. 1404-1414, 2008.

[63] V. Kolehmainen, S. R. Arridge, M. Vauhkonen and J. P. Kaipio. "Simultaneous reconstruction of internal tissue region boundaries and coefficients in optical diffusion tomography," *Phys. Med. Biol.*, vol. 45, pp. 3267-3283, 2000.

[64] S. Kyriakides, "The Beacon", *Breast Cancer Network Australia's magazine*, vol. 29, p. 10, 2004.

[65] P. Kosmas and C. Rappaport, "Time reversal with FDTD method for microwave breast cancer detection," *IEEE Trans. Microw. Theory Tech.*, vol. 53, pp. 2317-2322, 2005.

[66] P. Kosmas and C. Rappaport, "FDTD-basedtime reversal for microwave breast cancer detection:Localization in three dimensions ," *IEEE Trans. Microw. Theory Tech.*, vol. 54, pp. 1921-1927, 2006.

[67] P. Kosmas and C. Rappaport, "A matched filter FDTD-basedtime reversal approach for microwave breast cancer detection ," *IEEE Trans. Antennas Propagat.*, vol. 54, pp. 1257-1264, 2006.

[68] R. A. Kruger, W. L. Kiser , D. R Jr Reinecke, G. A. Kruger, R.L.Eiseinhart, "Thermoacoustic computed of the breast at 434 MHz ," IEEE MTT-S Int. Microwave Symp. Dig., vol. 2, pp. 591-594, 1999.

[69] G. Ku and L. V. Wang, "Thermoacoustic computed of the breast at 434 MHz ," *Med. Phys.*, vol. 27, pp. 1195-1202, 2000.

[70] K. J. Langerberg, 'Introduction to the special issue on inverse problems,' *Wave Motion*, vol. 11, pp. 99-112, 1989.

[71] M. Lazebnik,L.McCartney, D. Popovic, C. Watkins, M. Lindstrom, J. Harter, S. Sewall, A. Magliocco, J. Booske, M. Okonievki and S. Hagness,"A large-scale study of the ultrawideband microwave dielectric properties of normal breast tissue obtained from reduction surgeries ," *Phys. Med. Biol.*, vol. 52, pp. 2637-2656, 2007.

[72] M. Lazebnik, D. Popovic, L. McCartney, C. Watkins, M. Lindstrom, J. Harter, S. Sewall, T. Ogilvie, A. Magliocco, T. Breslin, W. Temple, D. Mew, J. Booske, M. Okonievki and S. Hagness,"A large-scale study of the ultrawideband microwave dielectric properties of normal,benign and malignant breast tissues obtained from reduction surgeries ," *Phys. Med. Biol.*, v.52, pp. 6093-6115, 2007.

[73] M. Lazebnik, M. Okoniewki, J. Booske and S. Hagness,"Highly Accurate Debye Models for Normal and Malignant Breast Tissue Dielectric Properties at Microwave Frequencies ," *IEEE Microwave and Wireless Components Letters*, vol. 17, pp. 822-824, 2007.

[74] X. Li and S. C. Hagness, B. D. Van Veen, and D. van derWeide, "Experimental investigation of microwave imaging via space-time beamforming for breast cancer detection," *IEEE MTT-S Int. Microwave Symp. Dig.*, pp. 379-382, 2003.

[75] X. Li and S. C. Hagness, "A confocal microwave imagingalgorithm for breast cancer detection," *IEEE Microwave Wireless Components Lett.*, vol. 11, pp. 130.132, 2001.

[76] A. Litman, D. Lesselier and D.Santosa, "Reconstruction of two-dimensional binary obstacle by controlled evolution of a level-set ," *Inverse Problems*, vol. 14, pp. 685-706, 1998.

[77] A. Litman, "Reconstruction by level sets of n-ary scattering obstacles," *Inverse Problems*, vol. 21, pp. 1-22, 2005.

[78] P. M. Meaney, K. D. Paulsen, A. Hartov, and R. K. Crane, "An active microwave imaging systemfor reconstruction of 2-D electrical property distribution," *IEEE Trans. Biomed. Eng.*, vol. 42, pp. 1017-1026, 1995.

[79] P. M. Meaney, M. W. Fanning, D. Li, S. P. Poplack, and K. D. Paulsen, "A clinical prototype for active microwave imaging of the breast," *IEEE Trans. Microwave Theory Tech.*, vol. 48, pp. 1841-1853, 2000.

[80] P. M. Meaney, K. D. Paulsen, and M. W. Fanning, "Microwave imaging for breast cancer detection: preliminary experience," *Proc. SPIE-Int. Soc. Opt. Eng.*, vol. 3977, pp. 308-319, 2000.

[81] P. M. Meaney, M. W. Fanning, T. Raynolds, C. J. Fox, Q. Fang, C. A. Kogel, S. P. Poplack, and K. D. Paulsen, "Initial clinical experience with microwave breast imaging in women with normal mammography", *Acad. Radiol.*, vol. 14, pp 207-218, 2007.

[82] P. M. Meaney, E. Godshalk, T. Raynolds, G. Burke, K. Paulsen, "Microwave Tomographic Techiques for Explosive and Flammable Liquid Detection," *23rd Annual Review of Progress in Applied Computacional Electromagnetics* Verona, Italy, March 19-23, 2007.

[83] B. Mouty, B. Bocquet, N. Ringot, N. Rocourt, P. Devos, "Microwave radiometric imaging for the chracterization of breast tumores ," *J. Appl. Phys.*, vol. 10, pp. 73-78, 2000.

[84] F. Natterer and F. Wubbeling, "Mathematical Methods in Image Reconstruction ," *SIAM*, Philadelphia, 2001.

[85] F. Natterer, "The Mathematics of Computerized Tomography", Teubner-Wiley 1986, Russische Ausgabe MIR, Moskau 1990. Reprinted in *SIAM Classics in Applied Mathematics*.

[86] T. R. Nelson, L. Cervino, J. M. Boone and K. K. Lindfors,"Classification of breast computed tomography data," *Med. Phys.*, v.35, , no.3, pp. 1078-1086, 2008.

[87] M. Okonievski, M. Mrozowski, and M. A. Stuchly, "Simple treatment of multi-term dispersion in FDTD", *IEEE Microw. Guided Wave Lett.*, vol. 7, pp. 121-123, 1997.

[88] S. Osher, J. A. Sethian, "Fronts propagating with curvature-dependent speed: algorthms based on Hamilton-Jacobi formulations", *J. Comput. Phys.*, vol. 79, pp. 12-49, 1988.

[89] S. Osher and R. Fedkiw, "Level set methods and dynamic implicit surfaces," *Applied Mathematical Sciences* , 2003 Springer-Verlag New York , Inc.

[90] C. Ramananjaona, M. Lambert, and D. Lesselier, "Shape inversion from TM and TE real data by controlled evolution of level sets," *Inverse Problems*, vol. 17, pp. 1585-1595, 2001.

[91] C. M. Rappaport , M. Kilmer, E. Miller, "Accuracy considerations in using the PML ABC with FDFD Helmholtz equation computation," *Journal of Numerical Modelling*, 1999.

[92] F. Santosa, "A level set approach for inverse problems involving obstacles," *ESAIM Control, Optimization and Calculus of Variations*, vol. 1, pp. 17-33, 1996.

[93] J. A. Sethian." Level set methods and fast marching methods ," *Cambridge University Press*, 2nd edition, 1999.

[94] M. Schweiger, S. R. Arridge, O. Dorn, A. Zacharopoulos, and V. Kolehmainen, "Reconstructing absorption and diffusion shape profiles in optical tomography using a level set technique," *Optics Letters*, vol. 31, pp. 471-473, 2006.

[95] Y. Shi and W. C. Karl, "A multiphase level set method for tomographic reconstruction of dynamic objects," *2003 IEEE Workshop on Statistical Signal Processing*, pp. 182-185.

[96] J. M. Sill and E. C. Fear, , "Tissue sensitive adaptive radar for braest cancer detection: study of immersion liquids," *Electronics Letters*, vol. 41, 2005.

[97] A. E. Souvorov, A. E. Bulyshev, S. Y. Semenov, R. H. Sveson, and G. P. Tatsis, "Two-dimensional computer analysis of a microwave flat antenna array for breast cancer tomography," *IEEE Trans. Microwave Theory Tech.*, vol. 48, pp. 1413-1415, 2000.

[98] "IEEE Standard for safety levels with respect to human exposure to radio frequency electromagnetic fields,3 kHz to 300 GHz," *IEEE* Std., C95.1,1999.

[99] A. J. Surowiec, S. S. Stuchley, J. R. Barr and S. Swarup, "Dielectric properties of breast carcinoma and the surrounding tissues", *IEEE Trans. Biomed. Eng.*, vol. 35, pp. 257-263, 1988.

[100] X. C. Tai, and T. F. Chan, "A survey on multiple level set methods with applications for identifying piecewise constant functions," *International Journal of Numerical Analysis and Modeling*, vol. 1, pp. 25–47, 2004.

[101] A. N. Tikhonov," Solution of incorrectly formulated problems and the regularization method", *Soviet Mathematics - Doklady*, vol.4, pp. 1035-1038, 1963.

[102] L. A. Vese and T. F. Chan, "A Multiphase Level Set Framework for Image Segmentation Using the Mumford and Shah Model," *Int. J. Comp. Vision*, vol. 50, no. 3, pp. 271-293, 2002.

[103] R. Villegas, O. Dorn, M. Moscoso, M. Kindelan, F. Mustieles, "Simultaneous characterization of geological shapes and permeability distributions in reservoirs using the level set method, Society of Petroleum Engineers SPE paper 100291, SPE Europec/EAGE Annual Conference and Exhibition, Vienna, Austria, June 12-15, 2006 (Proc. paper C015, pp. 1-12).

[104] D. W. Winters, E. J. Bond, B. D. Van Veen, S. C. Hagness,"Estimation of the Frequency-Dependent Average Dielectric Properties of Breast Tissue Using a Time-Domain Inverse Scatteruing Techique," *IEEE Transctions on Antennas and Propagation*, vol.54, n 11, pp. 3517-3528, 2006.

[105] Weng Cho Chew,“ Waves and fields inhomogeneous media,” *IEEE press*, 1995.

[106] E. Zastrow, S. K. Davis, S. Hagness,“ Safety assessment of breast cancer detection via ultrawideband microwave radar operating in pulsed-radiation mode,” *Microwave and Optical Technology Letters*, vol.40, no.1, pp. 675-677, 2006.

[107] H. Zhao, T. Chan, B. Merriman and S.Osher“ A variational level set to multiphase motion,” *J. Comput. Phys.*,v.127, pp. 179-195,1996.